Dissertation

submitted to the

Combined Faculty of Mathematics, Engineering and Natural Sciences

of Heidelberg University, Germany

for the degree of

Doctor of Natural Sciences

Put forward by

Philipp Schulz

born in Hamburg, Germany

Oral examination: October 31th, 2023

A relativistic diffusion model for hadron production in asymmetric heavy-ion collisions

Referees:

Professor Dr. Georg Wolschin

Professor Dr. Klaus Reygers

Ein relativisches Diffusionsmodell für die Erzeugung geladener Hadronen in asymmetrischen Kollisionen

Die Produktion geladener Hadronen wird in asymmetrischen Schwerionenkollisionen bei relativistischen Energien untersucht, um unser Verständnis des nichtperturbativen Bereiches der Quantenchromodynamik zu vertiefen. Dazu erweitern wir das relativistische Drei-Quellen Diffusionsmodell, ein nichtgleichgewichts-statistisches Modell durch Ersetzen der zugrundeliegenden phänomenologischen Verteilungen mit mikroskopische Verteilungen, die auf dem Parton-Modell basieren. Die Quelle im mittleren Rapiditätsbereich wird durch Gluon-Gluon-Wechselwirkungen unter Verwendung der k_T-Faktorisierung im Rahmen der Theorie der Gluonsättigung berechnet, während die beiden Fragmentationsquellen durch Quark-Gluon-Wechselwirkungen mit Hybrid-Faktorisierung und den Parton-Verteilungsfunktionen bestimmt werden. Die Idee der Fragmentationsquellen basiert auf Baryon-Stopping, erfordert jedoch eine Erweiterung durch einen Diffusionsprozess im Rapiditätsraum, um die Produktion geladener Hadronen erklären zu können. Die abschließende Hadronisierungsphase wird durch die Parton-Hadron-Dualität modelliert. Wir berechnen aus Lösungen einer Fokker-Planck Gleichung numerisch die Pseudorapiditätsverteilungen für Deuteron-Gold (d-Au) bei $\sqrt{s_{NN}} = 200$ GeV und Proton-Blei (p-Pb) bei $\sqrt{s_{NN}} = 5.02$ und 8.16 TeV und vergleichen sie mit experimentellen Daten von RHIC und LHC. Um nicht-analytische Integrale zu behandeln und die für die Berechnungen erforderlichen numerischen Verfahren zu nutzen, wird ein neues und selbst entwickeltes C++-Programm verwendet. Die zentralitätsabhängigen Verteilungen der produzierten geladenen Hadronen aus den Modellberechnungen zeigen eine gute Übereinstimmung mit den experimentellen Daten. Die Modellberechnungen betonen die Relevanz der Fragmentationsquellen für die Zentralitätsabhängigkeit geladener Hadronen, speziell in ultra-peripheren Kollisionen.

A relativistic diffusion model for hadron production in asymmetric heavy-ion collisions

Charged-hadron production in asymmetric heavy-ion collisions at relativistic energies is investigated to enhance our understanding of the non-perturbative regime of Quantum Chromodynamics. We extend the three source Relativistic Diffusion model, a nonequilibrium-statistical model, by substituting the underlying phenomenological distributions with microscopic distributions based on the parton model. The mid-rapidity source is computed through gluon-gluon interactions using k_T-factorization within the framework of gluon saturation, while the two fragmentation sources are determined by quark-gluon interactions using hybrid-factorization and the parton distribution functions. The concept of the fragmentation sources is grounded in the phenomenon of baryon stopping but requires an extension through a diffusion process in rapidity space allowing to explain charged-hadron production. The final hadronisation stage is modeled based on parton-hadron duality. We calculate the pseudorapidity distributions for deuteron-gold (d-Au) at $\sqrt{s_{NN}} = 200$ GeV and proton-lead (p-Pb) at $\sqrt{s_{NN}} = 5.02$ and 8.16 TeV numerically from solutions of the corresponding Fokker-Planck equation and compare them with experimental data from RHIC and LHC. In order to address non-analytical integrals and to utilize the numerical procedures required for the computations, a novel and self-developed C++ program is utilized. The centrality-dependent distributions of produced charged hadrons obtained from the model calculations exhibit good agreement with the experimental data. The model calculations also highlight the significance of the fragmentation sources in comprehending the centrality dependence of produced hadrons, with particular emphasis on their pronounced influence in ultra-peripheral collisions.

Contents

List of Figures

1. Introduction

In this thesis, we develop a model to calculate the longitudinal distributions of produced charged hadrons in heavy-ion collisions. The primary objective of this work is to investigate asymmetric deuteron-gold (d-Au) and proton-lead (p-Pb) collisions at ultra-relativistic energies. We calculate microscopic distributions of produced charged hadrons in the framework of gluon saturation and provide the distributions as initial conditions of an established one-dimensional diffusion model, known as the Relativistic Diffusion model.

The significance of this work stems from its exploration of particle production in asymmetric collisions at ultra-relativistic energies, offering a valuable approach to gain a deeper understanding of the consequences of gluon saturation in high-energy collisions.

1.1. Motivation

The Standard Model of particle physics serves as a comprehensive framework that encompasses the entire spectrum of particles and accurately predicts a wide range of physical phenomena. The model is rooted in the theory of quantum fields and relies on the principle of local gauge invariance. It incorporates three fundamental forces: the strong force, the weak force, and the electromagnetic force. At higher energies the strong force becomes the dominant interaction. In this thesis our focus is exclusively on the interactions governed by the strong force.

Quantum Chromodynamics (QCD), the theory that describes the strong force, considers color-charged particles known as quarks and gluons. QCD also describes the transition to color-neutral hadrons, which are classified into two families: mesons and baryons. Mesons are composed of a quark-antiquark pair, while baryons consist of three quarks, each carrying a different color charge. Through their combination, the quarks form color-neutral states.

The precise mechanism of confinement and chiral symmetry breaking which elucidates how quarks and gluons combine to form hadrons, remains a complex and unresolved issue. However, specific processes do not require the precise mechanism for accurate predictions, due to a fundamental property of QCD.

The factorization theorem permits the separation of scales within a process. In the context of collisions, the entire process can be decomposed into distinct hard- and soft-scattering components, allowing for the description of hadron production without the necessity for a precise understanding of the underlying mechanisms governing hadron formation.

The concept of factorization plays a dominant role also in deep inelastic scattering, a process where the incident particle is disrupted. By analysing such scattering at different energy scales, various internal structures of the colliding constituents have been unveiled. A similar progressive exploration led to the discovery of atoms and subsequently to the identification of nuclei. It also became evident that nuclei are composed of protons and neutrons, known as nucleons. Going even further, the current understanding in the field reveals that nucleons themselves are comprised of quarks and gluons.

A comparable methodology is employed in the study of particle production in heavy-ion collisions at relativistic energies, providing an alternative perspective on the underlying processes. In this context, the projectiles involved are hadronic particles such as protons, deuterons, or lead nuclei. Asymmetric heavy-ion collisions introduce distinct energy scales and reveal diverse aspects of the underlying physical phenomena. Nevertheless, these processes cannot be adequately analysed through standard perturbative methods that rely on the assumption of a small coupling constant and an initial point-like particle.

QCD-based calculations within the framework of quantum field theories necessitate the appropriate treatment of regularization and renormalization techniques. Regularization is employed to handle singularities arising from unknown processes at higher energies, while renormalization is utilized to address singularities resulting from self-interactions. To take these effects into consideration, the coupling constant, denoted as α_s, becomes energy-dependent. This is called running coupling.

The behaviour of the running coupling of QCD distinguishes it from other couplings of the Standard Model. Figure 1.1 illustrates the running coupling of QCD, demonstrating that at higher energies, the theory exhibits asymptotic freedom. Conversely, at lower energies, QCD enters a non-perturbative regime, characterized by the phenomenon of confinement.

The transition from perturbative to non-perturbative QCD is characterized by the energy scale $\Lambda_{\mathrm{QCD}} \approx 200\,\mathrm{MeV}$. At energies below Λ_{QCD}, the standard perturbative loop expansion ceases to be a reliable method of calculation.

Various methods have been developed to describe the non-perturbative regime of QCD. One such method is lattice QCD, which allows for the study of static properties within the theory. However, lattice QCD faces limitations when applied to dynamic collisions, and it becomes particularly challenging to incorporate fermions due to the sign problem.

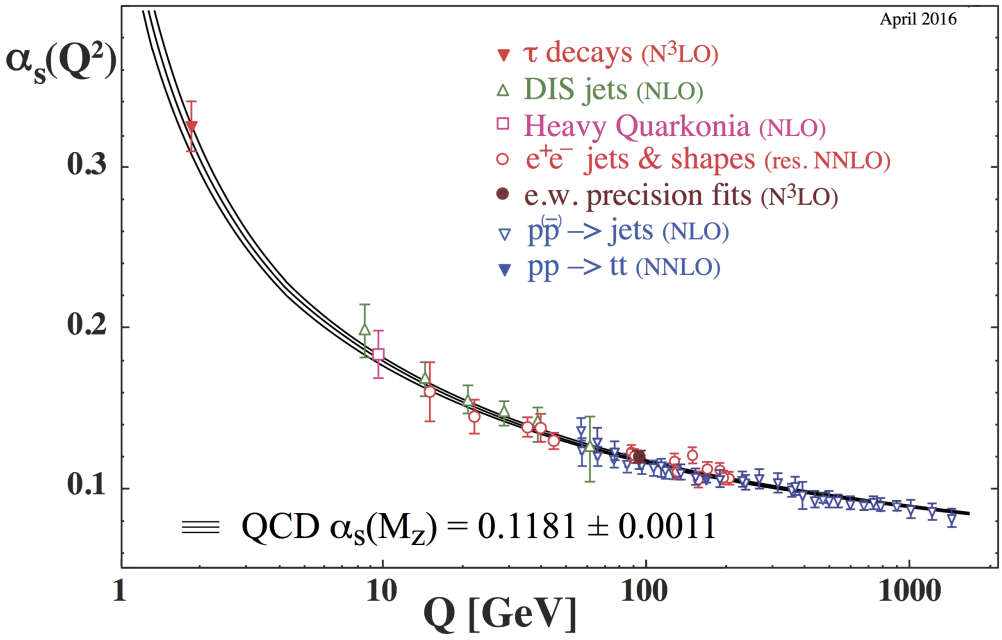

Figure 1.1.: Energy dependence of the Quantum Chromodynamics (QCD) coupling $\alpha_s(Q^2)$ based on renormalization at higher loop-order. The initial energy scale is set to the mass of the Z-boson, M_Z. At smaller energies, the strong coupling constant α_s increases, leading to a non-perturbative regime. Figure taken from Bethke [1].

In the present understanding, the production of hadrons in heavy-ion collisions at relativistic energies is primarily governed by the non-perturbative regime of QCD. As a consequence, direct calculations of hadron production from first principles are unfeasible at the current juncture. But, investigations have been conducted to develop effective theories and phenomenological models that allow to describe multiple aspects of hadron production. These include the framework of gluon saturation and the theory of the Color Glass Condensate.

The abundance of initial and produced particles in heavy-ion collisions allows to conceptualize these collisions as many-body systems. As a result, both relativistic hydrodynamics and statistical diffusion models can be employed to effectively describe various aspects of the process of hadron production.

Acquiring insights into the thermalisation process of the system's macroscopic degrees of freedom holds substantial significance, as the system is anticipated to not completely attain its equilibrium state due to the hadronisation process. Therefore, hadron production can be explained by effects of hot or cold nuclear matter [2].

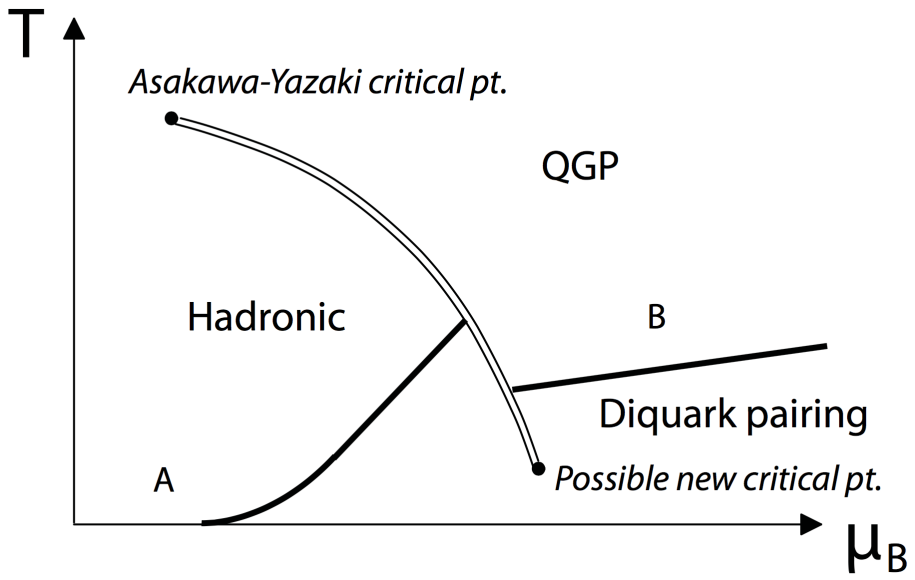

Figure 1.2.: Schematic phase diagram of Quantum Chromodynamics. The temperature T and the baryon potential μ_B define the physical state of the system. The baryon potential μ_B indicates the number of baryons relative to the number of hadrons. Relativistic heavy-ion collisions at LHC energies are expected to be located in the region of high temperatures and small baryon potential, between the hadronic phase and the Quark-Gluon Plasma. Figure taken from Baym [3].

Figure 1.2 depicts a schematic representation of the QCD phase diagram. Heavy-ion collisions involving a significant number of participating nuclei, such as symmetric Pb-Pb collisions with approximately 300 participants, are anticipated to exhibit a larger presence of hot nuclear matter.

In recent experiments at the Large Hadron Collider (LHC) certain regions attain temperatures high enough to produce a novel state of matter called the Quark-Gluon Plasma (QGP). Following the deconfinement phase, the plasma cools down, leading to confinement at the critical temperature.

In contrast, asymmetric heavy-ion collisions such as p-Pb collisions, are anticipated to exhibit more pronounced effects of cold nuclear matter, as discussed in [4]. To account for these effects, an accurate description of the initial state is essential. The parton model, an effective model for the structure of the proton, provides universal distributions known as parton distribution functions, which are employed to describe the initial state.

The determination of these parton distribution functions is achievable through alternative experiments, such as conducted at the Hadron–Electron Ring Accelerator (HERA), and they are applied by invoking the factorization theorem of QCD. Furthermore, the shift from proton to heavy-ion initial states introduces supplementary effects, including shadowing phenomena.

In the context of our research, a significant aspect within the framework of the parton model pertains to the behaviour of the gluon distribution at small momenta relative to the total momenta. Empirical observations reveal a continuous increase in gluon content at lower fractional momenta, giving rise to concerns about the unitarity of the distribution. This issue arises due to the absence of experimental data for very small fractional momenta.

In response to these challenges, a number of researchers have formulated an effective theoretical approach termed the Color Glass Condensate (CGC). This framework offers a more comprehensive means of gluon distributions. This theory predicts the saturation of gluons through gluon recombination, a crucial characteristic of non-abelian gauge theories.

In the CGC regime, the dynamic energy scale transitions from Λ_{QCD} to a hard probe scale, called the saturation scale Q_s. This scale is instrumental in predicting cold nuclear matter effects in hadron production within heavy-ion collisions, and it aligns with the k_T-factorization scheme.

Exploring baryon stopping is a promising approach to deepen our understanding of cold nuclear matter effects, particularly as it is expected to manifest shortly after the collision. Alongside our investigation of hadron production in asymmetric heavy-ion collisions at relativistic energies, the study of baryon stopping holds significant importance. Experimental investigations on this matter have already taken place at the BNL Relativistic Heavy-Ion Collider (RHIC) [5].

After outlined various aspects concerning hadron production in heavy-ion collisions at relativistic energies, we will now provide an overview of previous studies that have laid the groundwork for our present research.

1.2. State of the art

A recently published paper from the ALICE collaboration provides a comprehensive overview of the field of heavy-ion collisions, with a specific focus on the effects of hot matter [6].

Earlier investigations concerning p-Pb collisions at energies of $\sqrt{s_{NN}} = 5.02\,\mathrm{TeV}$ are documented in [7, 8]. In these studies, calculations of pseudorapidity distributions for produced charged hadrons were conducted using comparable microscopic frameworks.

This includes calculations with the AMPT event generator [9] as well as with the impact-parameter dependent CGC (b-CGC) model [10]. Both show good agreement with the centrality-dependent experimental data. However, at ultra-peripheral collisions some significant deviations can be observed, resulting in underestimating the hadron production in that region.

Furthermore, in [11] predictions for cold nuclear matter effects for p-Pb collisions at $\sqrt{s_{NN}} = 8.16\,\text{TeV}$ have been presented and are considered as state of the art.

One of the calculations incorporated in this study and originating from [12] entails centrality-dependent calculations for the pseudorapidity distributions of produced charged hadrons. However, their focus is exclusively on gluon-gluon interactions. Additionally, the transformation to pseudorapidity was performed using an effective mass, rather than considering the specific masses of the individual hadron species and the exact transformation.

The origin of the Relativistic Diffusion model (RDM), a three source phenomenological diffusion model, can be traced back to [13]. In a further paper [14], this model was used to investigate the experimental data from Phobos for d-Au and Au-Au collisions. In this context, the model utilizes delta distributions as initial conditions, which were replaced in further studies by Gaussian distributions. Subsequent refinements of the RDM for Pb-Pb collisions were undertaken in studies conducted in [15–17], whereas these advancements were also compared to p-Pb collisions in [18].

1.3. Outline

This thesis examines charged-hadron production in heavy-ion collisions at ultra-relativistic energies, with a primary focus on asymmetric collisions. In chapter 2, we provide an introduction to the kinematics of heavy-ion collisions at relativistic energies.

In section 2.1 we initiate our discussion by formulating relativistic momenta, accounting for the distinctive momentum direction inherent in heavy-ion collisions. To ensure a well-behaved Lorentz quantity, we introduce the concept of rapidity which is determined individually for each particle species. By utilizing rapidity, we can establish the beam rapidity and the nucleon-nucleon center of mass frame of reference. This specific reference frame holds notable significance as it establishes the context in which our theoretical computations have been conducted.

To be able to compare our theoretically calculated distributions with experimental data, it is essential to establish a quantity that measures unidentified particles. For this, we introduce section 2.2 the concept of pseudorapidity and examine the transition between pseudorapidity and rapidity, along with its observable effects.

In the final section, 2.3, of the kinematical introduction we examine the Glauber Model which provides a geometric extrapolation of collision participants. Furthermore, we discuss the definition of centrality classes, a concept that will be extensively utilized in the subsequent results section.

In chapter 3, we provide an overview of the fundamentals of the parton model, along with its extensions related to gluon saturation. We also outline the DGLAP equation which describes the parton distribution functions within the initial proton. We discuss the framework of gluon saturation, which describes the gluon distribution at small-x and non-zero transverse momenta, and introduce the concept of rapidity evolution. For the actual calculations, we review two models of the gluon distribution: the GBW and the KLN model.

After the introduction of the parton distribution functions, we outline the concept of QCD factorization in chapter 4. In order to characterize hadron production, we will introduce the k_T-factorization, where hadrons are produced from interactions between small-x gluons, and the hybrid-factorization, which yields hadrons from quark-gluon interactions.

In contrast to the microscopic description based on the parton model, chapter 5 presents a macroscopic model known as the Relativistic Diffusion model. This model is phenomenological and operates in a non-equilibrium statistical framework in one dimension. It offers a statistical description of the process from the stopping-inspired phase to subsequent time intervals associated with hadron production within the context of heavy-ion collisions.

Chapter 6 focuses on the presentation of the extended Relativistic Diffusion model and its details. It also elaborates on the numerical approach utilized for the calculations. Subsequently, we present two calculations of the pseudorapidity distribution for central collisions at LHC energy. These calculations are conducted in order to compare and contrast the two models, GWB and KLN, of the unintegrated gluon distribution. Additionally, the pseudorapidity distributions resulting from the diffusion process of the fragmentation sources for intermediate time intervals and the transverse momentum distribution of the gluon-gluon source for three pseudorapidites are displayed.

In the next section, we present centrality-dependent calculations for Pb-Pb collisions at LHC energy of $\sqrt{s_{NN}} = 5.02\,\text{TeV}$ to demonstrate the symmetric limit of our predominantly asymmetric model description.

Subsequently, we discuss our computations for minimum bias collisions at three energies: $\sqrt{s_{NN}} = 200\,\text{GeV}, 5.02\,\text{TeV}$, and $8.16\,\text{TeV}$. This allows us to investigate the impact of increasing collision energies on our model.

In chapter 7, various centrality-dependent calculations for the pseudorapidity distribution of hadron production are presented. We start to discuss the results for $\sqrt{s_{NN}} = 200\,\text{GeV}$ d-Au collisions. Despite the energy not being as high as energies

for collisions at the LHC, these collisions are still of great interest for investigation. The experimental data for these collisions cover a wide range of pseudorapidity values, including regions close to the beam rapidity.

Continuing to the following section, we present our calculations of centrality-dependent pseudorapidity distributions at $\sqrt{s_{NN}} = 5.02\,\text{TeV}$ alongside experimental data obtained from ATLAS and ALICE. The calculations exhibit slight variations due to different centrality classes.

Of particular significance are the computations of centrality-dependent pseudorapidity distributions related to the ALICE data, depicted in figure 7.5. The recently available experimental data covers a pseudorapidity range of $|\eta| < 5$, offering novel insights that are especially pertinent to the understanding of ultra-peripheral collisions.

In the last section we provide an analysis of our model calculations for p-Pb collisions at $\sqrt{s_{NN}} = 8.16\,\text{TeV}$ and present predictions for the pseudorapidity distributions up to approximately $|\eta| < 4$. Additionally, this section explores the centrality-dependent behaviour of a key model parameter, the initial saturation scale Q_0.

Finally, in chapter 8, we conclude the discussion and provide an outlook for further developments in describing cold nuclear matter effects on hadron production in relativistic heavy-ion collisions.

2. Kinematics of high-energy collisions

In this chapter, we present the essential concepts and variables that are relevant to relativistic heavy-ion collisions, with a strong emphasis on asymmetric collisions. After important studies, like [19], numerous concepts have been developed to address challenges in describing asymmetric collisions, where the laboratory frame of reference differs from the frame in which theoretical calculations can be performed. For symmetric collisions, these frames coincide.

The kinematics of high-energy collisions have been extensively studied and summarized in various publications, and in this study, we follow the approach presented in [20] and [21].

First, we describe symmetric collisions and establish the nucleon-nucleon center of mass frame of reference. We define the concept of rapidity and the beam rapidity, which are essential in characterizing the initial particle motion in such collisions. Next, we derive the important parameter Δy, which allows us later to transform the system in which our calculations are performed into the experimental laboratory system.

Before the collisions occur, there are typically two particle beams, each of which can be described by their respective 4-momenta, denoted by $p_\mu = (p_0, p_x, p_y, p_z)$. With the particle mass m, the relativistic energy relation of each particle beam is given by the equation

$$(mc^2)^2 = p^\mu p_\mu, \tag{2.1}$$

which we can rearrange to their energy

$$E^2 = (mc^2)^2 + (\mathbf{p}c)^2, \tag{2.2}$$

where $\mathbf{p}$ describes the three-momentum of the particle and $p_0 = E/c$. Due to the nature of the collision, we can always define a distinguished axis along which the momentum of the particles can be decomposed into its longitudinal component p_z and its transverse component p_T, as follows

$$\mathbf{p}^2 = p_z^2 + \mathbf{p}_T^2. \tag{2.3}$$

Further splitting of the momentum is not needed due to the expected spherical symmetry.

In the context of heavy-ion collisions, defining the initial energy of a particle within the beam can be accomplished by understanding the electromagnetic coupling between the beam particles and the magnetic setup in the laboratory frame of reference. The frame of reference plays an important role in the context of asymmetric collisions. The assumption is that no transverse momentum in the beam exists, and the acceleration of the beam particles is facilitated by the external magnetic field.

The longitudinal component of the momenta, denoted by p_z, is determined by the experimental magnetic setup. With heavy-ions as beam particles, their longitudinal momentum, referred to as p_{beam}, is defined by

$$p_{\text{beam}} = \frac{Z}{A} p_z, \tag{2.4}$$

where Z is the number of protons and A the mass number of the beam particle. In other words, while Z protons couple to the external magnetic field, the presence of the rest mass of the nuclei suppresses this coupling.

Before moving to asymmetric collisions, the definition of the center of mass frame of reference for symmetric collisions is straightforward. In the laboratory frame, the particle four-momenta of the two colliding beams are denoted as p_a and p_b, and their momenta are related by

$$\mathbf{p}_a = -\mathbf{p}_b. \tag{2.5}$$

By employing the above assumption along with the total energy of the collision, we can define the Mandelstam variable s by

$$s := (p_a c + p_b c)^2 = (E_a + E_b)^2 = E_{\text{cms}}^2 \tag{2.6}$$

Considering equal energy for both beams, we get $E_{\text{cms}} = 2E$. Based on these definitions we can define the nucleon-nucleon center of mass frame of reference by

$$\sqrt{s} = A\sqrt{s_{NN}}. \tag{2.7}$$

This follows by the fact that each particle beam consists of A ions, resulting in a total of $2A$ ions. It is important to note that in this frame of reference, the two nuclei approach each other with the same boost factor [21].

In the subsequent section, we proceed to a more precise depiction of the transformations across various frames of reference, an important consideration in the analysis of asymmetric collisions.

2.1. The rapidity and identified particles

In this section, we aim to define a quantity that allows the transformation of the initial laboratory frame of reference into a co-moving system where each nucleon has the same velocity.

In symmetric collisions, both frames of reference coincide, meaning they are equivalent and lead to the same description of the physical processes. However, in asymmetric collisions, the two frames of reference differ significantly, and the distinction between the laboratory and the nucleon-nucleon system becomes important.

To facilitate the transformation of relativistic momenta, it is common to introduce the concept of the rapidity y, as defined by

$$y = \frac{1}{2} \ln \left(\frac{p_0 + p_z}{p_0 - p_z} \right), \tag{2.8}$$

where p_z is the particle momentum in the direction of the beam axis and p_0 its energy [20]. Mathematically, one could go deeper into the concept of rapidity, providing additional details and formalisms, like the definition of light-cone variables. However, for our purposes, the given definition of rapidity is sufficient.

Rapidity is a dimensionless quantity that experiences a transformation under longitudinal Lorentz boosts by an additive constant. To illustrate this, we will establish the center of mass rapidity, denoted as y_{cms}, which can be defined from an arbitrary frame of reference, such as the laboratory frame of reference, following the approach presented in [21].

In an arbitrary frame of reference, the center of mass energy and momentum can be expressed as $E = \gamma_{\text{cms}}\sqrt{s}$ and $p = \beta_{\text{cms}}\gamma_{\text{cms}}\sqrt{s}$, respectively, where γ represents the Lorentz factor and is defined as $\gamma = 1/\sqrt{1-\beta^2}$, with $\beta = v/c$ being the ratio of the velocity v to the speed of light c.

Using the definition of the rapidity, we can derive the center of mass rapidity, denoted as y_{cms}, as follows

$$y_{\text{cms}} = \frac{1}{2} \ln \left(\frac{\gamma_{\text{cms}}\sqrt{s} + \beta_{\text{cms}}\gamma_{\text{cms}}\sqrt{s}}{\gamma_{\text{cms}}\sqrt{s} - \beta_{\text{cms}}\gamma_{\text{cms}}\sqrt{s}} \right) = \frac{1}{2} \ln \left(\frac{1 + \beta_{\text{cms}}}{1 - \beta_{\text{cms}}} \right). \tag{2.9}$$

On the other hand, a general longitudinal Lorentz boost with β is given by

$$\begin{pmatrix} E^* \\ p_\parallel^* \end{pmatrix} = \begin{pmatrix} \gamma & -\gamma\beta \\ -\gamma\beta & \gamma \end{pmatrix} \times \begin{pmatrix} E \\ p_\parallel \end{pmatrix}, \tag{2.10}$$

where the transverse momentum remains the same, $p_\perp^* = p_\perp$. In rapidity space, the inverse Lorentz boost is given by

$$y = \frac{1}{2} \ln \left(\frac{\gamma(E^* + \beta p_\parallel^*) + \gamma(\beta E^* + p_\parallel^*)}{\gamma(E^* + \beta p_\parallel^*) - \gamma(\beta E^* + p_\parallel^*)} \right). \tag{2.11}$$

After rearranging and splitting the logarithm, the expression becomes

$$y = \frac{1}{2} \ln \left(\frac{E^* + p_{\parallel}^*}{E^* - p_{\parallel}^*} \right) + \frac{1}{2} \ln \left(\frac{1 + \beta_{\text{cms}}}{1 - \beta_{\text{cms}}} \right). \tag{2.12}$$

Using the definition of the rapidity and the expression for the center of mass rapidity, the transformation property of longitudinal Lorentz boosts in rapidity space can be written as follows

$$y = y^* + y_{\text{cms}}. \tag{2.13}$$

After demonstrating that rapidity undergoes longitudinal Lorentz boosts with an additive constant only, it is important to highlight that the concept of rapidity can also be extended to the transverse plane.

In the context of heavy-ion collisions, we can define the beam rapidity y_{beam} in the laboratory frame of reference by using equation (2.4), which leads to

$$y_{\text{beam}} = \frac{1}{2} \ln \left(\frac{2 Z p_z}{\sqrt{(A\ mc)^2 + (Z p_z)^2} - Z p_z} + 1 \right), \tag{2.14}$$

where m denotes the proton mass. We employ the approximation that neutrons possess the same mass as protons. Expanding with $\sqrt{(A\ mc)^2 + (Z p_z)^2} + Z p_z$, we can rewrite the previous expression as follows

$$y_{\text{beam}} = \frac{1}{2} \ln \left(\frac{2 Z p_z \left(\sqrt{(A\ mc)^2 + (Z p_z)^2} + Z p_z \right)}{A\ mc} + 1 \right). \tag{2.15}$$

As shown, each longitudinal Lorentz boost can be expressed by an additive constant. This constant between the beam rapidities for each individual particle beam in the laboratory frame of reference and the center of mass system can be expressed by their difference in rapidity space Δy.

For general two particle beams with different ion configurations (Z_1, A_1) and (Z_2, A_2), but with the same initial longitudinal momentum, p_z, given by the experimental setup, Δy can be calculated with $p = \delta\ mc$ as follows

$$\begin{aligned} \Delta y \equiv y_{\text{beam},2} - y_{\text{beam},1} = \\ \frac{1}{4} \Bigg(& \ln \left(2 Z_1 / A_1^2\ \delta \left(\sqrt{A_1^2 + Z_1^2 \delta^2} + Z_1 \delta \right) + 1 \right) \\ & - \ln \left(2 Z_2 / A_2^2\ \delta \left(\sqrt{A_2^2 + Z_2^2 \delta^2} + Z_2 \delta \right) + 1 \right) \Bigg). \end{aligned} \tag{2.16}$$

For relativistic collisions, we can take the limit of δ approaching infinity, which provides a good approximation in that case. By using the continuity property of the logarithmic function, we can move the limit inside the logarithm. Consequently, we obtain the same expression for Δy as mentioned in [21]

$$\Delta y \approx \frac{1}{2} \log \left(\frac{Z_1 A_2}{Z_2 A_1} \right). \tag{2.17}$$

It is interesting to note that Δy is independent of the initial momenta and solely depends on the ion configuration. As an example, for p-Pb collisions, we find for momenta greater than $p = 12 m_p$, where m_p denotes the proton mass, an relative error in comparison to the exact solution of approximately 1%, where $\Delta y = 0.4654$.

With the definitions provided above and $y_i := y_{\text{beam},i}$, we can establish a symmetric frame of reference called the nucleon-nucleon center of mass frame of reference. In this frame, the beam rapidity $y_{\text{beam},NN}$ of the two particle beams has the same magnitude but opposite signs, defined by

$$y_{\text{beam},NN} = \frac{y_1 + y_2}{2}. \tag{2.18}$$

For completeness, as derived in [21], the beam rapidity for the center of mass frame of reference $y_{\text{beam,cms}}$ can also be defined by

$$y_{\text{beam,cms}} = \frac{y_1 + y_2}{2} + \frac{1}{2} \ln \left(\frac{m_1 e^{y_1} + m_2 e^{y_2}}{m_1 e^{y_2} + m_2 e^{y_1}} \right). \tag{2.19}$$

As we already have defined the collision energy in the nucleon-nucleon center of mass frame of reference for symmetric collisions in equation (2.7), we can now extend this definition to include asymmetric collisions based on the beam rapidity. The collision energy is given by

$$\sqrt{s_{NN}} = mc^2 \exp(y_{\text{beam},NN}). \tag{2.20}$$

After exploring the description of heavy-ion collisions and the idea of rapidity, it's important to mention that using rapidity involves knowing the masses of the underlying particles. However, in experimental settings, it is often challenging to identify the particle species directly. As a consequence, it becomes necessary to expand our description of heavy-ion collisions to include unidentified particles.

2.2. The pseudorapidity and unidentified particles

The concept of rapidity considers both the mass of the particle and its momentum. However, in cases where particle identification is either not feasible or not desired, an alternative quantity called pseudorapidity η can be utilized. The primary reference for this section is [20].

Beginning with the definition of rapidity from (2.8) with the relativistic limit of $|\mathbf{p}| \gg m$, we arrive at the definition of pseudorapidity as follows

$$\eta = \frac{1}{2} \ln \left(\frac{|\mathbf{p}| + p_z}{|\mathbf{p}| - p_z} \right) \tag{2.21}$$

Having established the definition of pseudorapidity, we can now treat both rapidity and pseudorapidity as independent variables, without assuming the relativistic limit. The derivation of the transformation between rapidity and pseudorapidity is of particular interest as it allows for a direct comparison of later theoretical calculations with experimental data.

Starting with the expression for the rapidity given in equation (2.8), we can derive the following equivalent forms

$$e^{y} = \sqrt{\frac{p_0 + p_z}{p_0 - p_z}}, \qquad e^{-y} = \sqrt{\frac{p_0 - p_z}{p_0 + p_z}}. \tag{2.22}$$

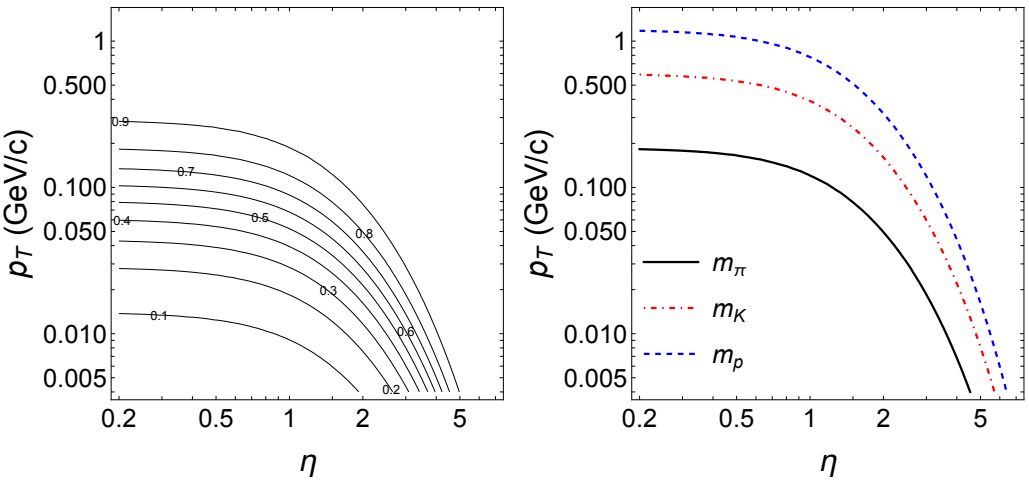

Figure 2.1.: The left displays a contour plot of the Jacobian $J = \mathrm{d}y/\mathrm{d}\eta(\eta, p_T)$ with a fixed mass which is set to the pion mass. The lines on the plot indicate the values of J with increments of $\Delta J = 0.1$. The right plot illustrates a fixed value of the Jacobian $J = 0.8$ for three different hadron masses: pions, kaons and protons (from bottom to top).

To proceed with defining the transformation, we introduce the transverse mass, denoted as m_T, and define it by

$$m_T^2 = (mc)^2 + \mathbf{p}_T^2. \tag{2.23}$$

It is noteworthy to mention that the transverse mass is a quantity with the unit of momentum. Furthermore, expressions for p_0 and p_z can be obtained from equation (2.22), given by

$$p_0 = m_T \cosh y, \qquad p_z = m_T \sinh y. \tag{2.24}$$

Having established these definitions, we proceed to derive the transformations between rapidity and pseudorapidity. Note that we omit the vector notation for p_T in the following. The first transformation expression, denoted as $\eta(y, p_T)$, is given by

$$\eta(y, p_T) = \frac{1}{2} \ln \left(\frac{\sqrt{m_T^2 \cosh^2(y) - m^2} + m_T \sinh(y)}{\sqrt{m_T^2 \cosh^2(y) - m^2} - m_T \sinh(y)} \right). \tag{2.25}$$

The second expression shows the opposite transformation, denoted as $y(\eta, p_T)$, and is given by

$$y(\eta, p_T) = \frac{1}{2} \ln \left(\frac{\sqrt{p_T^2 \cosh^2(\eta) + m^2} + p_T \sinh(\eta)}{\sqrt{p_T^2 \cosh^2(\eta) + m^2} - p_T \sinh(\eta)} \right). \tag{2.26}$$

It is significant for the later comparison of our calculations with experimental data. Therefore, we place emphasis on obtaining more details about the transformation effects. Figure 2.1 illustrates the suppression of the transformation in different regions of momentum space.

Due to the nature of the experimental data, observables in the context of hadron production in heavy-ion collisions at ultra-relativistic energies are expressed in pseudorapidity. However, our theoretical calculations are performed on the level of mass-dependent rapidity and transverse momenta of the produced hadrons.

Consequently, we must perform a transformation of the observable N, representing the produced charged hadrons, from $N(y, p_T)$ to $N(\eta, p_T)$. The transformation takes the form of

$$\frac{\mathrm{d}^2 N\,(\eta, p_T)}{\mathrm{d}\eta\ \mathrm{d}p_T} = \frac{\mathrm{d}y(\eta, p_T)}{\mathrm{d}\eta} \frac{\mathrm{d}^2 N\,(y, p_T)}{\mathrm{d}y\ \mathrm{d}p_T}. \tag{2.27}$$

The factor $\mathrm{d}y(\eta, p_T)/\mathrm{d}\eta$ is denoted as the Jacobian J and can be calculated from the above mentioned transformation expressions. In the literature, multiple forms of the expression are used. One of the most straightforward expressions is

$$\frac{\mathrm{d}y(\eta, p_T)}{\mathrm{d}\eta} = \frac{m_T \cosh(\eta)}{\sqrt{m^2 + m_T^2 \cosh^2(\eta)}}. \tag{2.28}$$

However, an alternative representation of the Jacobian can also be found, as presented in [16], given by

$$J(\eta, p_T) \equiv \cosh(\eta) \left[1 + (m/p_T)^2 + \sinh^2(\eta)\right]^{-1/2}. \tag{2.29}$$

This presents an opportunity to define an effective Jacobian $\widetilde{J}$ by introducing a parameter $p \coloneqq m/\langle p_T \rangle$, which represents the fraction between an effective mass and the mean transverse momentum. With the approximation $\eta \approx y$, we can simplify equation (2.27), allowing us to integrate over p_T without directly involving the transformation to pseudorapidity. The resulting expression takes the form

$$\frac{\mathrm{d}N}{\mathrm{d}\eta} = \widetilde{J}(p) \frac{\mathrm{d}N(y)}{\mathrm{d}y} \tag{2.30}$$

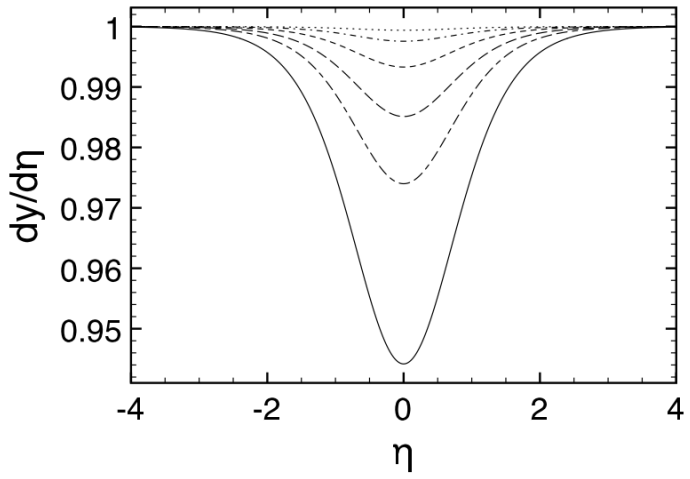

Figure 2.2.: The diagram shows the Jacobian $\widetilde{J} = \mathrm{d}y/\mathrm{d}\eta(p)$ with an effective parameter $p \coloneqq m/\langle p_T \rangle$ for an average mass of $\langle m \rangle = m_\pi$ and various average transverse momenta $\langle p_T \rangle$. The values of $\langle p_T \rangle$ are $0.4, 0.6, 0.8, 1.2, 2, 4\,\mathrm{GeV/c}$ (from bottom to top). The Jacobian shows significant suppression in the central region, corresponding to the mid-rapidity regime. Figure taken from Wolschin [22].

In figure 2.2, we illustrate the influence of the effective Jacobian for various common mean transverse momenta. For the chosen transverse momenta, the impact of the Jacobian is negligible at $\eta > 2$.

While we could make the assumption $\eta \approx y$, we refrain from doing so to thoroughly explore the implications of different hadron masses. Instead, we will maintain the full transformation from rapidity to pseudorapidity to ensure a comprehensive analysis.

From an experimental perspective, there is an alternative way to define pseudorapidity, which characterizes the momentum of unidentified particles. This approach is based on an effective angle θ, defined in the laboratory frame, which measures the angle between the particle trajectory and the beam axis. Based on [23] the effective angle θ can be derived using the definition of pseudorapidity 2.21 and the equation

$$\cos(\theta) = \frac{p_z}{|\mathbf{p}|}. \tag{2.31}$$

Using this relationship, the pseudorapidity η is then defined as

$$\eta = \ln\left(\frac{1-\cos(\theta)}{1+\cos(\theta)}\right) = -\ln\left(\tan(\theta/2)\right). \tag{2.32}$$

After defining the relevant kinematical variables for describing relativistic hadrons, the final section introduces a concept to address the potential geometric implications arising from the collision. This consideration becomes important when dealing with asymmetric collisions.

2.3. The Glauber model and centrality classes

So far, we have been treating the beam particles as point-like entities. However, nuclei are inherently extended objects, and this holds true at all scales relevant to heavy-ion collisions at relativistic energies.

The extended nature of nuclei introduces a central aspect to consider in the analysis and interpretation of experimental results, the collision geometry. The spatial arrangement and overlap of these extended objects profoundly influence the collision dynamics. Therefore, comprehending and accurately accounting for this collision geometry is essential for a thorough understanding of the underlying physics in heavy-ion collisions.

In the center of mass frame, prior to the collision, the incoming two nuclei can be envisaged as two thin disks due to Lorentz contraction along the longitudinal direction. The extent of overlapping of these disks may vary in different collisions.

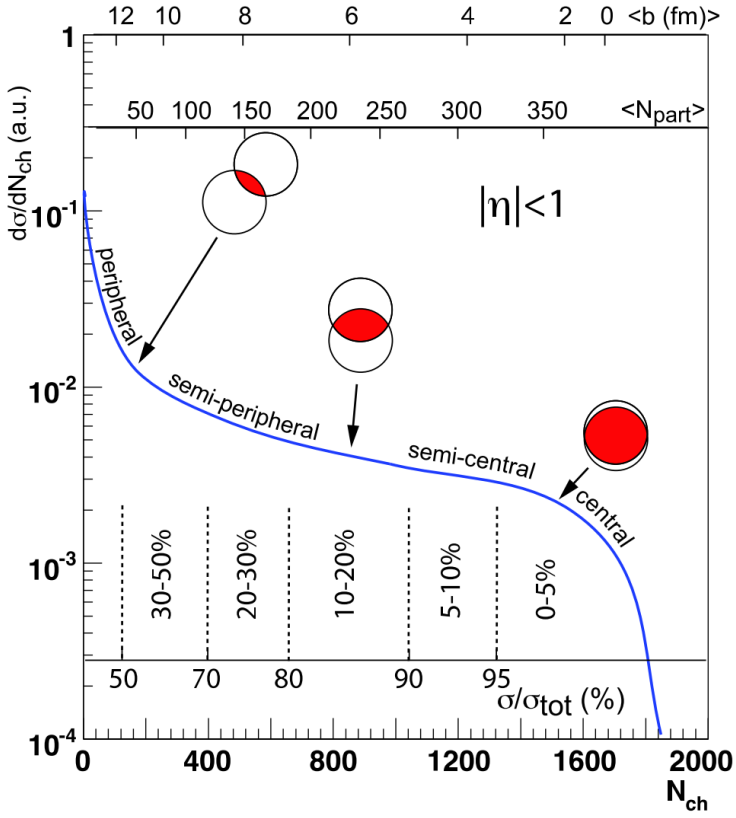

Figure 2.3.: Schematic classification of heavy-ion collisions based on the Glauber Model. Produced charged hadrons N_{ch} are related to Glauber-calculated quantities: the impact parameter b and the number of participants N_{part}. The fraction of the measured cross section to the total cross section $\sigma/\sigma_{\mathrm{tot}}$ defines the centrality classes, where 0-5% indicate central collisions and smaller fractions of the cross section correspond to more peripheral collisions. Figure taken from Miller [24].

Based on the collision's geometry, several quantities can be predicted, where for our study the number of collision participants and the centrality classes are of importance. The conventional approach to compute these geometric quantities is through a probabilistic model known as the Glauber model, introduced in [25], which we elucidate in the subsequent section.

The probabilistic description begins with the consideration of the nucleon density within nucleus A. This density is denoted by $\rho(z, \mathbf{b})$ and depends on both the longitudinal position z and the transverse position $\mathbf{b}$, which also refers to the impact parameter.

In many calculations, the nuclear profile function, or thickness function, emerges as the central quantity of interest. This function is defined as follows

$$T_A(\mathbf{b}) = \int_{-\infty}^{\infty} \mathrm{d}z \; \rho(z, \mathbf{b}). \tag{2.33}$$

With the normalization condition $\int \mathrm{d}\mathbf{b} \; T_A(\mathbf{b}) = 1$, the individual probability of a nucleon-nucleon interaction at a specific impact parameter $\mathbf{b}$ is $T_A(\mathbf{b})\sigma_{NN}^{\mathrm{inel}}$. Now, when considering a proton-nucleus collision, the probability that the proton interacts with n nucleons within the nucleus is given by the expression

$$P(n, \mathbf{b}) = \binom{A}{n} \left[1 - T_A(\mathbf{b})\sigma_{NN}^{\mathrm{inel}}\right]^{A-n} \left[T_A(\mathbf{b})\sigma_{NN}^{\mathrm{inel}}\right]^{n}, \tag{2.34}$$

where the first factor denotes the binomial coefficient, $\sigma_{NN}^{\mathrm{inel}}$ represents the inelastic nucleon-nucleon cross-section, and A is the nucleon number in the nucleus. We proceed to calculate the number of collisions, denoted as N_{coll}^{pA}, for a given impact parameter as follows

$$N_{\mathrm{coll}}^{pA}(\mathbf{b}) \equiv N_{\mathrm{part}}^{A}(\mathbf{b}) = \sum_{n=0}^{A} n \, P(n, \mathbf{b}) = A \; T_A(\mathbf{b})\sigma_{NN}^{\mathrm{inel}}, \tag{2.35}$$

where N_{part}^{A} signifies the number of participants in nucleus A. It coincides with the number of collisions N_{coll} since each nucleon in nucleus A interacts only once. The total number of participants, including the colliding proton, is then given by

$$N_{\mathrm{part}} = 1 + N_{\mathrm{part}}^{A}(\mathbf{b}). \tag{2.36}$$

An additional property that can be determined within this model is the geometric inelastic cross-section of the collision, denoted as $\sigma_{pA}^{\mathrm{inel}}$. It can be calculated as follows

$$\begin{aligned} \sigma_{pA}^{\mathrm{inel}} &= \int \mathrm{d}\mathbf{b} \sum_{n=1}^{A} P(n, \mathbf{b}) = \int \mathrm{d}\mathbf{b} \left[1 - \left(1 - T_A(\mathbf{b})\sigma_{NN}^{\mathrm{inel}}\right)^{A}\right] \\ &= \int \mathrm{d}\mathbf{b} \left[1 - \exp\left(-A \; T_A(\mathbf{b})\sigma_{NN}^{\mathrm{inel}}\right)\right], \end{aligned} \tag{2.37}$$

where the limit of large A has been considered for the last equality.

The Glauber model employs distinct underlying distributions, such as the Fermi distribution or the Wood-Saxon distribution, to characterize the geometry of the Lorentz-contracted nucleus involved in the collision. It predicts then the extent of overlap between the two colliding beams. Commonly, the nucleon density is described by a Fermi distribution formulated as follows

$$\rho(r) = \rho_0 \frac{1 + w(r/R)^2}{1 + \exp\left(\frac{r-R}{a}\right)}, \tag{2.38}$$

where ρ_0 represents the nucleon density at the nucleus center, while R denotes the nuclear radius. The parameters a characterizes the skin depth and w accounts for deviations from a spherical nucleon shape [24]. An illustrative example employed at RHIC is ^{197}Au, which is characterized by the parameter $R = 6.38\,\text{fm}$, $a = 0.535\,\text{fm}$ and $w = 0$. Another example is ^{208}Pb with the parameters $R = 6.62\,\text{fm}$, $a = 0.546\,\text{fm}$ and $w = 0$ [26].

The same conceptual framework can also find application in the context of nucleus-nucleus collisions. In addition, it is important to highlight that the Glauber model offers two distinct implementations for calculating these geometric properties: the optical-limit approximation and the Monte Carlo approach. However, due to our specific focus on asymmetric collisions, we shall abstain from further exploration of these aspects. Comprehensive details on these aspects are expounded in [24].

One particular expression that has been instrumental in our calculations is of significance. Analogous to equation (2.36), this expression pertains to the total number of participants in nucleus-nucleus collisions, which is given by

$$N_{\text{part}}(\mathbf{b}) = N^A_{\text{part}}(\mathbf{b}) + N^B_{\text{part}}(\mathbf{b}), \tag{2.39}$$

where N^A_{part} and N^B_{part} represent the numbers of participants for nuclei A and B. Typically, the characterized geometric properties exhibit a dependence on the impact parameter b. However, in order to facilitate the comparison of these quantities with experimental observations, the Glauber model introduces the concept of centrality classes.

Figure 2.3 provides a schematic illustration of the hierarchical classification of heavy-ion collisions based on their geometric attributes. The average over all possible collision geometries is called minimum bias.

This concludes the introduction to the kinematics of relativistic heavy-ion collisions. The next chapter introduces the parton model and the framework of gluon saturation.

3. Quarks and gluons

In the preceding chapter, we outlined the kinematics of heavy ions at relativistic energies. Moreover, we started to shift from considering point-like nuclei to contemplating geometrically extended entities. In the current chapter, our objective is to deepen our comprehension of the internal structures inherent to nuclei and elucidate their correlation with models inspired by QCD.

We begin by laying out the concept of deep inelastic scattering. This involves introducing partons within the infinite momentum frame and using a technique called QCD factorization to untangle universal patterns, such as the parton distribution functions. As we gradually move away from the initial assumption of the infinite momentum frame, we can consider the inclusion of transverse momenta. This shift leads us into the domain of gluon saturation framework, where we can define the unintegrated gluon distribution.

The conceptional background of processes in QCD can be traced back to [27], where the landscape of semi-hard processes is examined. For the scope of our investigation, our exclusive focus centers on the significance of deep inelastic scattering (DIS), where we follow an introduction from [28].

These processes entail the collision of electrons with more extended entities, such as e+p or e+A collisions. The underlying interactions involve the exchange of photons. These photons can also serve as a simplified framework to conceptualize gluon exchange. An experimental configuration for the measurement of such scatterings is provided by the Hadron–Electron Ring Accelerator (HERA).

Our exploration commences by delving into the phenomenon of electron-nucleus scattering, focusing on a configuration where a photon is exchanged between an electron and a nucleus, denoted as N.

The probing photon employed a wavelength denoted as $\lambda \sim 1/Q$, encapsulating momenta described by Q. The momentum of the photon is related to its 4-momentum by $Q^2 = -q^2$.

For nucleus N, the momentum associated with the nucleus is represented by p_N. The nucleus possesses a mass designated as M_N. The invariant mass, symbolized as W, is defined as

$$W^2 = (p_N + q)^2 = M_N^2 + 2p_N \cdot q + q^2. \tag{3.1}$$

Based on this foundation, two assumptions come into play: In the scenario where $Q^2 \gg M_N^2$, the scattering process is classified as deep. If we consider $W^2 \gg M_N^2$, the scattering event takes on the characteristic of being inelastic.

Let us trace the evolution as we systematically elevate the energy of the electron, thereby causing a reduction in the wavelength λ of the probing photon.

Our investigation commences within the regime $\lambda \gg R_N$, where R_N signifies the nucleus's radius. In this particular scenario, the photon perceives the nucleus as a point-like entity, resulting in elastic electron-nucleus scattering with $W = M_N$. To quantify this, we introduce the parameter

$$x_N \equiv \frac{Q^2}{2p_N \cdot q} = \left(\frac{Q^2}{2M_N\nu}\right)_{\text{lab}} = 1, \tag{3.2}$$

where ν denotes the electron's energy loss. As previously mentioned, when $x_N = 1$, the photon perceives the nucleus as a point-like particle.

However, as the energy increases, the value of x_N diminishes below 1, implying the existence of an internal structure. This phenomenon is illustrated by the peak of $x_N(Q^2)$ shifting to $x_N = 1/A$, where A represents the number of bounded point-like particles within the nucleus, called nucleons. That is conceptualized as deep ($Q^2 \gg M_N^2$) inelastic ($W^2 \gg M_N^2$) electron-nucleus scattering.

As the energy scale increases, a corresponding progression of observed substructures ensues, facilitating the interpretation of the nucleon, particularly the proton, as an extended entity endowed with momentum p. The definition of x is then given by

$$x = \frac{Q^2}{2p \cdot q}. \tag{3.3}$$

Analogous to the identification of nucleons, an observation arises from the energy dependence of the variable x, which manifests a peak at $x = 1/3$, providing an indication of the presence of valence quarks within the proton. The variable x is called the Bjorken scaling variable [29].

As we increase the energy even further, an intriguing phenomenon known as Bjorken scaling violation becomes evident. However, this deviation does not stem from additional substructures within the quarks. Instead, it is a manifestation of QCD effects exerted on quarks and gluons with the effects of the running coupling of the QCD constant α_s.

In the upcoming sections, we undertake a thorough investigation into the quark and gluon composition within the proton, with a particular focus on the context of relativistic heavy-ion collisions. We commence by introducing the Parton model, a theoretical construct employed to describe Parton distribution functions. Subsequently, we investigate the concept of gluon saturation within dense systems. Finally, our discourse concludes by outlining two distinct models that provide an

effective description of the gluon distributions pertinent to our subsequent computational analyses.

3.1. The Parton model

Following our exploration of the fundamental structure within the proton in the previous section, we now embark on a comprehensive examination of the Parton model.

We begin by considering the Lagrangian formulation of Quantum Chromodynamics (QCD) [30], which takes the form of

$$\mathcal{L}_{\mathrm{QCD}} = \bar{q}_f \left(i \not{D} - m \right) q_f - \frac{1}{4} F^a_{\mu\nu} F^{\mu\nu}_a, \tag{3.4}$$

which is invariant under the local $SU(3)$ non-abelian gauge group. This symmetrical group introduces the notion of three distinct color charges. The primary constituents of the particle framework are represented by the substantial quark fields, designated as q_f, and belong to the fundamental representation of the $SU(3)$ gauge group.

The concept of local gauge invariance associated with the Dirac operator $\not{D}$, which assumes the adjoint representation, introduces the gluon fields. These fields act as the carriers of the strong force, governing the interactions between particles.

The strength of these interactions, characterized by the strong coupling constant α_s, defines the dynamics underlying the exchange of particles between quark and gluon fields.

The application of perturbative expansions within this theory gives rise to divergences in observables. To address these divergences and restore meaningful results, a process known as renormalization needs to be applied. This process involves the introduction of a new non-physical energy scale denoted as μ and an alteration in the energy-dependent behaviour of the coupling constant.

The leading-order equation governing the renormalized strong coupling in the minimal subtraction ($\overline{\mathrm{MS}}$) scheme [28] is expressed as

$$\alpha_s(Q^2) = \frac{\alpha_s(\mu^2)}{1 + b_0 \alpha_s(\mu^2) \log(Q^2/\mu^2)}, \tag{3.5}$$

where the constant b_0 is defined as $b_0 = (33 - 2n_f)/12\pi$, and the term n_f indicates the count of quark fields. In the context of the $\overline{\mathrm{MS}}$ scheme, the value of n_f is set to $n_f = 5$. An important value for the strong coupling is given at the Z-Boson mass M_Z by

$$\alpha_s(M_Z) = 0.117 \pm 0.002. \tag{3.6}$$

Our focus now shifts exclusively towards unraveling the internal structure of the proton. Our review follows reference [28]. For the description of the underlying physical processes, it is common to use the Bjorken-x, which effectively quantifies the proportion of momentum held by the fundamental constituents, known as partons, relative to the proton's overall momentum.

As previously highlighted, deep inelastic scattering serves as a powerful tool for probing the underlying composition of the proton. This composition finds description through the proton's structure function denoted as F_a.

Utilizing the QCD factorization theorem [31] these structure functions can be universally expressed across all orders of DIS processes, as depicted by the following equation

$$F_a(x, Q^2) = \sum_{i=q,\bar{q},g} \int_0^1 \frac{\mathrm{d}y}{y} f_i(y, Q^2) C_{a,i}\left(x/y, \alpha_s(Q^2)\right) + O\left(\Lambda^2_{\mathrm{QCD}}/Q^2\right), \tag{3.7}$$

where y is linked to the scattering angle. Both variables x and y are confined within the range of 0 to 1. Notably, $y = 0$ corresponds to forward scattering, while $y = 1$ signifies backward scattering [28].

The factorization theorem facilitates the disentanglement of short-distance interactions from their long-distance counterparts within the process. In particular, the introduction of the universal parton density f_i accounts for the extended distance behavior, although its calculation eludes perturbative QCD methodologies. However, the energy-dependence can be appraised through the evaluation of a specific evolution equation.

The second component in equation (3.7), denoted as $C_{a,i}$, incorporates the short-distance characteristics of the processes. These short-distance behaviors are specific to each observable, while the long-distance behavior is deemed universal and unaffected by the particular process.

According to [28], it is noteworthy to highlight that the structure inherits a collinear divergence when the gluon is emitted parallel to the incoming quark, along with a soft divergence when the energy of the emitted gluon approaches zero.

$C_{a,i}$ can also be reformulated in the context of the splitting functions P, which can be deduced from the Feynman diagrams corresponding to particular processes. Further elaboration on the derivation is provided in [28].

For the forthcoming discourse, we introduce the common abbreviation for the convolution integral as

$$P \otimes f := \int_x^1 \frac{\mathrm{d}y}{y} f_q(y) P\left(\frac{x}{y}\right). \tag{3.8}$$

The energy dependency of the parton distribution functions (PDF), where we introduce the quark distribution denoted as $q = f_q$ and the gluon distribution as $g = f_g$, is delineated by the Dokshitzer-Gribov-Lipatov-Altarelli-Parisi (DGLAP) evolution equation [32]. For the quark distribution function q, this equation takes the form

$$\frac{\partial q(x,Q^2)}{\partial \log Q^2} = \frac{\alpha_s(Q^2)}{2\pi}\left(P_{qq}\otimes q + P_{qg}\otimes g\right), \tag{3.9}$$

where the splitting function P_{qg} signifies the transition from gluon to quark. The DGLAP equation for the gluon distribution function g is expressed as follows

$$\frac{\partial g(x,Q^2)}{\partial \log Q^2} = \frac{\alpha_s(Q^2)}{2\pi}\left(\sum_i P_{gq}\otimes(q_i+\bar{q}_i) + P_{gg}\otimes g\right). \tag{3.10}$$

The splitting functions can be generally represented as a series expansion in powers of α_s, given by

$$P_{ab}(\alpha_s, z) = P_{ab}^{LO}(z) + \alpha_s P_{ab}^{NLO}(z) + O(\alpha_s^2), \tag{3.11}$$

where ab represents the transition from state b to state a. When examining the initial state of the DGLAP equations, a challenge arises in determining $f(x, Q_0^2)$ through perturbative methods. Therefore, it is common to use a parameterization of the first moment of parton distribution function $xf(x, Q_0^2)$. Its common form is given by

$$xf(x,Q_0^2) = A\ x^{\delta}(1-x)^{\nu}(1+\epsilon\sqrt{x}+\gamma x). \tag{3.12}$$

In this equation, the parameter A is determined by adhering to summation rules, while δ and ν respectively delineate the influences at lower and higher values of x [33], with distinct values applicable to each individual parton. The values of ϵ and δ include higher-order effects.

The parametrization must adhere to the overall structure of the proton, which is predominantly governed by three primary sum rules. For the up-quarks, these rules manifest as follows

$$\int_0^1 (u-\bar{u})\,dx = \int_0^1 u_v\ dx = 2, \tag{3.13}$$

Similarly, for the down-quarks:

$$\int_0^1 \left(d-\bar{d}\right)dx = \int_0^1 d_v\ dx = 1. \tag{3.14}$$

In addition, the principle of momentum conservation must be fulfilled. Thus, we employ the first moment of the parton distribution functions as given

$$\int_0^1 \mathrm{d}z\ z\left(\sum_i \left[q_i(z,Q^2)+\bar{q}_i(z,Q^2)\right] + g(z,Q^2)\right) = 1. \tag{3.15}$$

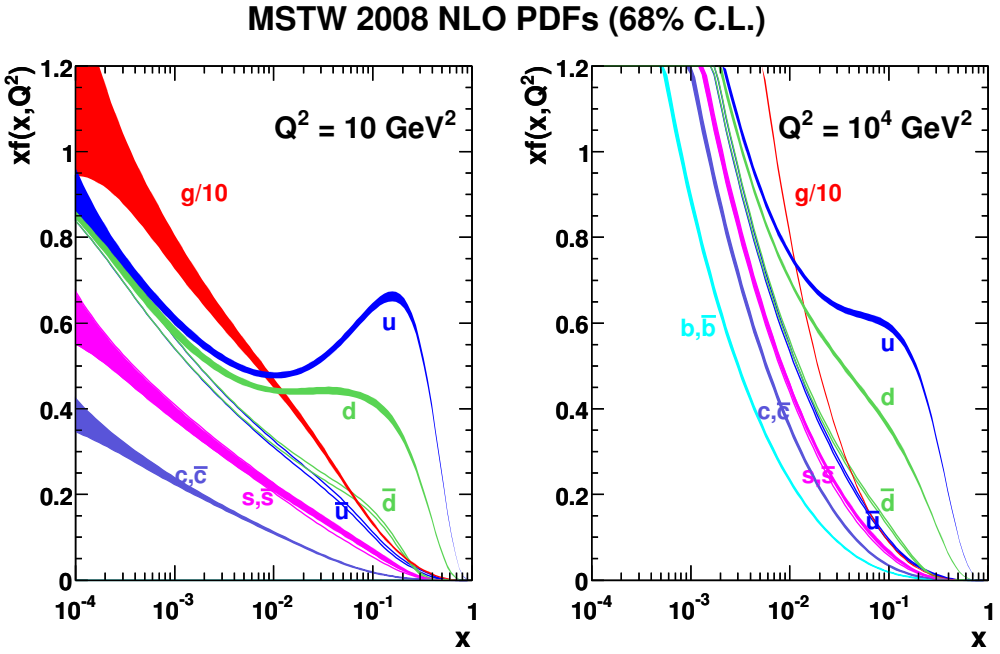

Figure 3.1.: Parton distribution functions (PDFs) for the proton at next-to-leading-order $xf(x, Q^2)$ using the Martin-Stirling-Thorne-Watt parametrization (MSTW 2008) are displayed at fixed energy scales: $Q^2 = 10\,\mathrm{GeV}^2$ and $10^4\,\mathrm{GeV}^2$. Figure taken from Martin [33].

This conservation requirement holds for all values of Q^2.

Numerous collaborations engage in the precise determination of the factors inherent to such parametrization. An illustration of the outcomes from one such parametrization is depicted in figure 3.1, showcasing the MSTW2008 parametrization [33] across two distinct energy scales. This specific parametrization will be employed in subsequent calculations.

Having established the parton distribution functions for quarks and gluons, the focus of our discourse now shifts toward elucidating the depiction of gluons exhibiting low fractional momentum in relation to the overall proton momentum.

3.2. Gluon saturation

In the domain characterized by low momentum fraction of gluons (small-x), the applicability of the DGLAP equation becomes limited. This leads to the emergence of an additional rapidity evolution that complements the conventional DGLAP evolution for the gluon distribution.

In the historical context, the Gribov-Levin-Ryskin (GLR) equation [34] is the first non-linear perturbative QCD evolution equation tailored to this specific scenario. It introduced the concept of parton recombination and the notion of saturation, thus extending the DGLAP evolution of the gluon distribution [35]. The formulation of this equation is as follows

$$\frac{\partial(xg)}{\partial \ln Q^2} = P_{gg} \otimes g + P_{gq} \otimes q - \frac{81\alpha_s^2}{16R^2Q^2} \int \frac{\mathrm{d}x'}{x'} \left[x' g\left(x', Q^2\right)\right]^2, \tag{3.16}$$

where x is the usual Bjorken scaling variable in DIS. The equation considers two gluon ladders recombining into a single gluon ladder, a fan diagram [28].

Further theoretical analyses have revealed that within the realm of small-x, gluons exhibit a high population density, leading in a dependence within the expansion of the splitting function $xP_{gg}(x)$ on both the coupling constant α_s and the logarithm of the reciprocal of x, represented as $\ln(1/x)$ [28]. Each term within this expansion takes the form

$$\alpha_s^n \ln^{n-1}(1/x). \tag{3.17}$$

In scenarios where the condition $\alpha_s \ln(1/x) \sim 1$ holds, the applicability of the DGLAP expansion for the splitting function becomes limited. This breakdown is particularly pronounced at low values of x. The second factor represents an alternate approach in defining the rapidity, denoted as Y. We utilize a distinct symbol here to emphasize the divergence in the origins of these definitions. The rapidity Y is expressed as follows

$$Y = \ln(x_0/x), \tag{3.18}$$

where x_0 serves as a gauge of the overall system energy. For $x = 1$, it correlates with the beam rapidity. In the literature, common values are either $x_0 = 1$ or $x_0 = 3 \times 10^{-4}$.

By adopting this definition, the process of resummation can be applied to the splitting function. Under the conjecture of logarithmic transverse momentum diffusion at small-x, coupled with the gluon density saturation within this region [28], the Balitsky-Fadin-Kuraev-Lipatov (BFKL) evolution equation [36, 37] surfaces as the governing equation for rapidity evolution. This equation is expressed for the gluon distribution f_g in the subsequent manner

$$\frac{\partial f_g}{\partial Y} = K \otimes f_g = \lambda f_g, \tag{3.19}$$

where K represents the BFKL kernel, and λ signifies its leading eigenvalue [28]. It is given by $\lambda = 12\alpha_s \ln 2/\pi$, and the solution can be represented as

$$f_g \sim \mathrm{e}^{\lambda \ln(x_0/x)} \sim (x/x_0)^{-\lambda}. \tag{3.20}$$

The interpretation of λ can be understood in terms of the emergence of propagating waves. The saturation front moves at a constant speed λ, which is equivalent to the exponential increase of the saturation momentum with Y [38].

This evolution indicates the emergence of a novel dynamic energy scale, denoting the saturation of the gluon distribution. We define the saturation scale Q_s in leading-order as

$$Q_s^2(Y) = Q_0^2 \mathrm{e}^{\lambda Y}, \tag{3.21}$$

where Q_0^2 is some non-perturbative initial scale and $\lambda \approx 4.9\alpha_s$ for fixed α_s [38]. An alternative computation yields $\lambda_{LO} \approx 4.8\alpha_s(Q^2)N_c/\pi$ [35]. Further analyses of λ are carried out in several literature sources, with particular emphasis on [39].

At high energies and rapidities, the condition $Q_s \gg \Lambda_{\mathrm{QCD}}$ holds for the saturation scale, implying that Q_s serves as the prevailing dynamic energy scale. Additionally, the running coupling $\alpha(Q_s)$ remains within the perturbative expansion regime, where $\alpha(Q_s) \ll 1$ [40].

When considering the effect of the running coupling α_s, the expression undergoes modification [38], resulting in

$$Q_s^2(Y) = Q_0^2 \mathrm{e}^{\sqrt{\lambda(Y+Y_0)}}, \tag{3.22}$$

where Q_0^2 and Y_0 are the corresponding initial conditions. Numerous additional expressions and calculations exist to ascertain the saturation scale. We restrict our attention to only one alternative solution, which also includes an energy dependence. Here, Q_s^2 is given as follows [41]

$$\ln\left(Q_s^2(Y,W)/\Lambda_{\mathrm{QCD}}^2\right) = \sqrt{2\lambda \ln\left(Q_0^2/\Lambda_{\mathrm{QCD}}^2\right)\left[\ln(W/W_0)+Y\right] + \ln^2\left(Q_s^2(W_0)/\Lambda_{\mathrm{QCD}}^2\right)}, \tag{3.23}$$

where $W = \sqrt{s_{NN}}$ and W_0 accounts for the initial energy.

The discourse concerning the theoretical determination of the saturation scale exponent λ remains incomplete at this juncture, owing to the existence of multiple values arising from next-leading-order eigenvalues and various BFKL kernels.

Another consideration that warrants investigation involves the proposition that the gluon distribution scales with $A^{1/3}$ for very large nuclei, as initially proposed in [42, 43]. The argument is as follows:

Although the color charge experiences screening, resulting in an average color charge of order $\sqrt{N}$, where N signifies the total color charge within each spatial region, the coherence of the color field results in a gluon density on the order of N. The density of valence quarks per unit transverse area is proportional to $A^{1/3}$. Consequently, the gluon density also follows a $A^{1/3}$ scaling [42].

A slightly different rationale for the $A^{1/3}$ proportionality, known as the so called *oomph* factor [35], is outlined in [44] as follows. Consider the wave function of a nucleus boosted to a high momentum, resulting in Lorentz contraction and confinement of partons to a thin sheet in the transverse plane.

Each parton occupies a transverse area of π/Q^2, governed by the uncertainty principle and its transverse momentum Q. This leads to a cross-section, which can be probed, of $\sigma \sim \alpha_s(Q^2)\pi/Q^2$. In contrast, the entire transverse area of the nucleus is $S_A \sim \pi R_A^2$. Consequently, if the number of partons N_A surpasses a threshold

$$N_A \sim \frac{S_A}{\sigma} \sim \frac{1}{\alpha_s(Q^2)} Q^2 R_A^2, \tag{3.24}$$

they begin to overlap within the transverse plane, initiating mutual interactions that impede the further growth of parton densities. This phenomenon occurs when the transverse momenta of the partons are on the order of

$$Q_s^2 \sim \alpha_s(Q_s^2)\frac{N_A}{R_A^2} \sim A^{1/3}, \tag{3.25}$$

which is called the saturation scale. We used that the transverse area scales like $A^{2/3}$. Building upon this assumption, we conclude our discussion of the saturation scale by presenting a refined definition for equation (3.21) as depicted below

$$Q_s^2\,(x) = A^{1/3} Q_0^2 (x/x_0)^{-\lambda}, \tag{3.26}$$

where we have utilized equation (3.18) to recast the expression in terms of the Bjorken-x. After having explored specific consequences of the BFKL equation in characterizing gluons, we proceed to investigate the theory of gluon saturation.

A key theoretical advancement in this context is represented by the Balitsky-Jalilian-Marian-Iancu-McLerran-Weigert-Leonidov-Kovner (B-JIMWLK) [45][46–56] evolution equation, which serves as the governing framework for the evolution of small-x QCD wavefunctions.

This equation is equivalent to an infinite set of coupled non-linear integro-differential evolution equations for the expectation values of the different correlators of Wilson lines averaged over the target gluon field configurations [57].

As outlined in [35], under the large-N_c limit, the complete B-JIMWLK hierarchy, specifically the Balitsky hierarchy as its alternative form, simplifies to a single, closed equation for the x-dependence of the dipole amplitude, known as the Balitsky-Kovchegov (BK) equation [45, 58]. This equation is the mean-field approximation [38] and represents the simplest non-linear $\ln(1/x)$ evolution equation in that hierarchy.

In its linear form, the BK equation corresponds to the BFKL equation, as mentioned in [40]. The BK equation can also be viewed as an expansion of the GLR equation, incorporating multiple-ladder recombination, as discussed in [59].

To further explore the BK equation, we can introduce the color dipole amplitudes using Wilson lines [60]. The dipole amplitude in the fundamental representation N_F, associated with the Wilson line V, is given by

$$N_F(\boldsymbol{x}_1, \boldsymbol{x}_2) \equiv \frac{1}{N_c} \mathrm{Tr}_c \left\langle V(\boldsymbol{x}_1) V^\dagger(\boldsymbol{x}_2) - 1 \right\rangle, \tag{3.27}$$

while the color dipole amplitude in the adjoint representation N_A, with Wilson line U, is defined as

$$N_A(\boldsymbol{x}_1, \boldsymbol{x}_2) \equiv \frac{1}{N_c^2 - 1} \mathrm{Tr}_c \left\langle U(\boldsymbol{x}_1) U^\dagger(\boldsymbol{x}_2) - 1 \right\rangle. \tag{3.28}$$

In this definition, we redefined $\boldsymbol{x}_1 = \boldsymbol{b} + \boldsymbol{r}_t/2$ and $\boldsymbol{x}_2 = \boldsymbol{b} - \boldsymbol{r}_t/2$, where $\boldsymbol{b}$ represents the impact parameter. Occasionally, this concept is also defined as the color dipole scattering matrix element, denoted as S, which is given by $N = 1 - S$, as seen in [61, 62]. For a more comprehensive understanding, we refer to [60] .

In the context of this research, we will refrain from delving into the detailed definition of Wilson lines due to the current limitations in obtaining meaningful results from such an approach. Instead, we will adopt a more pragmatic approach prevalent in contemporary literature by employing a phenomenological model to characterize the dipole amplitude.

By introducing a dependence on rapidity to the dipole amplitude and denoting it as $N_{\boldsymbol{xy}}(Y) \equiv N(\boldsymbol{x}, \boldsymbol{y}, Y)$, the BK equation can be expressed as provided in [28] by

$$\frac{\partial N_{\boldsymbol{xy}}}{\partial \ln Q^2} = \frac{N_c \alpha_s}{\pi} \int \frac{\mathrm{d}^2 \boldsymbol{z}}{2\pi} K(\boldsymbol{x}, \boldsymbol{y}, \boldsymbol{z}) \left[N_{\boldsymbol{xz}} + N_{\boldsymbol{yz}} - N_{\boldsymbol{xy}} - N_{\boldsymbol{xz}} N_{\boldsymbol{yz}} \right], \tag{3.29}$$

with the leading-order BK kernel [40] and $N_c = 3$ given by

$$K^{LO}(\boldsymbol{x}, \boldsymbol{y}, \boldsymbol{z}) = \frac{(\boldsymbol{x} - \boldsymbol{y})^2}{(\boldsymbol{x} - \boldsymbol{z})^2 (\boldsymbol{y} - \boldsymbol{z})^2}. \tag{3.30}$$

Including running coupling corrections to the BK (rcBK) equation translates into an improved kernel, called the rcBK evolution kernel [63, 64]. It is reviewed in [12] and with $\boldsymbol{r} = \boldsymbol{r}_1 + \boldsymbol{r}_2$ and $\boldsymbol{r} = \boldsymbol{x} - \boldsymbol{y}$, $\boldsymbol{r}_1 = \boldsymbol{x} - \boldsymbol{z}$ and $\boldsymbol{r}_2 = \boldsymbol{y} - \boldsymbol{z}$, given by

$$K^{run}(\boldsymbol{r}, \boldsymbol{r}_1, \boldsymbol{r}_2) = \frac{N_c \alpha_s(\boldsymbol{r}^2)}{2\pi^2} \left[\frac{1}{\boldsymbol{r}_1^2} \left(\frac{\alpha_s(\boldsymbol{r}_1^2)}{\alpha_s(\boldsymbol{r}_2^2)} - 1 \right) + \frac{\boldsymbol{r}^2}{\boldsymbol{r}_1^2 \boldsymbol{r}_2^2} + \frac{1}{\boldsymbol{r}_2^2} \left(\frac{\alpha_s(\boldsymbol{r}_2^2)}{\alpha_s(\boldsymbol{r}_1^2)} - 1 \right) \right]. \tag{3.31}$$

The middle term represents K^{LO}. An interesting observation is that $N_c/2\pi^2 = 0.152$, which is of the same order as $\alpha_s(Q^2)$ for $Q \sim 12\,\mathrm{GeV}$. The solution to the rcBK equation was obtained numerically in [65].

The nuclear unintegrated gluon distribution (UGD), necessary for hadron production in both k_T- and hybrid-factorization frameworks, is interconnected with the quark and gluon dipole scattering amplitudes through a two-dimensional Fourier transforms. The UGD is expressed [12] as follows

$$\varphi(k, \boldsymbol{R}, x) = \frac{C_F}{\alpha_s(k)(2\pi)^3} \int \mathrm{d}^2\boldsymbol{r}\ e^{-i\boldsymbol{k}\cdot\boldsymbol{r}}\ \nabla^2_{\boldsymbol{r}} N_A(\boldsymbol{r}, \boldsymbol{R}, x), \tag{3.32}$$

where x corresponds to the Bjorken scaling variable, related with the rapidity through equation (3.18). The transverse size of the dipole is denoted by $\boldsymbol{r}$, while $\boldsymbol{R}$ represents the transverse position at which the hadron target is probed. The parameter $\boldsymbol{k}^2$ specifies the scale of internal momentum transfer. We omit the vector notation and using only its magnitude here.

The function φ is dimensionless and signifies the quantity of gluons within a unit transverse area and a cell in transverse momentum space [12]. A slightly different definition can we found in [66], which defines the UGD as

$$\varphi(k, x) = \int \frac{\mathrm{d}^2\boldsymbol{r}}{2\pi\boldsymbol{r}^2}\ e^{-i\boldsymbol{k}\cdot\boldsymbol{r}}\ N_A(\boldsymbol{r}, x). \tag{3.33}$$

This definition can be seen as a specific realisation of equation (3.32) in case of $N_A \sim \exp\bigl(-r^2\bigr)$).

The connection between the gluon dipole scattering amplitude, which is essential for the unintegrated gluon distribution, and the quark dipole scattering amplitude can be formulated in the large-N_c limit as described in [12] as

$$N_A(\boldsymbol{r}, \boldsymbol{R}, x) = 2N_F(\boldsymbol{r}, \boldsymbol{R}, x) - N_F^2(\boldsymbol{r}, \boldsymbol{R}, x). \tag{3.34}$$

3.3. Models for the gluon

Having discussed the rapidity evolution of the color dipole amplitude, our attention now shifts towards elucidating the initial gluon distribution and reviewing specific solutions to the evolution equations. As an exact solution to one of the rapidity evolution equations is not presently available, we resort to employing phenomenological models to characterize the initial color dipole amplitude.

These models can be employed as initial conditions for either the rcBK equation or, from a historical perspective, the BFLK equation. Given the multitude of published models, our focus will be on specific ones. The initial model describing the color dipole amplitude is the McLerran-Venugopalan model [43]. This model is formulated as follows

$$N_A^{MV}(\boldsymbol{r}, Y = 0) = 1 - \exp\left[-\left(\frac{r^2 Q_{s,0}^2}{4}\right)^{\gamma} \ln\left(\frac{4}{r\ \Lambda_{\mathrm{QCD}}} + e\right)\right], \tag{3.35}$$

where $Q_{s,0}^2$ represents the initial saturation scale and γ stands for an anomalous dimension.

Another model, the Golec-Biernat and Wüsthoff (GBW) model, was independently introduced in [67, 68], albeit in a different formulation. This model utilizes the definition of the color dipole amplitude as follows

$$N_A^{GBW}(\boldsymbol{r}, Y = 0) = 1 - \exp\left[-\left(\frac{r^2 Q_{s,0}^2}{4}\right)\right], \tag{3.36}$$

resulting in the aforementioned GBW model, outlined in [69]. The original formulation of the model provides a definition for the unintegrated gluon distribution.

Another interesting model discussed in [40] is the Boer-Utermann-Wessels (BUW) model [70]. In this model, the color dipole amplitude is defined as follows

$$N_A^{BUW}(\boldsymbol{r}, Y = 0) = 1 - \exp\left[-\left(\frac{r^2 Q_{s,0}^2}{4}\right)^{\gamma(r,Y)}\right], \tag{3.37}$$

where $\gamma(r, Y)$ is also an anomalous dimension. Note that the model is a simple Glauber-like formula [71].

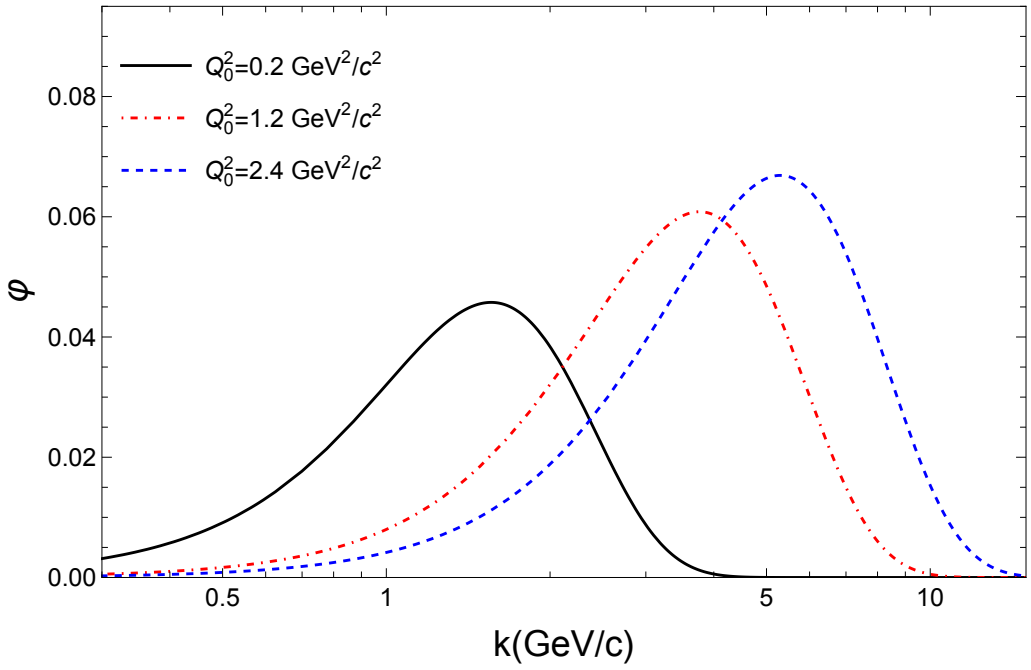

Figure 3.2.: The curves represent unintegrated gluon distributions $\varphi(k)$ calculated by the GBW model at three different energy scales, plotted as a function of momentum k.

In the subsequent discussion, we will substitute the initial saturation scale $Q_{s,0}$, which is defined at a specific rapidity, with the rapidity-dependent saturation scale $Q_s(Y)$. The specific form of this scale relies on the underlying evolution equation being considered. We will narrow down our further exploration to the solution of the BFLK equation, where the saturation scale takes the form of $Q_s(x)$ in terms of Bjorken-x, as described by equation (3.26).

Up to this point, the definitions of the color dipole amplitude have been established based on the transverse size $\boldsymbol{r}$. However, when applying these dipole amplitudes within the context of factorization, they need to be transformed into momentum space characterized by $\boldsymbol{k}$.

In accordance with [40] and [61], this transformation resembles that depicted in equation (3.32), and can be expressed as follows

$$\widetilde{N}_A(k,x) = \int \mathrm{d}^2\boldsymbol{r}\ \mathrm{e}^{i\boldsymbol{k}\cdot\boldsymbol{r}}\left(1 - N_A(r,x)\right). \tag{3.38}$$

Applying this transformation to the BUW model allows us to deduce analytical expressions for the adjoint dipole amplitude when γ takes on values of 1 and 1/2, as demonstrated in [60]. For the case of $\gamma = 1/2$, the dipole amplitude assumes the form

$$\widetilde{N}_A^{\gamma=1/2}(k^2,x) = \int \mathrm{d}^2\boldsymbol{r}\ \mathrm{e}^{i\boldsymbol{k}\cdot\boldsymbol{r}} N_A^{\gamma=1/2}(\boldsymbol{r}) = \frac{32\pi}{Q_s^2(x)}\left(1 + \frac{16k^2}{Q_s^2(x)}\right)^{-3/2}, \tag{3.39}$$

whereas for $\gamma = 1$, it takes the form

$$\widetilde{N}_A^{\gamma=1}(k^2,x) = \int \mathrm{d}^2\boldsymbol{r}\ \mathrm{e}^{i\boldsymbol{k}\cdot\boldsymbol{r}} N_A^{\gamma=1}(\boldsymbol{r}) = \frac{4\pi}{Q_s^2(x)} \exp\left(-k^2/Q_s^2(x)\right). \tag{3.40}$$

Using a definition analogous to that presented in equation (3.33), the unintegrated gluon distribution φ can be expressed as

$$\varphi(k,x) = k^2 \widetilde{N}_A\left(k,x\right). \tag{3.41}$$

This allows us to infer that $k^2 N_A^{\gamma=1}(k^2,x)$ corresponds to the original formulation of the GBW model, as discussed in [67, 68]. We expand upon the model by imposing the condition $\varphi \sim k^2/(3\pi^2\alpha_s(k^2))$ [72, 73], which leads us to the following expression for the gluon distribution

$$\varphi\left(k,x\right) = \frac{1}{3\pi^2\alpha_s(Q^2)} \frac{4\pi k^2}{Q_s^2(x)} \exp\left(-k^2/Q_s^2(x)\right). \tag{3.42}$$

The results of our calculation of the unintegrated gluon distribution using the GBW model are depicted in figure 3.2. The calculation employs equation (3.42) for the gluon distribution and equation (3.26) for the saturation scale, with parameters $x_0 = 3 \times 10^{-4}$, $A = 1$, and $\lambda = 0.288$ as specified in [67] . The diagram can be compared to similar calculations presented in [12] and [73]. For the calculation, a specific parametrization of the running coupling is employed, and its details will be provided at the end of this section.

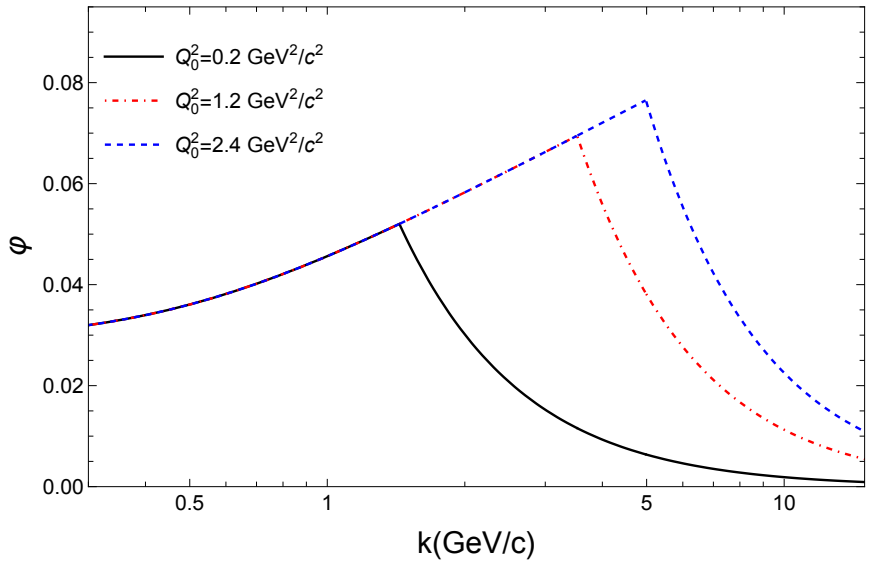

Figure 3.3.: The curves represent unintegrated gluon distributions $\varphi(k)$ calculated by the KLN model at three different energy scales, plotted as a function of momentum k.

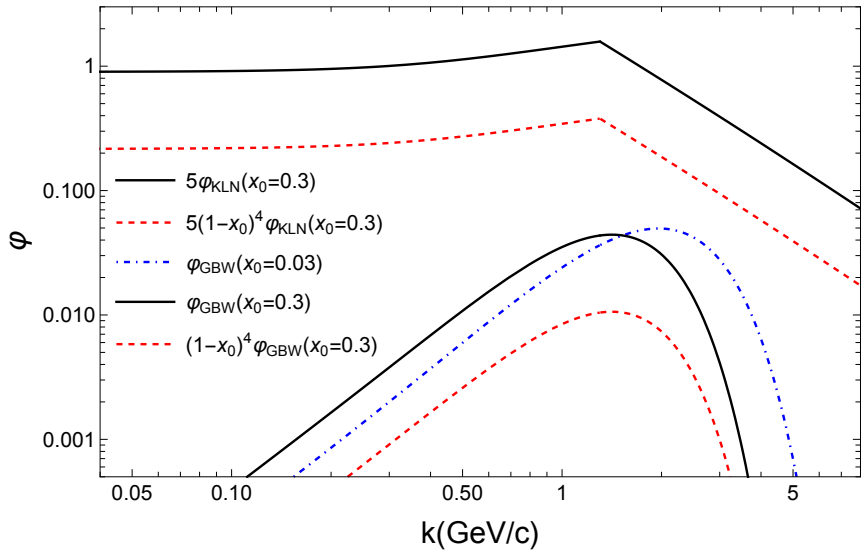

Figure 3.4.: Comparison of the unintegrated gluon distribution (UGD) $\varphi(k)$ obtained through calculations using the GBW and KLN models at $x_0 = 0.3$. To improve visibility, the KLN model results were magnified by a factor of 5. The solid curves correspond to the UGD without considering the large-x suppression factor, while the dashed curves depict the UGD with inclusion of the large-x suppression factor. The dot-dashed curve illustrates the UGD computed using the GBW model with $x_0 = 0.03$. The choice of $x_0 = 0.3$ represents a typical large-x value, and $x_0 = 0.03$ reflects the variation in the UGD within the GBW model as the parameter x_0 decreases.

The final model which we present is the Kharzeev-Levin-Nardi (KLN) model [41, 44, 72, 74, 75]. The exposition of this model is based on [76]. It establishes the unintegrated gluon distribution φ based on the corresponding bremsstrahlung radiation spectrum [72] for momenta greater than the saturation scale. It can be formulated as

$$\varphi_{\mathrm{KLN}}(k,x) := \begin{cases} \dfrac{2C_F}{3\pi^2\alpha_s(Q^2)}, & k^2 \leq Q_s^2(x) \\ \dfrac{2C_F}{3\pi^2\alpha_s(Q^2)}\dfrac{Q_s^2(x)}{k^2}, & k^2 > Q_s^2(x). \end{cases} \tag{3.43}$$

The parameter k^2 defines the internal momentum transfer scale, and x corresponds to the Bjorken scaling variable, connected to the rapidity through equation (3.18).

The color factor C_F establishes the probability associated with a gluon's interaction with a quark. For the number of colors $N_c = 3$, it can be expressed as

$$C_F := \frac{N_c^2 - 1}{2N_c} = 4/3. \tag{3.44}$$

This coefficient is also evident in earlier studies, such as [44] , and the structure of this model can also be observed in equations derived in [77] and [78]

The outcomes of our computation regarding the unintegrated gluon distribution utilizing the KLN model are illustrated in figure 3.3. The calculation makes use of equation (3.43) to represent the gluon distribution and equation (3.26) for the saturation scale, with specific parameters being $x_0 = 3 \times 10^{-4}$, $A = 1$, and $\lambda = 0.288$. However, it is necessary to rescale the results by a factor of $1/2\pi$ in order to align them with the range of the GBW model employing the same parameters.

The applicability of this presented formalism is anticipated to be limited to small values of x. Incorporating this condition into practical calculations is not straightforward. To mitigate the impact of contributions from large-x, an additional factor is introduced, leading to a modification of the KLN model as follows

$$\varphi^*_{\mathrm{KLN}}(k,x) = (1-x)^4\,\varphi_{\mathrm{KLN}}(k,x)\,. \tag{3.45}$$

The rationale behind introducing this factor is to reduce overcounting for large value of x, which adheres to quark counting rules [79, 80] and aims to simulate the behaviour of the distribution as x approaches 1.

This factor can also be applied to various models, such as the GBW model. Figure 3.4 illustrates the impact of this suppression factor on both the GBW and KLN models, utilizing the same model parameters as in figure 3.2 and 3.3.

For these calculations, a similar approach is taken for the running of the strong coupling constant as in [12]. It is defined by

$$\alpha_s(r^2) = \frac{4\pi}{\beta \ln\left(\frac{4C^2}{r^2\Lambda^2_{\mathrm{QCD}}} + \mu\right)}, \tag{3.46}$$

where $\beta = 11 - 2/3N_f = 9$ with $N_f = 3$ and $\Lambda_{\mathrm{QCD}} = 0.241\,\mathrm{GeV}$. The parameter is introduced to regulate the strong coupling for large dipole sizes and is determined by the condition $\alpha_s(\infty) = \alpha_{fr} = 0.5$ [12], resulting in $\mu = 16.322$. A very similar but slightly different parametrization of the strong coupling constant can also be found in [11].

We can substitute r^2 with $1/k^2$ in equation 3.46, as it presupposes the application of α_s prior to performing the Fourier transformation required for computing the unintegrated gluon distribution from the dipole amplitude. Consequently, it is permissible to assign a value of $C = 1$, as this adjustment considers the inherent uncertainty associated with the Fourier transform, as elucidated in [12]. Therefore, our parametrization of α_s is expressed as follows:

$$\alpha_s(k^2) = \frac{4\pi}{\beta \ln\left(\frac{4k^2}{\Lambda^2_{\mathrm{QCD}}} + \mu\right)}. \tag{3.47}$$

In this chapter, we have examined the parton model's description of quarks and gluons, focusing on its energy dependence within a nucleus. Furthermore, we introduced the concept of gluon saturation and explored the behaviour of gluons at small-x. Lastly, we discussed two models that provide descriptions of the unintegrated gluon distribution. In the subsequent chapter, our attention will turn towards the factorization that facilitate the description of hadron production by combining insights from the parton model and gluon saturation.

4. Charged-hadron production

After providing an overview of deep inelastic scattering and revisiting certain aspects of the parton model, which encompass the characterization of quarks and gluons confined within a proton, our attention now shifts towards investigating the cross section associated with charged-hadron production.

The chapter commences with the presentation of the factorization theorem, followed by the introduction of two distinct factorization schemes. These include the k_T-factorization for interactions involving gluon-gluon interactions, and the hybrid-factorization for interactions involving quarks-gluons interactions. Both of these schemes carry substantial importance in providing a comprehensive description of charged-hadron production in heavy-ion collisions.

The complexity of QCD calculations is notably high, especially when considering both initial and final hadron states. In the context of a scattering process, the ability to untangle the cross section of the entire process into distinct, independent components would be of immense utility. This involves segregating the cross sections associated with hard and soft processes.

Fundamentally, the capacity to disentangle cross sections dependent on short-range processes from those that exhibit universal and long-range characteristics would be highly advantageous. This property is commonly known as factorization. A formal proof that QCD exhibits such factorization is provided in [81].

In the context of this work, our goal is to describe hadron production resulting from heavy-ion collisions. Consequently, our focus is solely on hard processes. The QCD factorization of hard processes has already been investigated in [31].

Our approach begins with a simpler collision, namely electron-hadron scattering. From this foundation, we can extrapolate the factorization of cross sections for more complex collisions.

Based on [31], we establish a parallel definition, akin to that in section 3.1, of a parton distribution denoted as $f_{a/H}(\xi)$. This distribution represents the likelihood that an electron will interact with a non-interacting parton of species a, carrying a fraction ξ of the hadron's momentum. We consider the cross section for the interaction of an electron with such a parton, characterized by a momentum transfer Q^2, as the Born cross section $\sigma_B(Q^2, \xi)$.

When considering free partons, where the condition $\xi > x \equiv 2p \cdot q/Q^2$ holds, it results in the total cross section for deep inelastic scattering of a hadron by an electron:

$$\sigma_{eH}(x, Q^2) = \sum_a \int_x^1 \mathrm{d}\xi \; f_{a/H}(\xi)\sigma_B\left(x/\xi, Q^2\right). \tag{4.1}$$

This expression represents the parton model cross section for deeply inelastic scattering, as described in [31].

As mentioned in [31], the Drell-Yan cross section serves as a significant example, elucidating hadron-hadron scattering that results in the production of a pair of leptons in the final state. By adapting this cross section to the parton model framework, the process is given by direct annihilation of a parton and anti-parton pair, sourced from each of the interacting hadrons, within the Born approximation, denoted as $\sigma'_B(Q^2, y)$.

The interactions responsible for producing the distributions of these individual partons occur on a timescale much longer than that of annihilation. Furthermore, final-state interactions involving the remaining partons occur too late to influence the annihilation process [31]. Consequently, we extend the expression given in equation (4.1) to encompass the parton model description of the Drell-Yan cross section, which is given in [31] as

$$\frac{\mathrm{d}\sigma}{\mathrm{d}Q^2\mathrm{d}y} = \sum_a \int_{x_A}^1 \mathrm{d}\xi_A \int_{x_B}^1 \mathrm{d}\xi_B \; f_{a/A}(\xi_A) \; f_{\bar{a}/B}(\xi_B) \; \sigma'_B(Q^2, y), \tag{4.2}$$

where x_A and x_B are given by

$$x_A = \exp(+y)\sqrt{Q^2/s}, \qquad x_B = \exp(-y)\sqrt{Q^2/s}. \tag{4.3}$$

An essential point to highlight is that the Lorentz contraction of the hadrons in the center of mass frame of reference is an important factor for achieving the universality of parton distributions [31]. Building upon this definition, we can now introduce the ideas of k_T-factorization and hybrid-factorization.

4.1. The k_T-factorization

In the realm of charged-hadron production in high-ion collisions at relativistic energies, the k_T-factorization becomes highly important. This is because a significant number of the resulting hadrons are expected to be well explained by this idea and the related gluon-gluon interactions.

The foundation of k_T-factorization traces its origins to [82–86], whereas the factorized form of the inclusive cross section, is mentioned in [87], which takes the following form

$$\frac{\mathrm{d}\sigma}{\mathrm{d}y\mathrm{d}^2\boldsymbol{k}_T} = \frac{2\alpha_s}{C_F\boldsymbol{k}_T^2}\int \mathrm{d}^2\boldsymbol{k}_T\ \frac{f_A(\xi_A,\boldsymbol{k}_T^2)\ f_B(\xi_B,|\boldsymbol{k}_T-\boldsymbol{q}_T|^2)}{q_T^2(\boldsymbol{k}_T-\boldsymbol{q}_T)^2}. \tag{4.4}$$

Here, ξ_A and ξ_B represent the values of the Bjorken-x variable corresponding to the gluons in each of the colliding particles. The symbol C_F is defined as given in equation equation (3.44).

The unintegrated gluon distributions, denoted as $f_A(\xi_A,\boldsymbol{q}_T^2)$ and $f_B(\xi_B,|\boldsymbol{k}_T-\boldsymbol{q}_T|^2)$, are the probability to find a gluon that carries ξ fraction of energy with $\boldsymbol{k}_T$ transverse momentum in the projectile or target [10]. It is in general given by equation (3.32). A different definition can be found in [35]

$$\begin{aligned}\frac{\mathrm{d}\sigma^{A+B\to g}}{\mathrm{d}y\mathrm{d}^2\boldsymbol{p}_T\mathrm{d}^2\boldsymbol{R}\mathrm{d}^2\boldsymbol{b}} =& \frac{2}{C_F\boldsymbol{p}_T^2}\int\frac{\mathrm{d}^2\boldsymbol{k}_T}{4}\ \times \\ & \alpha_s(Q)\ \varphi_A\left(\frac{|\boldsymbol{p}_T+\boldsymbol{k}_T|^2}{2},b\right)\varphi_B\left(\frac{|\boldsymbol{p}_T-\boldsymbol{k}_T|^2}{2},R-b\right),\end{aligned} \tag{4.5}$$

which is also based on equation (4.4) but uses a slightly different definition of the unintegrated gluon distribution, given by $\varphi_i(k^2)\sim f_i(k^2)/k^2$. The sightly difference in the definition can also be found in [60].

We introduced a abbreviation to make the equation more readable: $\varphi_i\equiv\varphi_i(x_i)$. The definitions of x_A and x_B follow from equation (4.3) and adjusting to the context of heavy-ion collisions. This indicates that the Bjorken-x are defined by

$$x_A = \frac{m_T}{\sqrt{s_{NN}}}\mathrm{e}^{y}, \qquad\qquad x_B = \frac{m_T}{\sqrt{s_{NN}}}\mathrm{e}^{-y}. \tag{4.6}$$

This also shows that the definition is similar to equation (2.20) with $p_T=0$. equation (4.5) uses the definition of 4.6 but with $m=0$.

The employed model for computing charged-hadron production via k_T-factorization is a hybrid combination of these approaches. In contrast to considering impact-parameter-dependent unintegrated gluon distributions, our approach involves scaling the cross-section by the number of participants.

It's important to note that in the context of asymmetric collisions, two distinct processes must be calculated: $A+B\to g$ and $B+A\to g$. It can be seen by applying our model to symmetric collisions.

The final expression defining the production of charged hadrons in asymmetric collisions is as follows

$$\frac{\mathrm{d}^3 N_{gg}^h}{\mathrm{d}y \mathrm{d}\boldsymbol{p}_T^2} = \frac{2}{C_F} \frac{\alpha_s(\boldsymbol{m}_T^2)}{\boldsymbol{m}_T^2} \int_0^{p_T} \mathrm{d}\boldsymbol{k}_T^2 \Big[N_1 \varphi_1 \left(x_1, \boldsymbol{k}_T^2\right) \varphi_2 \left(x_2, |\boldsymbol{m}_T - \boldsymbol{k}_T|^2\right) + N_2 \varphi_2 \left(x_2, \boldsymbol{k}_T^2\right) \varphi_1 \left(x_1, |\boldsymbol{m}_T - \boldsymbol{k}_T|^2\right) \Big]. \tag{4.7}$$

We employ the model for the unintegrated gluon distribution outlined in (3.43,) incorporating the suppression factor as described in (3.45), and also utilize the model discussed in (3.42) for subsequent calculations.

In terms of the scale for the running of α_s, we adopt the internal momentum scale Q^2 defined within the unintegrated gluon distribution, which can take on values of either $Q^2 = \boldsymbol{k}_T^2$ or $|\boldsymbol{m}_T - \boldsymbol{k}_T|^2$. This choice is supported by the discussions found in [76] and [73].

4.2. The hybrid-factorization

In this section, certain aspects of the parton model are revisited, as previously discussed in chapter 3. However, the primary emphasis now shifts towards examining the interactions between quarks and gluons.

To examine the spectrum of produced hadrons in the forward direction near the beam rapidity, a comprehensive analysis of multiple Feynman diagrams is essential, as illustrated in [60]. We follow the derivation of [60] in this section. The pertinent Feynman diagrams incorporate recoil effects in gluon production. The accumulation of these diagrams results in the subsequent expression

$$\int_x^1 \frac{\mathrm{d}\xi}{\xi} \left\{ q_0(x/\xi) \left(\delta(1-\xi) + \frac{\alpha_s}{2\pi} \log \frac{Q^2}{\Lambda^2} P_{q/q}(\xi) \right) + g_0(x/\xi) \frac{\alpha_s}{2\pi} \log \frac{Q^2}{\Lambda^2} P_{q/g}(\xi) \right\} N_F(\xi, k_t, b), \tag{4.8}$$

where $q_0(x/\xi)$ and $g_0(x/\xi)$ represent the bare (parton model) quark and gluon distribution functions, as documented in [60]. $P_{q/q}$ and $P_{q/g}$ stand for the DGLAP splitting functions, detailing transitions from quark species to quark species and from gluons to quark species, which are also defined section 3.1.

Here, x denotes the momentum fraction of the initial parton, while ξ signifies the momentum fraction of a produced gluon. The fundamental and adjoint representations of the dipole cross section are denoted $N_{F/A}$ Additionally, k_t represents the transverse momentum, and the impact parameter dependence is captured by b.

These combined splitting functions can be integrated into the quark distribution function of a proton, denoted as $f_{q/p}(x/\xi, Q^2)$, subsequent to utilizing the DGLAP evolution equation. Employing the convolution symbol $\otimes$, we can express (4.8) as

$$f_{q/p}(x/\xi, Q^2) \otimes N_F\left(\xi, p_T, b\right). \tag{4.9}$$

This encompasses the integration over the momentum fraction of produced gluons. Upon considering an alternate set of Feynman diagrams, a parallel equation is derived for the gluon distribution function within a proton after incorporating the DGLAP evolution

$$f_{g/p}(x/\xi, Q^2) \otimes N_A\left(\xi, p_T, b\right). \tag{4.10}$$

In this case, the dipole amplitude N_A utilizes the adjoint representation, as opposed to the fundamental representation. This approach is similarly applied to two additional sets of Feynman diagrams, encompassing the basic fragmentation functions for quarks and gluons, denoted as $D_q^0(x/\xi)$ and $D_g^0(x/\xi)$. This leads to the expressions

$$D_q(x/\xi, Q^2) \otimes \widetilde{N}_F\left(\xi, k_t, b\right), \tag{4.11}$$

and

$$D_g(x/\xi, Q^2) \otimes \widetilde{N}_A\left(\xi, k_t, b\right), \tag{4.12}$$

where we used

$$\widetilde{N}_{F,A}\left(\xi, k_t, b\right) \equiv N_{F,A}\left(\xi, k_t/\xi, b\right)/\xi^2. \tag{4.13}$$

By combining these successive stages, the representation of one-parton radiation can be encapsulated within a unified equation, expressed as

$$\begin{aligned} f_q(Q^2) \otimes N_F \otimes D_q^0 + q^0 \otimes \widetilde{N}_F \otimes D_q(Q^2) \\ + f_g(Q^2) \otimes N_A \otimes D_g^0 + g^0 \otimes \widetilde{N}_A \otimes D_g(Q^2). \end{aligned} \tag{4.14}$$

Here, the convolution is performed over the variable x. The inclusion of additional contributions results in equation (4.14) evolving into a comprehensive representation at the one-loop order, expounded in detail in Appendix A of [60].

We establish a connection between the complete result at the one-loop order and the cross section, as discussed in [88], yielding the following expression for the cross section of asymmetric proton-nucleus scattering

$$\begin{aligned} x_F \frac{\mathrm{d}\sigma\left(pA \to hX\right)}{\mathrm{d}x_F\ \mathrm{d}p_T^2\ \mathrm{d}b^2} = & \frac{1}{(2\pi)^2} \int_{x_F}^1 \mathrm{d}x_p \frac{x_p}{x_F} \Bigg[\\ & f_{q/p}\left(x_p, Q_f^2\right) N_F\left(\frac{x_p}{x_F} p_T, b\right) D_{h/q}\left(\frac{x_F}{x_p}, Q_f^2\right) \\ & + f_{g/p}\left(x_p, Q_f^2\right) N_A\left(\frac{x_p}{x_F} p_T, b\right) D_{h/g}\left(\frac{x_F}{x_p}, Q_f^2\right) \Bigg], \end{aligned} \tag{4.15}$$

where A represents the nucleus and h stands for the produced hadron. The fragmentation scale is designated as Q_f^2, and x_F denotes the Feynman-x, which is defined as

$$x_F = xp_T/k_T, \tag{4.16}$$

where p_T signifies the transverse momentum of the produced hadron and k_T symbolizes the transverse momentum of the parton [89]. For further exploration, we integrate over the impact parameter and utilize an effective impact parameter denoted as $\langle b \rangle$, which corresponds to the minimum bias centrality.

Now, we proceed to specify the gluon dipole amplitude N. Assuming that we are operating in the small-x regime and considering the saturation of the gluon distribution function, we can define an effective saturation scale for a given effective impact parameter $\left\langle Q_s^2(b) \right\rangle$. With this dynamically varying energy scale, as widely discussed in section 3.2, we can express equation (4.15) for large rapidities [90] as

$$\begin{aligned} \frac{\mathrm{d}N_{m.b.}}{\pi\ \mathrm{d}y_h\ \mathrm{d}p_T^2} = \ & \frac{1}{(2\pi)^2} \int_{x_F}^1 \mathrm{d}x_p \frac{x_p}{x_F} \Bigg[\\ & f_{q/p}\left(x_p, Q_f^2\right) N_F\left(\frac{x_p}{x_F} p_T, y_A, \left\langle Q_s^2(b) \right\rangle\right) D_{h/q}\left(\frac{x_F}{x_p}, \mu_f^2\right) \\ & + f_{g/p}\left(x_p, Q_f^2\right) N_A\left(\frac{x_p}{x_F} p_T, y_A, \left\langle Q_s^2(b) \right\rangle\right) D_{h/g}\left(\frac{x_F}{x_p}, \mu_f^2\right) \Bigg], \end{aligned} \tag{4.17}$$

where μ_f represents the fragmentation scale of the fragmentation function. We can proceed to analyse this equation further following the methodology presented in [91]. To begin, we establish the fraction z of quark energy carried by the produced hadrons as follows

$$z(x) := x_F/x, \tag{4.18}$$

where $z(1) = x_F$ and $z(x_F) = 1$ serve as the boundary conditions. For the sake of completeness, the differential $\mathrm{d}z$ is expressed as follows

$$\mathrm{d}x/x_F = -x^2/x_F^2 \mathrm{d}z = -\mathrm{d}z/z^2. \tag{4.19}$$

Moreover, considering massive constituents that contribute an additional portion of the transverse momentum, we can define an effective transverse momentum, denoted as q_T, by

$$q_T := m_T/z = \sqrt{p_T^2 + m^2}/z. \tag{4.20}$$

After using the last three steps, equation (4.17) can be rearranged to

$$\begin{aligned} \frac{\mathrm{d}N(pA \to hX)}{\pi\ \mathrm{d}y_h\ \mathrm{d}^2 p_T} = & \frac{1}{(2\pi)^2} \int_{x_F}^1 \frac{\mathrm{d}z}{z^2} \Bigg[\\ & D_{h/q}\left(z, \mu_f^2\right) x_p f_{q/p}\left(x_p, Q_f^2\right) \frac{1}{q_T^2} \varphi_F\left(y_A, q_T\right) \\ & + D_{h/g}\left(z, \mu_f^2\right) x_p f_{g/p}\left(x_p, Q_f^2\right) \frac{1}{q_T^2} \varphi_A\left(y_A, q_T\right) \Bigg]. \end{aligned} \tag{4.21}$$

This equation coincides with the one presented in [92], after rearranging the variables z and q_T. Furthermore, we employ a similar relationship between the unintegrated gluon distributions as outlined in equation (4.13).

Inspired by [93], the final equation we utilize to compute the single-inclusive hadron production, considering solely valence quark-gluon scattering, is expressed by

$$\frac{\mathrm{d}^3N}{\mathrm{d}y_h\mathrm{d}^2p_T} = \frac{K}{(2\pi)^2}\frac{1}{m_T^2}\int_{x_F}^{1}\mathrm{d}z\; D_{h/q}\left(z,\mu_f^2\right)x_p f_{q/p}\left(x_p,Q_f^2\right)\varphi_F\left(y_A,q_T\right), \tag{4.22}$$

where we use $Q_f^2 = \mu_f^2 = p_T^2$. The K-factor is introduced to account for higher-order corrections and additional dynamical effects that are not encompassed within the hybrid framework, as mentioned in [40], and includes a factor of order 2π that is required to make k_T- and hybrid-factorization consistent with each other in the context of our Relativistic Diffusion model.

As previously stated, asymmetric collisions necessitate separate calculations for both fragmentation sources by interchanging the roles of the projectile and target. In this context, we adjust the parton distribution functions of the nucleus by scaling them with the number of participants as follows

$$x_A f_{q/A} = N_{\mathrm{part}}\; x_p f_{q/p}, \tag{4.23}$$

which is similarly indicated by [94]. It is important to highlight that φ_F corresponds to the adjoint representation, as elucidated in equation (3.34), which leads to an additional scaling of the saturation scale as follows [41, 71, 74, 94]

$$Q_s^2 \to \frac{N_C}{C_F}Q_s^2 = \frac{4}{9}Q_s^2. \tag{4.24}$$

This chapter outlined two factorization schemes, which can be utilized for describing rapidity distributions for charged-hadron production at relativistic heavy-ion collisions.

5. Diffusion approach to charged-hadron production

In this chapter, we present an non-equilibrium statistical model known as the Relativistic Diffusion model (RDM). The foundation of this model rests upon the assumption that the underlying microscopic processes exhibit Markovian characteristics. Formulated in one dimension, the RDM draws from the Uhlenbeck-Ohrnstein process as its theoretical framework.

The employed Uhlenbeck-Ohrnstein process facilitates the transition from initial distributions, motivated by stopping phenomena, to distributions that describe hadron production.

5.1. The Fokker-Planck equation

Statistical distribution functions serve as a foundational framework for elucidating the behaviour of physical processes. The intricate nature of these processes allows for the formulation of diverse assumptions regarding the underlying microscopic dynamics. The Markov process holds a preeminent status among stochastic processes. It can be locally defined within the framework of differential equations, as well as globally expounded through the application of integrals.

The global equation for Markov processes is called the Chapman-Kolmogorov equation [95] and is expressed through transition probabilities

$$p_2(x_3|x_1) = \int \mathrm{d}x_2 p_2(x_3|x_2) p_2(x_2|x_1), \tag{5.1}$$

with x_i denoting abstract states.

Interpretation of this can be elucidated as follows: The likelihood of state x_3 materializing subsequent to the occurrence of state x_1 is calculable by considering the probabilities associated with all intermediary states x_2. In the domain of field theory, the transition probability p_2 is also known as the propagator.

For the purpose of resolving solutions within the context of the Chapman-Kolmogorov equation, the introduction of a local formulation proves advantageous. For this

work, we exclusively employ the one-dimensional representation of the Chapman-Kolmogorov equation.

It is important to note that the Chapman-Kolmogorov equation assumes the form of an integral equation, and its inherent global nature renders the task of solution derivation challenging. Nevertheless, it becomes feasible to convert it into a localized equation by imposing suitable assumptions that pertain to the behaviour on short time scales.

In pursuit of the derivation of the localized expression for the Chapman-Kolmogorov equation, we postulate that the first moment of the statistical distribution function is proportional to Δt, yielding the relationship

$$\int \mathrm{d}x_2 \, (x_2 - x_1) \, p_2(x_2, t + \Delta t | x_1, t) = J(x_1, t)\Delta t + O(\Delta t^2). \tag{5.2}$$

The term $J(x_1, t)$ is identified as the drift function. Similarly, for the second moment, we assume a proportionality to Δt, resulting in

$$\int \mathrm{d}x_2 \, (x_2 - x_1)^2 \, p_2(x_2, t + \Delta t | x_1, t) = 2D(x_1, t)\Delta t + O(\Delta t^2), \tag{5.3}$$

where $D(x_1, t)$ denotes the diffusion function. The presence of a factor of two preceding the diffusion function is a conventional choice.

Combining of these two expressions culminates in a localized equation that characterizes the Markov process. Later, we use this equation in rapidity space. Therefore, we rename the variable x to y. To further align with the intended usage, we rename the statistical distribution function to $R(y, t)$. As a consequence, we arrive at the formulation of the localized Chapman-Kolmogorov equation in one dimension [96]:

$$\left(\frac{\partial}{\partial t} + \frac{\partial}{\partial y} J(y, t) - \frac{\partial^2}{\partial y^2} D(y, t) \right) R\,(y, t) = 0. \tag{5.4}$$

This equation is called the Fokker-Planck equation. An insightful article discussing this equation is available in [97].

In the context of our analysis, centered on the evolution of rapidity distributions in heavy-ion collisions, we make two physical assumptions. The first assumption pertains to the constancy of the diffusion coefficient, denoted by D. This coefficient encapsulates the underlying microscopic physics, which is anticipated to exhibit time- and rapidity-independence, as emphasized in [98], leading to the expression

$$\frac{\partial}{\partial t} R(y, t) + \frac{\partial}{\partial y} [J(y) R(y, t)] - D_y \frac{\partial^2}{\partial y^2} R(y, t) = 0 \tag{5.5}$$

Based on the conjecture that the stationary solution adheres to a relativistic Boltzmann distribution, the characterization of the drift term $J(y)$ can be deduced [99] yielding the expression

$$J(y) = -\frac{m_T D}{T} \sinh(y), \tag{5.6}$$

where m_T is defined as in equation (2.23) and T denotes the temperature T. In the following step, we embark on a perturbative expansion of the drift term up to the leading order. This expansion leads to the concept known as the relaxation ansatz [100], in which the drift term assumes the form

$$J(y) = \frac{y_{\mathrm{eq}} - y}{\tau_{\mathrm{y}}}. \tag{5.7}$$

Here, τ_{y} represents the rapidity relaxation time, dictating the temporal trajectory by which the system converges to thermal equilibrium. Furthermore, y_{eq} designates the specific rapidity value at which the system reaches thermal equilibrium. Notably, this value differs from zero solely in the context of asymmetric collisions.

The study conducted in [101] demonstrated that the discrepancies between the solutions derived from the full drift term and the drift term augmented with the relaxation ansatz are negligibly small within the localized region of the solution.

Furthermore, the solution for the linear Fokker-Planck equation with the relaxation ansatz can be expressed analytically. This fact prompts us to proceed with this assumption for our further analysis. The Fokker-Planck equation incorporating the relaxation ansatz is presented as follows

$$\frac{\partial}{\partial t} R(y,t) = -\frac{1}{\tau_y} \frac{\partial}{\partial y} [(y_{\mathrm{eq}} - y) R(y,t)] + D_y \frac{\partial^2}{\partial y^2} R(y,t). \tag{5.8}$$

The derived equation corresponds to a significant physical phenomenon known as the Uhlenbeck-Ohrnstein process [102]. This linear Focker-Planck equation is associated with an underlying dynamics featuring a positive harmonic potential centered at y_{eq}. Given a specific initial state positioned at $y_{\max}$, the distribution function's locality extends towards y_{eq}.

Furthermore, the derivation of the diffusion coefficient D can be accomplished using the dissipation-fluctuation theorem, also known as the Einstein relation. This relation is expressed as follows

$$D_y = \alpha T \simeq f\left(\tau_y, T\right), \tag{5.9}$$

where T signifies the temperature of the equilibrium distribution. The function f can be elaborated upon, leading to an analytical expression for the diffusion term as demonstrated in [13]:

$$D_y(\tau_y, T) = \frac{1}{2\pi\tau_y} \left[c(\sqrt{s}, T) m^2 T \left(1 + 2\frac{T}{m} + 2\frac{T}{m}\right)^2 \right]^{-2} \exp\left(\frac{2m}{T}\right), \tag{5.10}$$

with the proton mass m. A comprehensive formulation for $c(\sqrt{s}, T)$ can be also found in [13].

The subsequent section will encompass the presentation and assessment of the analytical solution to this linear Fokker-Planck equation under specific initial conditions.

5.2. Solution of the linear Fokker-Planck equation

The linear Fokker-Planck equation can be analytically solved for various initial conditions. Let us begin by considering an out-of-equilibrium initial state. Specifically, we examine the initial condition where the distribution $R(y,t)$ at $t = 0$ is concentrated around a distinct value $y = y_{\max}$, with $y_{\max} \neq y_{\text{eq}}$, described by the expression

$$R(y,0) = \delta\left(y \mp y_{\max}\right). \tag{5.11}$$

The solution for the linear Fokker-Planck equation can be achieved through a Fourier transformation, as demonstrated in [101]. In this approach, $\widetilde{R}(k,t)$ represents the Fourier transform of $R(y,t)$. The resulting equation becomes

$$\frac{\partial}{\partial t}\widetilde{R}(k,t) + \frac{k}{\tau_y}\frac{\partial}{\partial k}\widetilde{R}(k,t) = \left[\frac{ik}{\tau_y}y_{\text{eq}} - k^2 D_y\right]\widetilde{R}(k,t). \tag{5.12}$$

By applying the method of characteristics, we transform the partial differentials ∂_y and ∂_t into total differentials $\mathrm{d}s$, using the expression

$$\frac{\mathrm{d}\widetilde{R}(k(s),t(s))}{\mathrm{d}s} = \frac{\partial\widetilde{R}(k,t)}{\partial t}\frac{\mathrm{d}t}{\mathrm{d}s} + \frac{\partial\widetilde{R}(k,t)}{\partial k}\frac{\mathrm{d}k}{\mathrm{d}s}. \tag{5.13}$$

The solution of the Fourier transformed function takes the form

$$\widetilde{R}(k_0,t) = \widetilde{R}(k_0,0)\exp\left[ik_0 y_{\text{eq}}(\mathrm{e}^{t/\tau_y} - 1) - \frac{D_y\tau_y}{2}k_0^2(\mathrm{e}^{2t/\tau_y} - 1)\right]. \tag{5.14}$$

Upon retransformation, the analytic solution $R(y,t)$ is given by

$$R(y,t) = \frac{1}{\sqrt{2\pi\sigma_y^2}}\exp\left(-\frac{(y - \langle y\rangle)^2}{2\sigma_y^2}\right). \tag{5.15}$$

This analytical form corresponds to a Gaussian distribution. The first moment of this Gaussian distribution, representing the mean value $\langle y(t)\rangle$, is provided by [16]

$$\langle y(t)\rangle = y_{\text{eq}}\left[1 - \exp\left(-t/\tau_y\right)\right] \pm y_{\max}\exp\left(-t/\tau_y\right). \tag{5.16}$$

The second moment, corresponding to the width $\sigma^2(t)$, is determined by

$$\sigma^2(t) = D_y \tau_y [1 - \exp(-t/2\tau_y)]. \tag{5.17}$$

The non-equilibrium characteristics of this initial condition are clearly observed in the temporal evolution of its first and second moments, wherein only in the limit of $t \to \infty$ do the exponential functions vanish and y approaches y_{eq}. The scenario of $y_{\max} \to y_{\mathrm{eq}}$ corresponds to nearly equilibrium initial conditions:

$$R(y, 0) = \delta\left(y - y_{\mathrm{eq}}\right), \tag{5.18}$$

as in this case, the first moment becomes independent of time.

With the analytical solution of the linear Fokker-Planck equation established, the subsequent section will provide a comprehensive review of the Relativistic Diffusion model.

5.3. The Relativistic Diffusion model

After deriving the solution for the linear Fokker-Planck equation using the relaxation time ansatz, we proceed to review the Relativistic Diffusion model, which was initially introduced in [13].

The equilibrium distribution is assumed to be the Boltzmann distribution due to the high energies [99] and is given by

$$E\frac{\mathrm{d}^3 N}{\mathrm{d}p^3} \propto E \exp(-E/T) = m_\perp \cosh(y) \exp(-m_\perp \cosh(y)/T), \tag{5.19}$$

where equation (2.24) has been employed. Consequently, the longitudinal production can be expressed as follows

$$E\frac{\mathrm{d}N}{\mathrm{d}y}(y, t) = c \int_m^\infty m_\perp^2 \cosh(y) R(y, t)\ \mathrm{d}m_\perp, \tag{5.20}$$

where m denotes typically the proton mass and $R(y, t)$ represents the statistical distribution function. The underlying assumption of this model is that the production yield can be described as the incoherent superposition of three distinct sources [16], which can be formulated as follows

$$\frac{\mathrm{d}N^{\mathrm{ch}}}{\mathrm{d}y}(\tau_{\mathrm{int}}) = N_{\mathrm{ch}}^1 R_1\left(y, \tau_{\mathrm{int}}\right) + N_{\mathrm{ch}}^2 R_2\left(y, \tau_{\mathrm{int}}\right) + N_{\mathrm{ch}}^{gg} R_{gg}\left(y, \tau_{\mathrm{int}}\right), \tag{5.21}$$

where $N_{\mathrm{ch}}^{1,2}$ correspond to the produced charged hadrons in the fragmentation sources, while N_{ch}^{gg} accounts for charged-hadron production in the mid-rapidity source.

The temporal parameter is set to the interaction time $t = \tau_{\text{int}}$, as the model assumes interactions between $t = 0$ and $t = \tau_{\text{int}}$ due to the nature of the underlying microscopic interactions.

This model can be applied to investigate charged-hadron production in relativistic heavy-ion collisions. However, evaluating this model presents several challenges.

Owing to the nature of QCD interactions, an energy scale $\Lambda_{\text{QCD}} \approx 200\,\text{MeV}$ exists, indicating a phase transition from quark-gluon interaction to hadron production. This naturally defines a time scale $\tau_{\text{int}} = 6 - 8$ fm/c [16], during which interactions between constituents cease and asymptotic states, namely the hadrons, are produced. Only in the limit $\tau_{\text{int}} \to \infty$ can the system reach global equilibrium. Nevertheless, determining the distinct time scales τ_{int} and τ_y directly in relativistic heavy-ion collisions poses a challenge. Previous investigations have shown that the entire system collectively expands in longitudinal and transverse direction [103].

When applying this model to asymmetric collisions, it becomes necessary to formulate the mean value of the equilibrium rapidity, denoted as y_{eq} and calculated as defined in [16]

$$y_{\text{eq}}(b) = -\frac{1}{2}\ln\frac{\left\langle m_T^{(1)}(b)\right\rangle \exp(y_{\max}) + \left\langle m_T^{(2)}(b)\right\rangle \exp(-y_{\max})}{\left\langle m_T^{(2)}(b)\right\rangle \exp(y_{\max}) + \left\langle m_T^{(1)}(b)\right\rangle \exp(-y_{\max})}. \tag{5.22}$$

This equation is associated with equation (2.19) where $y_{\max}$ corresponds to y_{beam} and $\left\langle m_T^{1,2}(b)\right\rangle$ represents the average centrality-dependent transverse mass. The latter is defined, as in equation (2.23), as

$$\left\langle m_T^{1,2}(b)\right\rangle = \sqrt{m_{1,2}^2(b) + \langle p_T\rangle^2}, \tag{5.23}$$

where $\langle p_T\rangle$ stands for the average transverse momentum and $m_{1,2}^2(b) = m_p N_{\text{part}}^{1,2}$ involves the participant mass. When $y_{\max}$ is large, the last equation simplifies to

$$y_{\text{eq}}(b) = \frac{1}{2}\ln\frac{\left\langle m_T^{(2)}(b)\right\rangle}{\left\langle m_T^{(1)}(b)\right\rangle}. \tag{5.24}$$

Following the introduction of the Relativistic Diffusion model, the subsequent chapter will involve the application of this model. We will employ initial conditions derived from microscopic quark-gluon interactions for the fragmentation source, as well as for the mid-rapidity source obtained from gluon-gluon interactions. These conditions will be applied to different collision scenarios, where we compute the corresponding pseudorapidity distributions.

6. Results for charged-hadron production

In this chapter, we introduce a novel model designed to elucidate the pseudorapidity distributions of produced charged hadrons in primarily asymmetric relativistic heavy-ion collisions. The foundation of our model is the well-established Relativistic Diffusion model (RDM), as detailed in section 5.3.

We embark on an exhaustive investigation centered on central p-Pb collisions. We explore two distinct models for the unintegrated gluon distribution, examine the distributions stemming from the diffusion process at intermediate times, and show the transverse momentum dependency of charged-hadron production distribution for various pseudorapidity values.

Our exploration commences with an analysis of pseudorapidity distributions for symmetric Pb-Pb collisions at LHC energies of $\sqrt{s_{NN}} = 5.02\,\text{TeV}$ across varying centrality classes. This investigation showcases the model's capability to explain symmetric collisions. Moreover, this experimental dataset has been available for a considerable period and provides data in a broader range in pseudorapidity space at LHC energies, encompassing pseudorapidity values up to $\eta = 5$, whereas similar datasets for asymmetric collisions only extend up to $\eta = 2$.

Subsequently, we present computed pseudorapidity distributions for minimum bias collisions at three incident energies and compare them with experimental data. This comparison allows us to observe the transition of the pseudorapidity distributions from RHIC energies to LHC energies. Specifically, we compare the pseudorapidity distributions for d-Au collisions at $\sqrt{s_{NN}} = 200\,\text{GeV}$ with Phobos data and with those at LHC energies of $\sqrt{s_{NN}} = 5.02\,\text{TeV}$ and $8.18\,\text{TeV}$ for p-Pb collisions. The experimental data used for comparison at LHC energies were obtained through measurements conducted by the CMS experiment.

6.1. The central p-Pb collision at $\sqrt{s_{NN}} = 5\,\text{TeV}$

The presented model builds upon the Relativistic Diffusion model, see section 5.3, which delineates the production of charged hadrons through three underlying

sources: the mid-rapidity source and two fragmentation sources. The latter undergoes an additional drift-diffusion process, commonly abbreviated as diffusion.

It is justified by a macroscopic equilibration process that facilitates the time evolution of distributions from τ_h to τ_{int}, with τ_y delineating its temporal scale. In this context, the time scale τ_h signifies the abstract time associated with factorization, while τ_{int} pertains to the instance when the hadrons are in free motion as the final state, also termed freeze-out time.

This foundational structure remains integral to our extended model, which characterizes the pseudorapidity distribution of charged-hadron production as expressed by

$$\frac{\mathrm{d}N_{\mathrm{ch}}}{\mathrm{d}\eta} = \frac{\mathrm{d}N_{\mathrm{ch}}^{gg}(\eta)}{\mathrm{d}\eta} + \frac{\mathrm{d}N_{\mathrm{pro}}^{qg}(\eta, \tau_{\mathrm{int}}/\tau_y)}{\mathrm{d}\eta} + \frac{\mathrm{d}N_{\mathrm{tar}}^{qg}(\eta, \tau_{\mathrm{int}}/\tau_y)}{\mathrm{d}\eta}, \tag{6.1}$$

where the pseudorapidity η is defined as in equation (2.21). N_{ch}^{gg} characterizes the yield of produced charged hadrons originating from the mid-rapidity source and is determined through the k_T-factorization approach based on small-x gluon-gluon interactions.

N_{pro}^{qg} and N_{tar}^{qg} denote the yields of produced charged hadrons resulting from hybrid-factorization, based on quark-gluon interactions, and involving an additional diffusion process towards smaller rapidity. The pertinent variables will be defined subsequently.

The yield of produced charged hadrons per pseudorapidity interval from the mid-rapidity source can be expressed as

$$\frac{\mathrm{d}N_{\mathrm{ch}}^{gg}(\eta)}{\mathrm{d}\eta} = \sum_h \int_0^{p_{\max}} 2\pi p_T \mathrm{d}p_T \; J_h(\eta, p_T) \frac{\mathrm{d}^2 N_h^{gg}(y(\eta), p_T)}{\mathrm{d}y \mathrm{d}p_T}, \tag{6.2}$$

where we have incorporated the two-dimensional transverse momentum by

$$\mathrm{d}\boldsymbol{p}_T^2 = 2\pi p_T \mathrm{d}p_T. \tag{6.3}$$

The yield of produced charged hadrons, $\mathrm{d}^2 N_h^{gg}/\mathrm{d}y\mathrm{d}p_T$, is defined according to equation (4.7), where a summation is performed over the charged hadron species, including $h = \pi^{\pm}, K^{\pm}, p^{\pm}$. Importantly, in the sense of this equation these species differ only in the mass of the produced hadron. A factor of 2 is applied to account for particle and anti-particle contributions.

It is also worth noting that the principle of parton-hadron duality is employed to establish a connection between the produced gluons and the corresponding measurable hadrons.

By using equation (4.6), we can define the limit of the transverse momentum by

$$p_{\max}^2 = \sqrt{s_{NN}} e^{-2|y|} - m^2, \tag{6.4}$$

following from $x_{\max} = 1$, where $|y|$ accounts for the definition of the projectile, either A or B.

The theoretical model is computed in the rapidity frame of reference defined in the nucleon-nucleon center of mass, denoted as y_{NN}. When comparing these calculations to experimental data, a series of transformations are required, including the conversion from y_{NN} to the laboratory frame rapidity y_{lab}, and subsequently to the pseudorapidity η. The corresponding Jacobian, denoted as $J_h(\eta, p_T)$, is defined in equation (2.28). It should be noted that the Jacobian is uniquely defined for each individual hadron species.

We have incorporated the running coupling, which are parametrized as shown in equation (3.47), into the factorization schemes by substituting α_s with $\alpha_s(Q^2)$, with the energy scale specified in the corresponding sections.

Furthermore, the microscopic contribution attributed to the mid-rapidity source will not undergo any supplementary macroscopic diffusion process.

In the case of asymmetric collisions, it becomes necessary to differentiate between the two individual fragmentation sources. Each source i is calculated independently. The yield per pseudorapidity interval for an individual fragmentation source N_i^{qg} is defined as follows

$$\frac{\mathrm{d}N_i^{qg}(\eta, \tau_{\mathrm{int}}^i/\tau_y^i)}{\mathrm{d}\eta} = \widetilde{J}\left(\frac{\langle p_T \rangle}{m_\pi c}\right) \frac{\mathrm{d}N_i^{qg}(y \equiv \eta, \tau_{\mathrm{int}}^i/\tau_y^i)}{\mathrm{d}y}, \tag{6.5}$$

Here, $\tau_{\mathrm{int}}^i/\tau_y^i$ represents the evolution in the diffusion process from the theoretical timescale after hybrid-factorization has taken place to the moment at which hadronisation is completed and the hadrons are moving freely.

Similarly to the mid-rapidity source, we also need to perform transformations from y_{NN} to y_{lab} and then to η. However, due to the one-dimensional nature of the diffusion along the beam direction, which results in the loss of the precise transverse momentum distribution, the exact transformation cannot be employed. Consequently, we rely on the effective Jacobian as defined in equation (2.29), coupled with the approximation of $y \approx \eta$.

Our calculations for charged hadrons stemming from the fragmentation sources exclusively involve pions. This approximation is justifiable owing to the relatively lower mass of pions in comparison to kaons and protons, along with the suppression effects introduced by the fragmentation functions.

The initial yield per rapidity interval for an individual fragmentation source based on hybrid factorization, at the abstract time τ_h, is expressed as follows

$$\frac{\mathrm{d}N_i^{qg}}{\mathrm{d}y}(y, \tau_h) = \int_0^{p_{\max}} 2\pi p_T \mathrm{d}p_T \, \frac{\mathrm{d}^2 N_\pi^{qg}}{\mathrm{d}y \mathrm{d}p_T}(y, p_T). \tag{6.6}$$

The $\mathrm{d}^2 N_\pi^{qg}/\mathrm{d}y\mathrm{d}p_T$ originates from quark-gluon interactions within hybrid factorization and is defined by equation (4.22). This initial distribution is subsequently applied to the relativistic diffusion process, governed by a Fokker-Planck equation. The definition of the diffusion process is provided by equation (5.8).

The final yield resulting from the evolution of the diffusion process until τ_{int} characterizes the production of charged hadrons from the underlying fragmentation source.

The hybrid factorization employs quark parton distribution functions. We utilize the up-valence quark distribution derived from the MSTW2008 [33] parametriza-

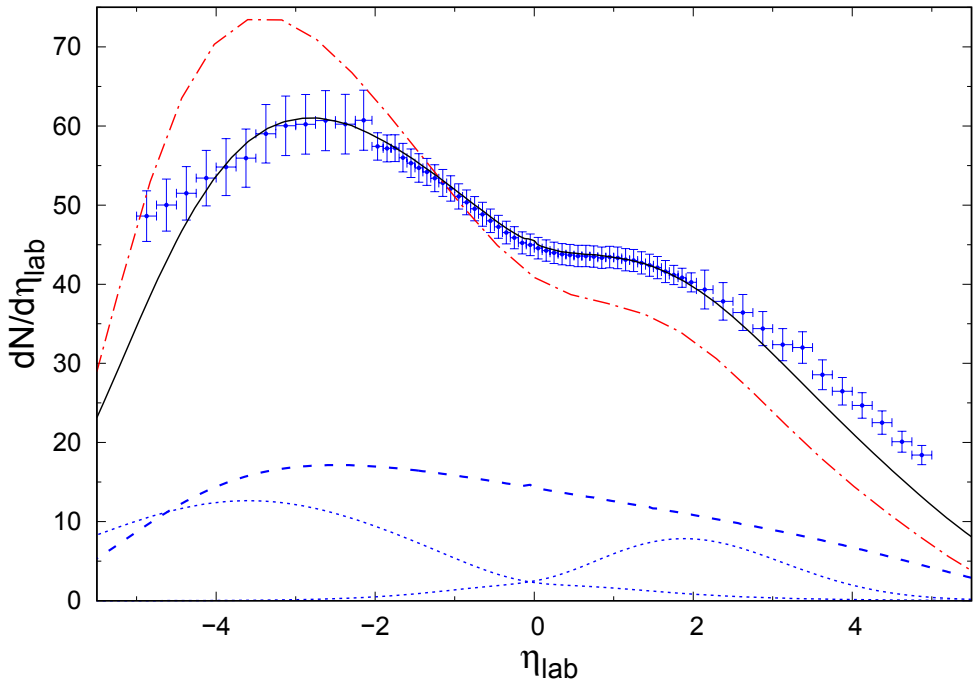

Figure 6.1.: Calculated pseudorapidity distributions of produced charged hadrons for p-Pb collisions at $\sqrt{s_{NN}} = 5.02\,\mathrm{TeV}$ for the central collisions (0-5%). The data for $|\eta| < 2.0$ come from the ALICE detector [104], whereas the data for $|\eta| > 2.0$ come from [105].
The solid distribution shows the full-calculated pseudorapidity distribution based on the unintegrated gluon distributions with KLN model, whereas only the dot-dashed distribution shows the unintegrated gluon distributions with GBW model. The further distributions are calculated with the KLN model. The dashed distribution shows only pions produced by gluon-gluon interactions and the dotted distributions show the produced pions coming from quark-gluon interactions.

tion. This parametrization is presented as a numerical library, establishing the initial conditions and further evolving them to the relevant energy scale through an extrapolation of the DGLAP equation.

As for the fragmentation functions, we implement the AKK parametrization [106] ourselves. It takes the following form

$$D_i^{h^\pm}(z, M_0^2) = N_i^{h^\pm} z^{a_i^{h^\pm}} (1-z)^{b_i^{h^\pm}} \left(1 + c_i^{h^\pm}(1-z)^{d_i^{h^\pm}}\right) \tag{6.7}$$

where $M_0 = \sqrt{2}\mathrm{GeV/c^2}$ and the parameters N, a, b, c, d are involved. These parameters relate to the transition from the underlying partons to the produced hadrons and are provided separately for each hadron species in [106]. This parametrization assumes symmetrical production of both hadrons and antihadrons. For our calculations, we solely employ the fragmentation function for pions $\pi^\pm$. In principle, the fragmentation functions should also be evolved to match the energy scale of the system using the DGLAP equation. However, in this specific calculation, the energy scale of the fragmentation function is held constant at M_0^2.

The parameters governing the fragmentation function for the production of a pion from an up-quark are as follows: $N = 0.32$, $a = -2.07$, $b = 0.96$, $c = -0.81$, and $d = 2.91$ [106]. In contrast to the AKK parametrization, alternative approaches to parametrize the fragmentation functions have been proposed [90].

The unintegrated gluon distributions for both factorization schemes are characterized by the model values $\lambda = 0.288$ and $x_0 = 1$. While the value of Q_0 is set separately for each calculation, it remains constant within each calculation for both factorization schemes.

Figure 6.1 presents the calculated pseudorapidity distributions of produced charged hadrons for central p-Pb collisions at $\sqrt{s_{NN}} = 5.02\,\mathrm{TeV}$. Detailed values of the model parameters will be provided in the subsequent chapter, specifically in table 7.6. The solid curve in the figure corresponds to the calculation based on the KLN model, demonstrating good agreement with the experimental data.

The distribution shown as dot-dashed curves illustrates the calculated results using the unintegrated gluon distributions by the GBW model. This specific model employs an identical set of parameters, thereby indicating that its alignment with the data will be comparatively less precise compared to the KLN model calculation.

Despite this, the depiction of the overall maxima, particularly in the backward region tends to overestimate the observed charged-hadron production to a significant extent. This discrepancy might originate from the inherent simplicity of the model in conjunction with its leading-order BFKL rapidity evolution, which may not adequately capture the behaviour at higher rapidities.

Figure 6.2 depicts the calculated diffusion process for the pseudorapidity distributions originating from both fragmentation sources, which was used in the same

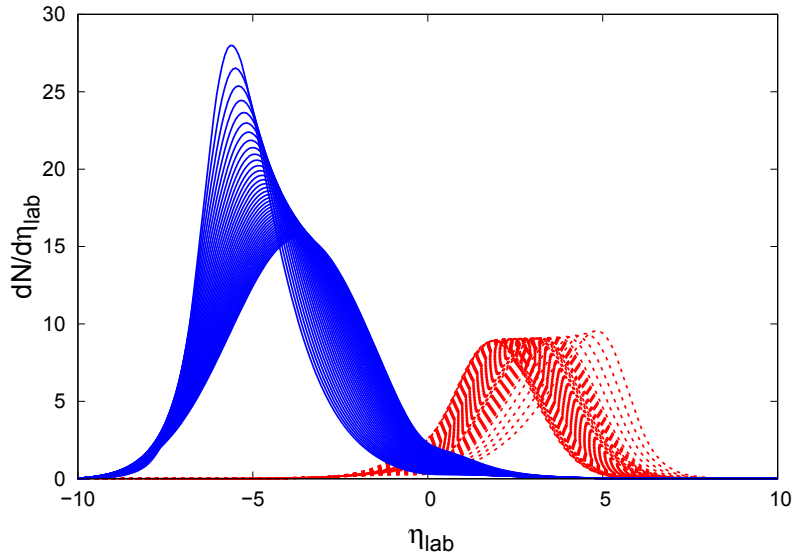

Figure 6.2.: Calculated diffusion process for pseudorapidity distributions of the fragmentation sources. The initial distributions, indicated by its peak position being the largest rapidity, is calculated within the hybrid-factorization scheme, whereas the final distribution shows the distribution associated to produced charged hadrons.

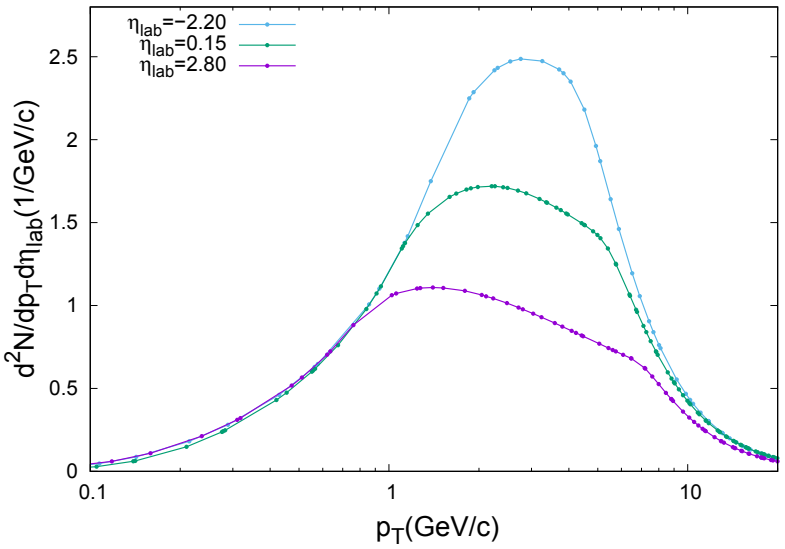

Figure 6.3.: Calculated transverse momentum distributions of produced charged hadrons for p-Pb collisions at $\sqrt{s_{NN}} = 5.02$ TeV for the central collisions (0-5%). The distributions are shown for three pseudorapidity values.

calculation underlying figure 6.1. The figure visually demonstrates that each peak experiences a shift towards the equilibrium rapidity y_{eq}, which is situated close to mid-pseudorapidity. Concurrently, the distributions undergo a diffusion that leads to an enlargement of their widths. This depiction corresponds to the time interval spanning from τ_h to τ_{int}. It is important to note that this model does not encompass the treatment of the initial distribution prior to the collision or the equilibrium distribution.

In contrast to the macroscopic diffusion process, figure 6.3 presents the computed transverse momentum distributions for three distinct pseudorapidity values of the same calculation shown in figure 6.1.

On the numerics

In the course of this thesis, we developed a C++ program starting from scratch, aimed at addressing the intricate non-analytical integrals and resolving the differential equation. This endeavour demanded substantial effort and a significant time investment to arrive at the present state of the code, which we have now achieved.

For the computation of the momentum integrals, we employed the *QAG adaptive integration with 61 point Gauss-Kronrod rules* method sourced from the GSL Numerical library [107, 108].

To solve the Fokker-Planck equation, we employed a finite-element method, which was implemented by [109, 110].

Based on these two library implementation a new problem occurred, the different implementations of their underlying grids on which the integrals and the differential equations are solved.

To tackle this issue and refine the corresponding grids we needed to add an interpolation method to transform between the different algorithms.

Therefore, we also included the *spline* library from the GSL Numerical library , in particular we use the *Non-rounded Akima spline with natural boundary conditions* to refine the grids.

Finally, we also included the *ROOT* library [111] into our codebase to perform χ^2-minimization.

6.2. Symmetric collisions at $\sqrt{s_{NN}} = 5\,\mathrm{TeV}$

In this section, we present our computations of centrality-dependent pseudorapidity distributions for the production of charged hadrons in Pb-Pb collisions at LHC energies.

While the primary emphasis of this investigation revolves around asymmetric collisions, the consideration of symmetric collisions provides a pivotal limit that aids in validating our calculations. More specifically, our calculations encompass distinct forward and backward rapidity regions. Under the conditions of symmetric collisions, these two rapidity domains must coincide, when they are mirrored.

For symmetric systems the differentiation between the laboratory and center of mass frame of reference becomes dispensable. Furthermore, the mass numbers A_1 and A_2 are identical, likewise the numbers of participants $N^{(1)}_{\mathrm{part}}$ and $N^{(2)}_{\mathrm{part}}$.

For our analysis, we have opted to utilize experimental data obtained by the ALICE collaboration at $\sqrt{s_{NN}} = 5.023\,\mathrm{TeV}$ [112]. The experimental setup for this measurement involved a proton beam momentum of $p_{\mathrm{beam}} = 4\,\mathrm{TeV}/c$. When applied to the corresponding lead beam, this translates to a beam momentum of $p_{\mathrm{beam}} = 1.577\,\mathrm{TeV}/c$, as mentioned in equation (2.4).

Using equation (2.14), we can calculate the beam rapidity, yielding $y_{\mathrm{beam}} = 8.586$. Subsequently, equation (2.20) enables us to precisely determine the value of $\sqrt{s_{NN}}$, a quantity conventionally used to classify sets of experimental data in the realm of relativistic heavy-ion collisions. However, it is essential to understand the methodology behind calculating the exact value of $\sqrt{s_{NN}}$, particularly in the context of asymmetric collisions.

Our computations of the pseudorapidity distributions utilize the extended Relativistic Diffusion model. In this approach, the mid-rapidity source is determined through gluon-gluon interactions employing k_T-factorization, while the two fragmentation sources stem from quark-gluon interactions and hybrid-factorization.

We also incorporate an additional diffusion process, as introduced in equation (5.8), that evolves from the time corresponding to baryon stopping to the time corresponding to charged-hadron production. This entire process is scaled by the number of participants N_{part} to account for multiple nucleon-nucleon interactions. Comprehensive details of these calculations are available in chapter 6.

The geometric parameters required for these calculations are provided by experimental collaborations and will be subsequently presented. The data sources for these parameters are the same as those used for the experimental data.

For the gluon saturation scale Q_s^2, see equation (3.26), we adopt commonly used values, such as $\lambda = 0.288$ as reported in [66], for the gluon saturation scale exponent. However, the initial saturation momentum Q_0^2 linked to the unintegrated

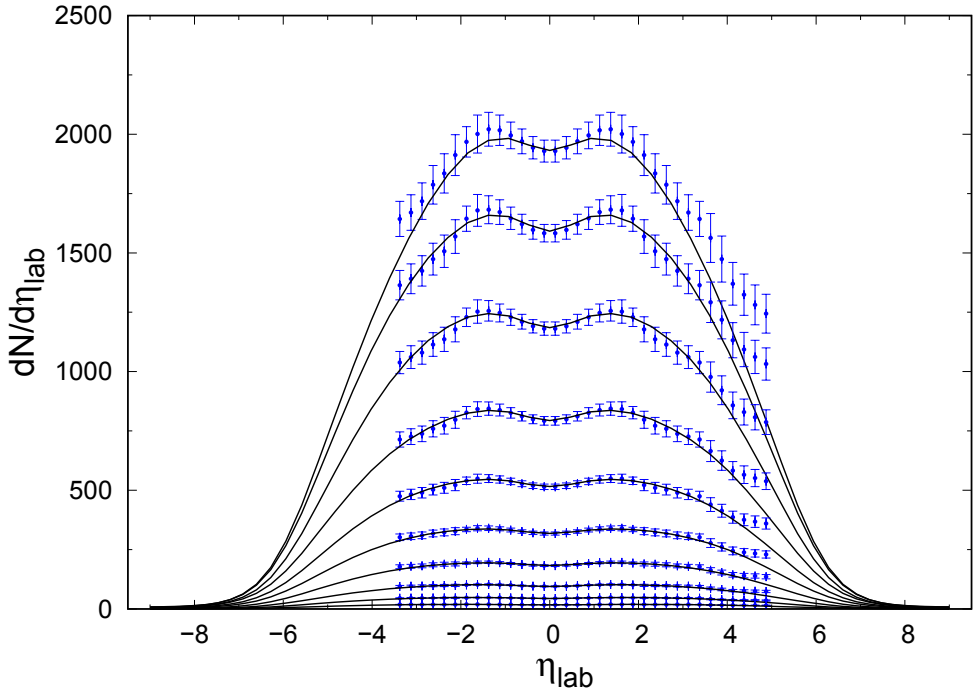

Figure 6.4.: Calculated pseudorapidity distributions of produced charged hadrons for Pb-Pb collisions at $\sqrt{s_{NN}} = 5.02\,\mathrm{TeV}$ compared with data measured by ALICE for various centrality classes [112]. The solid curves represent the calculated distributions of produced charged hadrons using the extended Relativistic Diffusion model. The centrality classes are given from top to bottom as follows: 0-5%, 5-10%, 10-20%, 20-30%, 30-40%, 40-50%, 50-60%, 60-70%, 70-80%, 80-90%.

gluon distribution varies according to the centrality. We will delve into the specifics of this aspect in the subsequent discussions.

To delineate the pseudorapidity distributions originating from hybrid-factorization as fragmentation sources for charged-hadron production, we incorporate a diffusion process that evolves our rapidity distributions to τ_{int}, utilizing the time scale τ_y. These distributions exhibit significant deviations from the equilibrium distribution characterized by y_{eq}.

Subsequently, after evolving the distribution, we proceed with the transformation to pseudorapidity through equation (2.29), incorporating $\langle p_T \rangle$ values ranging from $0.5\,\mathrm{GeV/c}$ for central collisions to $0.3\,\mathrm{GeV/c}$ for ultra-peripheral collisions. It is of significance to emphasize that the transformation from rapidity to pseudorapidity for the gluon-gluon source is devoid of additional parameters. Consequently, the precise transformation outlined in equation (2.28) is directly utilized.

central.(%)	N_{ch}	N_{ch}^{gg}	N_{π}^{gg}	N_{K}^{gg}	N_{π}^{gg}	N_{Pb}^{qg}	R_{qg}^{gg}
0-5	17923	13857	4859	4670	4329	2033	3.4
5-10	15109	11675	4101	3935	3639	1717	3.4
10-20	11505	8848	3113	2983	2752	1329	3.3
20-30	7873	6058	2135	2043	1880	908	3.3
30-40	5218	3989	1409	1346	1233	615	3.2
40-50	3287	2505	887	845	772	391	3.2
50-60	1907	1440	512	487	442	234	3.1
60-70	1009	757	270	256	231	126	3.0
70-80	485	360	129	122	109	63	2.9
80-90	198	145	52	49	43	27	2.7

Table 6.1.: Calculated produced charged hadrons N_{ch} for Pb-Pb collisions at $\sqrt{s_{NN}} = 5.02\,\mathrm{TeV}$ for various centrality classes. The calculations integrate over the full range of pseudorapidity. The extended Relativistic Diffusion model comprises three individual production sources: the mid-rapidity source N_{ch}^{gg} and two identical fragmentation sources N_{Pb}^{qg}. The produced charged hadrons for the mid-rapidity include pions N_{π}^{gg}, kaons N_{K}^{gg}, and protons N_{p}^{gg}, whereas the fragmentation regions only contain pions. The ratio between the mid-rapidity region and the combined fragmentation regions is shown by $R_{gg}^{qg} = N_{\mathrm{ch}}^{gg}/\Sigma_i N_i^{qg}$.

Figure 6.4 presents the computed centrality dependence for diverse centrality classes. The sub-distributions have not been visually represented.

Table 6.1 presents the overall amount of produced hadrons computed using the extended Relativistic Diffusion model. This tally encompasses pions, kaons, and protons stemming from the mid-rapidity source, and exclusively pions for the fragmentation sources., which is justified as first approximation by the suppression of heavier particles within the fragmentation functions. The majority of hadron production occurs within the gluon-gluon mid-rapidity source. The classification of centrality classes is determined by the ALICE collaboration and is detailed in table 6.2.

The amount of produced hadrons demonstrates a steady increase, with approximately ~ 100 times more hadrons produced in central collisions compared to ultra-peripheral collisions.

Upon examining the ratio between the mid-rapidity source and the combined fragmentation sources, denoted as $R_{qg}^{gg} = N_{\mathrm{ch}}^{gg}/(N^{qg} + N^{qg})$, we discern a similar mono-

tonic trend. Interestingly, this ratio also follows a relatively straightforward relationship, expressed as

$$R_{qg}^{gg} \sim \frac{A^{2/3} N_{\text{part}}}{2A^{1/3} N_{\text{part}}} = \frac{A^{1/3}}{2} \approx 3, \tag{6.8}$$

where the mass number is $A_{Pb} = 208$. The number of participants N_{part} are shown in table 6.2. This phenomenon can be rationalized by considering the k_T-factorization.

This scaling is proportional to $A^{1/3}$ for each implicated Q_s, and further scales with N_{part} to quantify how many of such processes taking place. Conversely, the denominator, which encompasses the hybrid-factorization, entails the summation of the two fragmentation sources, see equation (6.1). Each of these sources scales by the product of Q_s and the number of N_{part} processes.

Analysing the specific ratio, the production resulting from gluon-gluon interactions relative to quark-gluon interactions decreases as one moves from central collisions to ultra-peripheral collisions. This observation offers an initial glimpse into the trends that will manifest more prominently in the context of asymmetric collisions, which will be further explored in subsequent discussions.

The observed mass dependence depicted in table 6.1 deviates from the anticipated mass distribution, which is approximately composed of 83% pions, 13% kaons, and

centrality (%)	N_{part}^{Pb}	Q_0^2 (GeV$^2/c^2$)	$D\tau_y$	τ_{int}/τ_y	χ^2/N_{dof}
0-5	190.00	0.013	3.0	1.00	1.756
5-10	166.50	0.012	4.0	1.00	1.269
10-20	131.50	0.012	4.0	0.90	1.084
20-30	94.00	0.011	6.0	0.90	0.833
30-40	65.50	0.011	6.0	0.80	0.726
40-50	43.15	0.010	7.0	0.70	0.638
50-60	26.80	0.009	7.0	0.70	0.802
60-70	15.20	0.009	7.0	0.70	0.918
70-80	7.80	0.008	7.0	0.60	0.803
80-90	3.65	0.007	8.0	0.50	0.948

Table 6.2.: Model parameters extracted from the Relativistic Diffusion model used to compute pseudorapidity distributions for Pb-Pb collisions at $\sqrt{s_{NN}} = 5.02\,\text{TeV}$. The number of participants N_{part} were sourced from [112]. The parameters τ_{int}/τ_y and $D\tau_y$ are dimensionless.

4% protons, as shown in [113, 114] for similar collision configurations. Utilizing the transverse mass m_T instead of the transverse momentum p_T in the factorization scheme is not enough to predict the mass dependency. A more refined model for the parton-hadron transition needs to be considered to describe the mass distribution more accurately.

Table 6.2 shows the model parameter from the extended Relativistic Diffusion model. The number of participants N_{part} are obtained from the ALICE collaboration, where they calculated these with the Glauber Monte Carlo simulations. In symmetric collisions participants for projectile and target are treated the same, which leads to $N_{\mathrm{part}} = \langle N_{\mathrm{part}} \rangle /2$.

The computation for central collisions involves the utilization of specific parameters for the diffusion coefficient D and interaction time τ_{int}. These values are determined through fitting to experimental data, whereas τ_y is expressed in multiples of fm/c.

In a broader context, a more accurate estimation could be achieved by employing an alternative diffusion process that takes into account the initial parton distributions of the particles before the collision, which could then be compared with the measured total collision time.

Albeit, our model description only allows for the interpretation of the centrality dependence of these values.

Considering ultra-peripheral collision, the interaction time diminishes, resulting in a reduced level of equilibration compared to central collisions. This phenomenon can be attributed to the lower number of participating particles in such collisions, causing them to exit the interaction region more rapidly. Consequently, the likelihood of further scattering events decreases.

Moreover, as collisions become more peripheral, the diffusion coefficient experiences an increase. This observation suggests that, in the event of a collision, described by the diffusion process, the produced hadrons undergo a greater momentum loss in the beam direction.

The corresponding unintegrated gluon distribution is only applicable within the small-x limit. However, when calculating the distributions of produced hadrons, integration over a combination of x_1 and x_2 is involved, which is determined by the collision kinematics. Generally, this lies outside the small-x limit. To address this challenge in the large pseudorapidity regime, two potential approaches are considered.

In our initial implementations, we addressed these effects by introducing an effective parameter x_{cut} to manage the regime where the approximation of gluon saturation is not applicable. A more refined approach involves incorporating a suppression factor, specifically of the form $(1 - x)^4$, as detailed in section 3.3.

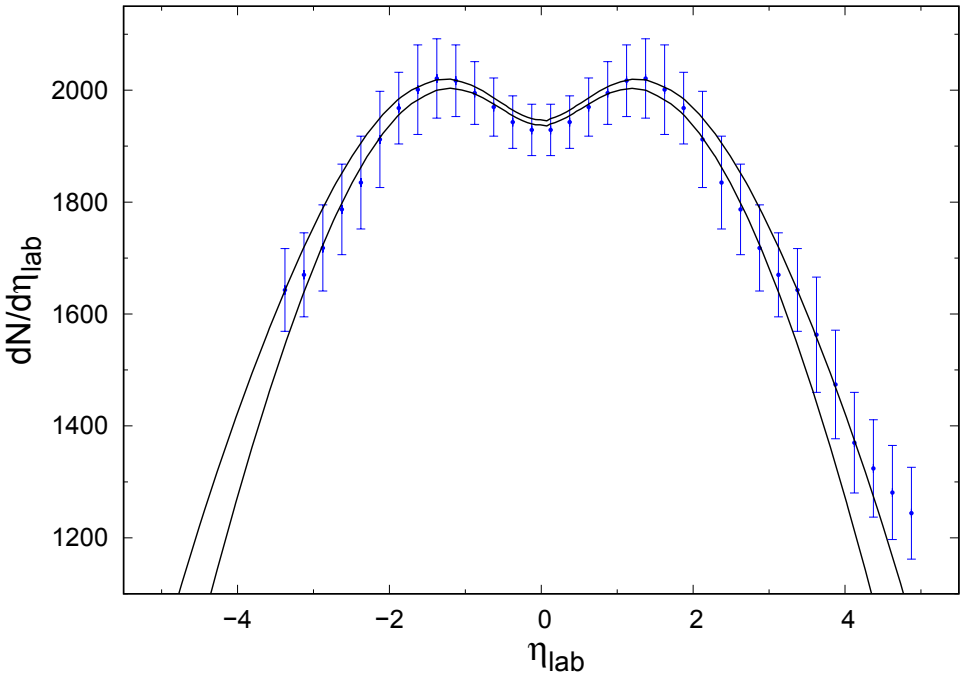

Figure 6.5.: Influence of the large-x suppression factors on pseudorapidity distributions of hadron production.Curves show: $f(x) = (1-x)^4$ (inside), $f(x) = (1-x)^2$ (outside).

However, when examining the region of large pseudorapidity near the beam rapidity, our model appears to underestimate the production of hadrons. To grasp the impact of this phenomenon, figure 6.5 illustrates the effect of the large-x suppression factor applied to the gluon distribution on the pseudorapidity distribution of charged-hadron production.

This is achieved by varying the exponent of the suppression factor. The graph showcases two curves: one where the exponent lies within the typical range, and another where a slightly different factor is utilized, namely $(1-x)^2$. This adjusted factor aligns the model's predictions with the experimental data more effectively.

In contrast, the large-x behaviour in the MSTW parametrization of the gluon distribution is characterized by the functional form of $(1-x)^{5.4}$ [33].

Having examined the symmetric realization of our model calculation, we now turn our attention to analysing asymmetric collisions.

6.3. Energy dependence: from RHIC to LHC

This section presents the calculations conducted for minimum bias collisions at three distinct energy levels: $\sqrt{s_{NN}} = 0.2, 5.02$, and $8.16\,\text{TeV}$. Figure 6.6 shows the calculated pseudorapidity distributions for these energies. They agree with the experimental data.

In table 6.3, the produced hadrons for the underlying gluon-gluon and fragmentation sources are tabulated. These values exhibit a monotonous trend with respect to energy, with the contributions of the gluon-gluon source becoming more prominent at higher energies. Notably, for LHC energies, the contributions of the projectile-like and target-like fragmentation sources are of comparable magnitudes.

Table 6.4 shows similar initial saturation scale values Q_0^2 for all three energy levels. This observation indicates that Q^2 not only scales with $A^{1/3}$ but also depends on centrality. Considering the diffusion parameter, it shows that for $\sqrt{s_{NN}} = 200\,\text{GeV}$ the hybrid factorization are very near to the time scale similar to the time scale of the charged-hadron production.

With increasing energy the diffusion coefficients of the target-like fragmentation source increases, as well as, the interaction time, which means the fragmentation sources thrive through the equilibrium. But also the overall model parameter for the LHC energies are very similar.

In region of the target heavy-ion, for low energies the fragmentation source is far-from-equilibrium, because it is near to the hadronisation phase. Consequently,

$\sqrt{s_{NN}}$	N_{ch}	N_{ch}^{gg}	N_{π}^{gg}	N_{K}^{gg}	N_{p}^{gg}	N_{tar}^{qg}	N_{pro}^{qg}	$R_{\text{pro}}^{\text{tar}}$	R_{qg}^{gg}
200 GeV	83.5	27.8	10.8	9.4	7.5	43.1	12.6	3.4	0.5
5.02 TeV	185.1	141.3	50.5	47.6	43.1	22.1	21.9	1.0	3.2
8.16 TeV	228.4	176.9	62.9	59.6	54.4	27.1	24.8	1.1	3.4

Table 6.3.: Calculated produced charged hadrons N_{ch} for minimum bias p-Pb and d-Au collisions at various energies. The extended Relativistic Diffusion model comprises three individual production sources: the mid-rapidity source N_{ch}^{gg} and two fragmentation sources $N_{\text{pro/tar}}^{qg}$. The produced charged hadrons for the mid-rapidity include pions N_{π}^{gg}, kaons N_{K}^{gg}, and protons N_{p}^{gg}, whereas the fragmentation regions only contain pions. The ratio between the two fragmentation sources are shown as $R_{pro}^{tar} = N_{tar}^{qg}/N_{\text{pro}}^{qg}$. The ratio $R_{gg}^{qg} = N_{\text{ch}}^{gg}/\Sigma_i N_i^{qg}$ represents the proportion of produced charged hadrons in the mid-rapidity region compared to the combined fragmentation regions.

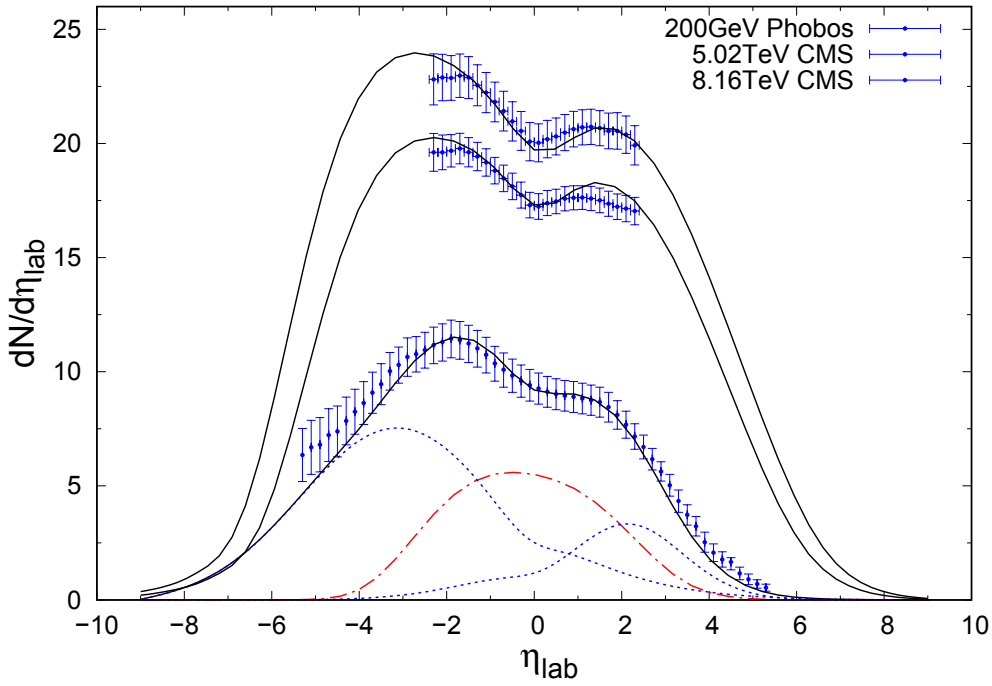

Figure 6.6.: Calculated pseudorapidity distributions of produced charged hadrons for p-Pb and d-Au collisions at different energies. Compared with data from Phobos [115] and CMS [116]. Pseudorapidity distributions at $\sqrt{s_{NN}} = 200\,\text{GeV}$, 5.02 TeV and 8.16 TeV (from bottom to top).

hadrons escape the interaction region at a faster rate. Additionally, hadrons sense a greater momentum loss in the beam direction with increasing energy, while maintaining consistency for LHC energies.

$\sqrt{s_{NN}}$	$N_{\text{part}}^{\text{tar}}$	Q_0^2 (GeV$^2/c^2$)	$D^{\text{pro}}\tau_y$	$\tau_{\text{int}}^{\text{pro}}/\tau_y$	$D^{\text{tar}}\tau_y$	$\tau_{\text{int}}^{\text{tar}}/\tau_y$	χ^2/N_{dof}
200 GeV	6.60	0.05	2.0	0.1	8.0	0.2	0.803
5.02 TeV	6.87	0.06	2.9	0.6	13.0	0.9	0.340
8.16 TeV	7.09	0.06	2.9	0.6	13.0	1.0	0.142

Table 6.4.: Model parameters extracted from the Relativistic Diffusion model used to compute pseudorapidity distributions for p-Pb and d-Au minimum bias collisions. The number of participants $N_{\text{part}}^{\text{tar}}$ were sourced from [117] and [116]. The parameters $\tau_{\text{int}}^i/\tau_y^i$ and $D^i\tau_y^i$ are dimensionless.

7. Centrality dependence of pseudorapidity distributions

In this chapter, we present our calculations of centrality-dependent pseudorapidity distributions and compare them with experimental data from Phobos and LHC. The extended Relativistic Diffusion model and its numerical implementation have been discussed in the previous chapter. Here, our primary focus lies in exploring the centrality dependence of our calculations.

We commence with an investigation of pseudorapidity distributions of asymmetric d-Au collisions at Phobos energies of $\sqrt{s_{NN}} = 200\,\mathrm{GeV}$, covering multiple centrality classes. Despite the lower energy in comparison to LHC collisions, the extensive coverage of the experimental data in pseudorapidity space near the beam rapidity provides significant value for comparison and analysis.

In the subsequent section, we examine the centrality dependence of our calculations and compare them with ATLAS data at $\sqrt{s_{NN}} = 5.02\,\mathrm{TeV}$. These data were the initial collection of data that served our purpose for analysing asymmetric collisions, encompassing a broader extent of pseudorapidity space. The selection of centrality classes for ultra-peripheral collisions exhibits implications compared to the centrality classes from ALICE.

In the following part of this section, we present the main results of our calculations for the pseudorapidity distributions for p-Pb collisions. These outcomes are compared with the recently published expanded data provided by the ALICE collaboration at $\sqrt{s_{NN}} = 5.02\,\mathrm{TeV}$. These data encompass a broader pseudorapidity range, extending up to $\eta = 5$. The improved data permits a more comprehensive analysis of ultra-peripheral collisions.

The subsequent section presents a comparison between our computational results for p-Pb collisions at $\sqrt{s_{NN}} = 8.16\,\mathrm{TeV}$ and the experimental data obtained from ALICE. This section also includes predictions for a wider pseudorapidity range, spanning from $\eta = 2$ to $\eta = 5$. The last part of the section concludes with a detailed examination of the minor variations in the initial saturation scale across all the calculated collisions, highlighting their centrality dependence.

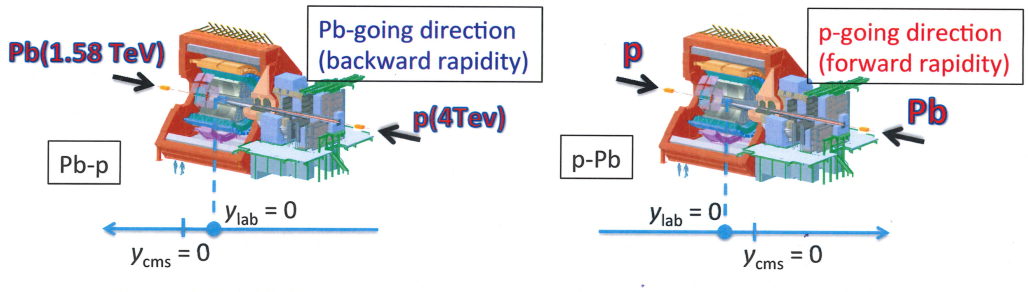

Figure 7.1.: Schematic demonstration of the ALICE detector and the two possible beam configurations of asymmetric heavy-ion collisions. The momenta are determined by the experimental setup. For p-Pb collisions at $\sqrt{s_{NN}} = 5.02\,\text{TeV}$, the momentum of the proton beam is fixed to 4 TeV, and the lead beam momentum is scaled by a factor of Z/A. Figure taken from Ploskon [118].

Before starting the discussion of our findings, it is essential to highlight a key aspect concerning asymmetric collisions. Illustrated in figure 7.1 is a schematic representation of the experimental arrangements and the two potential conventions for handling asymmetric collisions. Our preference aligns with the second convention, wherein forward rapidities are linked to the particle beam resembling the projectile, consisting of deuterons and protons. In parallel, backward rapidities correspond to the particle beam akin to the target, which in our instance comprises gold and lead nuclei.

7.1. Asymmetric d-Au collisions at $\sqrt{s_{NN}} = 200\,\mathrm{GeV}$

We provide an analysis of the centrality-dependent calculations of pseudorapidity distributions for produced charged hadrons in d-Au collisions at RHIC energies. Asymmetric collisions necessitate the separate calculation of forward and backward rapidities, unlike the simple mirroring employed in symmetric collisions.

The relevant experimental data have been reported in multiple papers. The minimum bias data were published in [115], while centrality-dependent data can be found in [119]. A review of Phobos data has also been published in [117].

This dataset, stemming from experiments conducted prior to LHC energies, covers pseudorapidity measurements up to nearly the beam rapidity. This extensive coverage allows for comprehensive testing of the full shape of the distribution. However, it is important to note that the deuteron is significantly more complex than a simple combination of a proton and a neutron.

In d-Au collisions, the beam momenta are set such that the energy per nucleon-nucleon pair is given by $\sqrt{s_{NN}} = 200\,\mathrm{GeV}$, corresponding to $y_{\mathrm{beam}} = 5.362$. The shift in rapidity between the laboratory frame and the nucleon-nucleon pair reference frame is $\Delta y = 0.110$, which needs to be considered when comparing the calculated rapidity distributions with data.

The experimental data adhere to the same convention as that employed in this thesis, where positive rapidity is attributed to the deuteron beam. The geometric parameters required for these calculations are established by experimental collaborations and will be subsequently presented. The data sources for these parameters are the same as those used for the experimental data.

We performed computations of the pseudorapidity distributions using the extended Relativistic Diffusion model as outlined in section 6.1.

For the gluon saturation scale exponent we use $\lambda = 0.288$ and $x_0 = 1$. The initial saturation momentum Q_0^2, linked to the unintegrated gluon distribution, also exhibits a minor dependence on centrality.

To account for the fragmentation sources, we introduce a diffusion process that evolves our rapidity distributions towards τ_{int}, using the time scale τ_y. However, the specific value of the time scale based on τ_y remains elusive within our model. These distributions significantly deviate from the equilibrium distribution characterized by y_{eq}. For the Jacobian of the fragmentation sources, we employ $\langle p_T \rangle$ values between $0.4\,\mathrm{GeV}/c$ and $0.5\,\mathrm{GeV}/c$, along with the pion mass m_π.

In figure 7.2, the computed centrality dependence for various centrality classes is depicted. The outcomes derived from our analysis reveal a notable alignment between the computed results and the experimental data, spanning a wide range of pseudorapidity values. Specifically, the model adeptly captures the behaviour

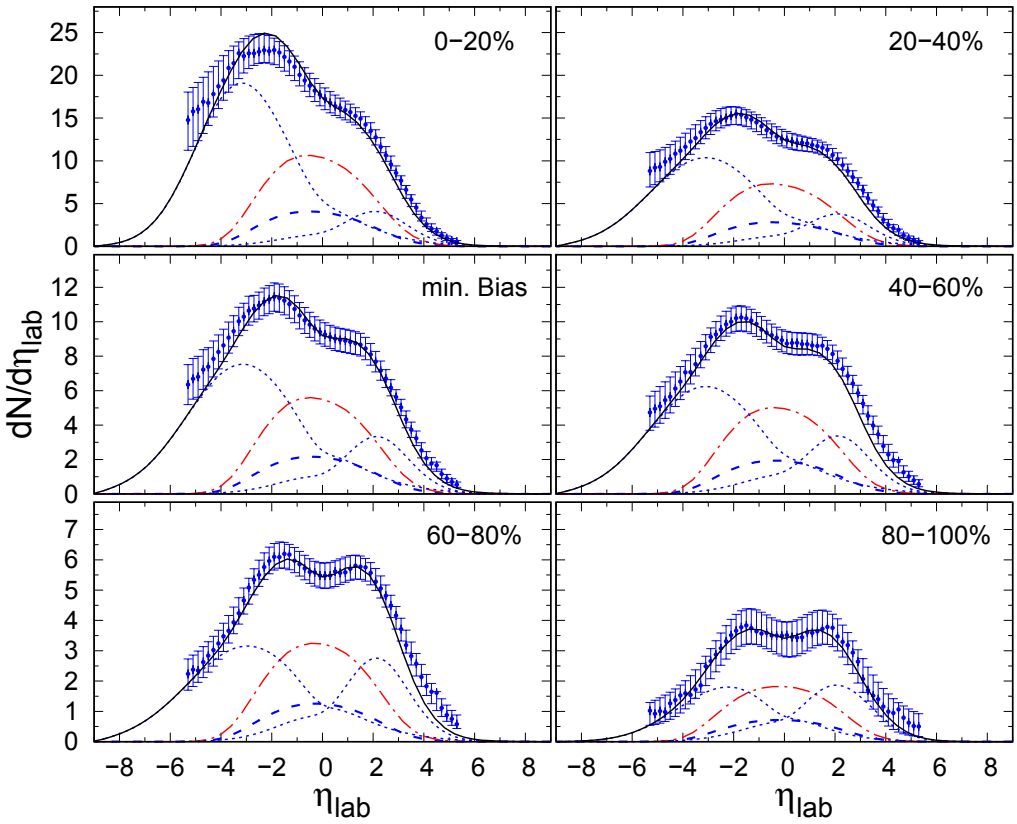

Figure 7.2.: Calculated pseudorapidity distributions of produced charged hadrons for d-Au collisions at $\sqrt{s_{NN}} = 200\,\mathrm{GeV}$ compared with Phobos data for different centrality classes [119]. The solid curves show the produced charged hadron distributions calculated by the extended Relativistic Diffusion model. The dot-dashed curves show the model contribution for the mid-rapidity region for produced pions, kaons and protons, whereas the dashed curves show the contribution only for pions. Kaons and protons are not explicitly shown. The dotted curves show the model contribution for pions coming from the two fragmentation regions.

of the mid-rapidity region across all examined centrality classes with a high level of precision. Moreover, the positive rapidity region associated with the deuteron-going side shows agreement with the measured data. However, further discussion is warranted for the negative rapidity region linked to the gold-going side.

This proficiency extends further to the replication of the both peaks observed in the charged-hadron production. The influence of the Jacobian for the mid-rapidity source is found to be negligibly small. As a consequence, the dip observed in the mid-rapidity region can be attributed to the smallness of the fragmentation sources at midrapidity.

A comparison between our calculations and previously published results, such as [74], reveals a better agreement with the experimental data. Our calculations demonstrate improved agreement within the mid-rapidity regime. A comparison with the Relativistic Diffusion model utilizing Gaussian rapidity distributions [14] yields compatible results. Even the sub-distributions exhibit remarkable agreement, barring the ultra-peripheral collisions where our calculations indicate a more pronounced contribution from the fragmentation sources.

Regarding the gold-going side, the phenomenon of underestimating hadron production has also been observed in previous calculations, as evident in [120] and [121]. These findings are particularly relevant in the light of the binding energy of a proton (928.9 MeV) or neutron (927.7 MeV), which are significantly higher than that of a deuteron (2.225 MeV). Consequently, shortly after a collision, the deuteron is expected to decay into two free nucleons.

Considering this decay process, it becomes apparent that the validity of the Glauber-calculated number of participants could be questioned, as the assumption of a single collision may not hold. To address this, we scale N_{part}^{Au} by a factor of 2.2. This adjustment leads to a more accurate description of the observed trends.

Table 7.1 presents the total amount of produced hadrons, computed through the utilization of the extended Relativistic Diffusion model. This summation encompasses pions, kaons, and protons stemming from the mid-rapidity source, with exclusively pions emerging from the fragmentation sources.

The preponderance of hadrons arises from the gluon-gluon mid-rapidity source. The classification of centrality classes is taken from the Phobos collaboration and is delineated in table 7.2.

The amount of produced hadrons N_{ch} exhibits a monotonically increasing trend, with central collisions yielding ~ 7 more hadrons than ultra-peripheral collisions.

It is intriguing to observe that the ratio R_d^{Au} representing the production of hadrons between the fragmentation sources shifts towards the deuteron's fragmentation source.

central.	N_{ch}	N_{ch}^{gg}	N_{π}^{gg}	N_{K}^{gg}	N_{p}^{gg}	N_{Au}^{qg}	N_{d}^{qg}	R_{d}^{Au}	R_{qg}^{gg}
0-20%	162.7	52.4	20.3	17.7	14.4	94.7	15.7	6.0	0.475
20-40%	110.4	36.2	14.1	12.3	9.8	59.7	14.5	4.1	0.488
min.bias	83.5	27.8	10.8	9.4	7.5	43.1	12.6	3.4	0.499
40-60%	73.7	24.9	9.7	8.5	6.7	35.9	12.9	2.8	0.510
60-80%	45.5	16.1	6.3	5.5	4.3	18.9	10.4	1.8	0.549
80-100%	25.9	9.2	3.6	3.1	2.4	9.2	7.5	1.2	0.550

Table 7.1.: Calculated produced charged hadrons N_{ch} for d-Au collisions at $\sqrt{s_{NN}} = 200\,\mathrm{GeV}$ for various centrality classes and minimum bias. The calculations integrate over the full range of pseudorapidity. The extended Relativistic Diffusion model comprises three individual production sources: the mid-rapidity source N_{ch}^{gg} and two fragmentation sources $N_{d/Au}^{qg}$. The produced charged hadrons for the mid-rapidity include pions N_{π}^{gg}, kaons N_{K}^{gg}, and protons N_{p}^{gg}, whereas the fragmentation regions only contain pions. The ratio between the two fragmentation sources are shown as $R_{d}^{Au} = N_{Au}^{qg}/N_{d}^{qg}$. The ratio $R_{qg}^{gg} = N_{\mathrm{ch}}^{gg}/\Sigma_i N_i^{qg}$ represents the proportion of produced charged hadrons in the mid-rapidity region compared to the combined fragmentation regions.

central.	N_{part}^{Au}	Q_0^2 (GeV^2/c^2)	$D^d\tau_y$	$\tau_{\mathrm{int}}^d/\tau_y^d$	$D^{Au}\tau_y$	$\tau_{\mathrm{int}}^{Au}/\tau_y$	χ^2/N_{dof}
0-20%	13.5	0.054	2.0	0.1	9.0	0.1	0.890
20-40%	8.9	0.051	2.0	0.1	8.0	0.2	1.019
min.bias	6.6	0.050	2.0	0.1	8.0	0.2	0.803
40-60%	5.4	0.050	2.0	0.1	8.0	0.2	1.280
60-80%	2.9	0.050	2.0	0.1	7.0	0.3	1.132
80-100%	1.6	0.042	3.0	0.2	6.0	0.4	0.180

Table 7.2.: Model parameters extracted from the Relativistic Diffusion model used to compute pseudorapidity distributions for d-Au collisions at $\sqrt{s_{NN}} = 200\,\mathrm{GeV}$. The number of participants N_{part}^{Au} were sourced from [117]. The parameters $\tau_{\mathrm{int}}^i/\tau_y^i$ and $D^i\tau_y^i$ are dimensionless.

Also for this calculation, we see a slight deviation compared to the data for pseudorapidities near the beam rapidity. As for symmetric collisions the suppression factor of $(1-x)^4$ might be a reason, why the hadron production is underestimated in that area.

Table 7.2 presents a comprehensive overview of the cumulative yield of produced hadrons, calculated using the extended Relativistic Diffusion model. The results are categorized into distinct centrality classes, ranging from the most central (0-20%) to the most peripheral (80-100%) collisions. The number of participants for the deuteron, N^d_{part}, are given by $2.0, 1.9, 1.7, 1.4, 1.1$ and for minimum bias 1.7 [117].

The cumulative count includes pions, kaons, and protons originating from the mid-rapidity source, while exclusively pions emerge from the fragmentation sources. Notably, the primary contribution to the hadron yield arises from the gluon-gluon mid-rapidity source.

Concerning the parameter governing the diffusion process, it is noteworthy that both fragmentation sources exhibit very short interaction times. One plausible explanation is that the potential for longitudinal momentum loss is constrained considerably due to the relatively low overall energy, as compared to energies at the LHC.

Given the limited duration of interaction times, the influence of the diffusion process is extremely minor, preventing a valuable interpretation of the centrality dependence of the diffusion coefficient.

We continue with collisions at LHC energies.

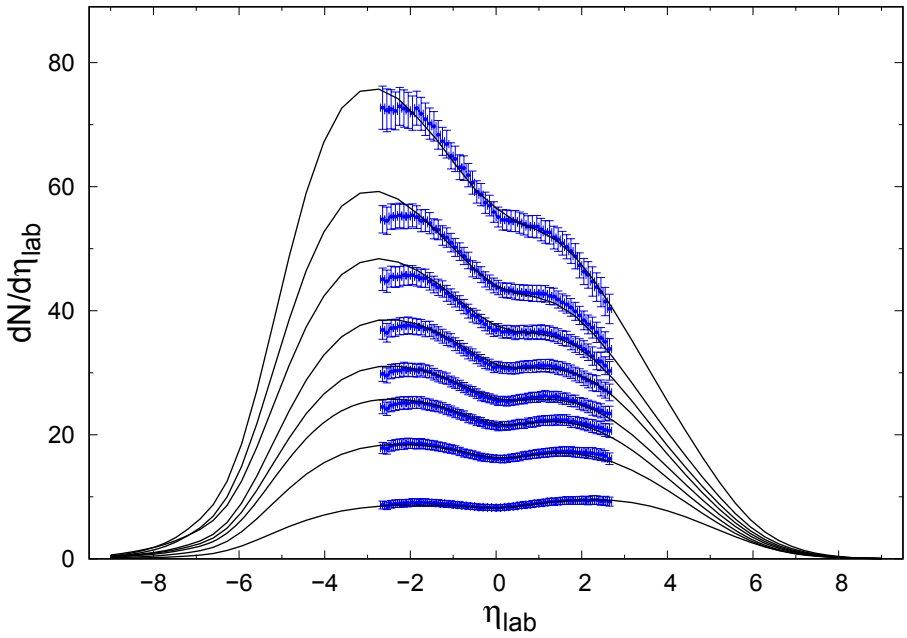

(a) Experimental data from ATLAS ($p_T > 0$) [122]. The centrality classes from top to bottom are 0-1%, 1-5%, 5-10%, 10-20%, 20-30%, 30-40%, 40-60%, 60-90%.

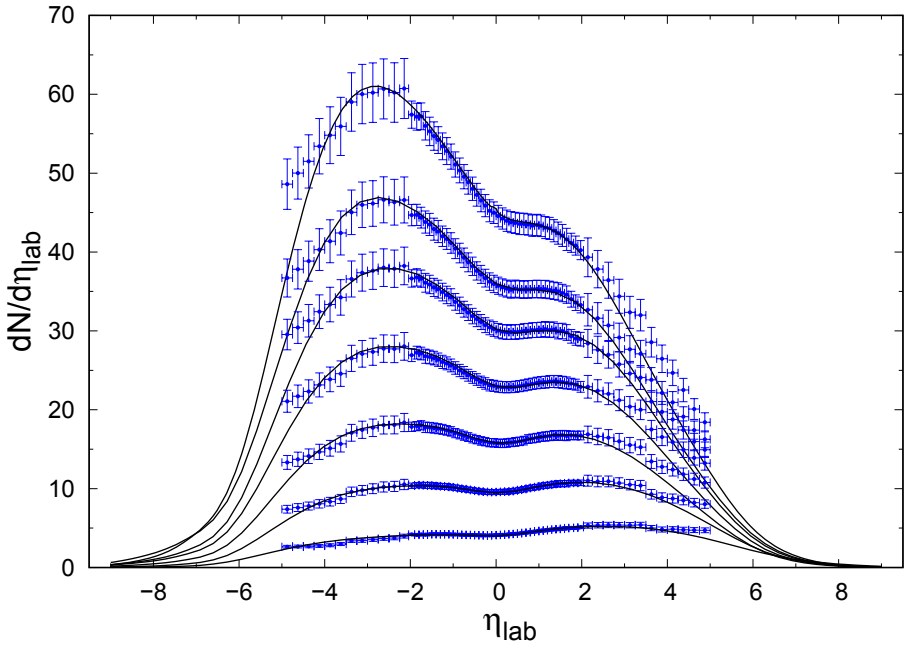

(b) Experimental data from ALICE for $|\eta| < 2$ from [104], all others from [105]. The centrality classes from top to bottom are 0-5%, 5-10%, 10-20%, 20-40%, 40-60%, 60-80%, 80-100%.

Figure 7.3.: Calculated pseudorapidity distributions of produced charged hadrons for p-Pb collisions at $\sqrt{s_{NN}} = 5.02\,\text{TeV}$ compared with data for various centrality classes. The solid curves represent the calculated distributions of produced charged hadrons using the extended Relativistic Diffusion model.

7.2. Charged hadrons for p-Pb collisions at 5 TeV

We conduct an analysis of centrality-dependent calculations focusing on the pseudorapidity distributions of produced charged hadrons in p-Pb collisions at $\sqrt{s_{NN}} = 5\,\text{TeV}$. To conduct a comprehensive analysis, we compare our calculations with experimental data obtained from both the ALICE and ATLAS collaborations.

This choice is motivated by several factors. Firstly, the ATLAS data covers a broader range in pseudorapidity over an extended period of time. But, ALICE recently published experimental data for the pseudorapidity range of $\eta < 5$. Furthermore, variations in the centrality classes between the two collaborations offer an intriguing avenue for comparison.

For asymmetric collisions, distinct calculations are necessitated for forward and backward rapidities. In the case of p-Pb collisions, the proton and lead beams possess disparate momenta: $4.0\,\text{TeV}/c$ for the proton beam and $1.577\,\text{TeV}/c$ for the lead beam. These beam momenta correspond to beam rapidities of $y^{p}_{\text{beam}} = 9.051$ and $y^{Pb}_{\text{beam}} = 8.120$, respectively. As a result, the energy per nucleon-nucleon pair is $\sqrt{s_{NN}} = 5.023\,\text{TeV}$, which corresponds to a beam rapidity in the nucleon-nucleon frame of reference of $y_{\text{beam}} = 8.586$.

It is important to account for a rapidity shift of $\Delta y = 0.465$ between the laboratory frame and the nucleon-nucleon pair reference frame when calculating rapidity distributions.

To conform with the convention embraced in this thesis, wherein positive rapidity corresponds to the proton beam, a transformation of the experimental data of ALICE from the laboratory frame Pb-p to p-Pb, as illustrated in figure 7.1, was required. The procedure involves shifting the experimental data to the center of mass frame, performing a mirroring operation, and then shifting it to the other laboratory frame.

The geometric parameters essential for these calculations are established through collaborations within the experimental community and will be subsequently detailed. These parameter sources are consistent with those employed for the experimental data.

To perform the computations, we apply our extended Relativistic Diffusion model with the three production sources, which is elucidated in section 6.1. These include the mid-rapidity source N^{gg}_{ch} and two fragmentation sources $N^{qg}_{p/Pb}$, which collectively shape the spectra of charged hadrons. The mid-rapidity source encompasses various charged hadrons such as pions N^{gg}_{π}, kaons N^{gg}_{K}, and protons N^{gg}_{p}, while the fragmentation sources only involve pions.

In this process, we adhere to the same parameter values as employed in the preceding calculations. Specifically, we use a gluon saturation scale exponent $\lambda = 0.288$

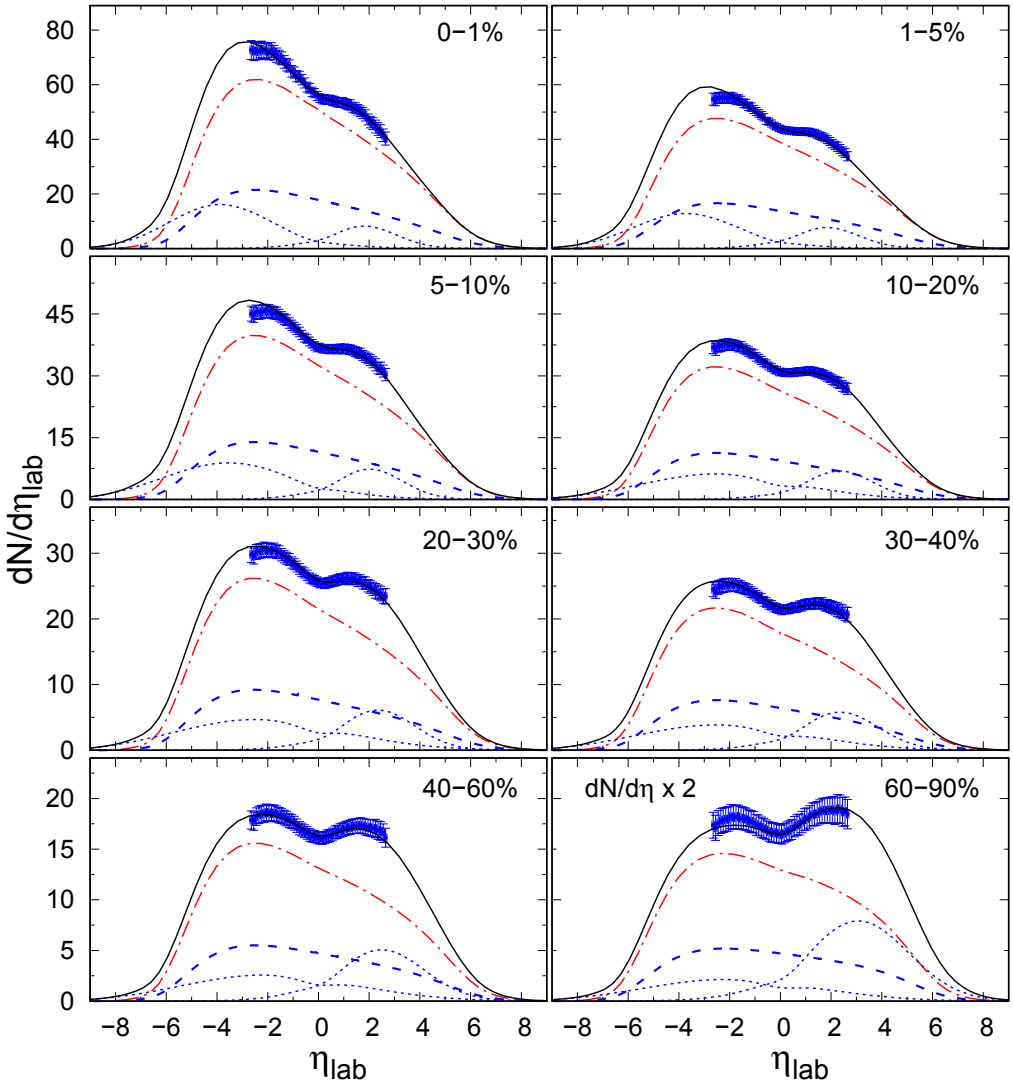

Figure 7.4.: Calculated pseudorapidity distributions of produced charged hadrons for p-Pb collisions at $\sqrt{s_{NN}} = 5.02\,\text{TeV}$ compared with ATLAS data for different centrality classes and $p_T > 0$ [122]. The solid curves show the produced charged hadron distributions calculated by the extended Relativistic Diffusion model. The dot-dashed curves show the model contribution for the mid-rapidity region for produced pions, kaons and protons, whereas the dashed curves show the contribution only for pions. Kaons and protons are not explicitly shown. The dotted curves show the model contribution for pions coming from the two fragmentation regions.

and $x_0 = 1$. The initial saturation momentum Q_0^2, exhibits only minor variations in response to changes in centrality.

To account for the contributions from the fragmentation sources, we introduce a diffusion mechanism that guides our rapidity distributions towards τ_{int}, utilizing the time scale τ_y. However, the precise value of the time scale derived from τ_y remains uncertain within our model. It is worth noting that these distributions deviate significantly from the equilibrium distribution characterized by y_{eq}.

For the calculation of the Jacobian associated with the fragmentation sources, we employ an average transverse momentum $\langle p_T \rangle$ value of $0.3\,\text{GeV}/c$ and the pion mass m_π.

The computed pseudorapidity distributions for p-Pb collisions compared with ATLAS and ALICE data are illustrated in figure 7.3. They both show good agreement with the experimental data. Similar calculations but using different models are presented in [8], but these are confined to the experimental data reported in [104].

Notably, as of the completion of this thesis, there are no other published calculations available for the recently released data from [105].

Calculations compared with ATLAS data

A notable distinction in the ATLAS data lies in the selection of the centrality classes. Specifically, the most peripheral collisions are defined within the range of 60% to 90%.

Figure 7.4 illustrates the computed centrality dependence across various centrality classes. Our analysis demonstrates a remarkable concurrence between the calculated results and the experimental data, encompassing a diverse range of pseudorapidity values. The model effectively captures the characteristics of the mid-rapidity region for all examined centrality classes with a high degree of accuracy.

An overview of the total yield of produced hadrons, calculated through the implementation of the extended Relativistic Diffusion model is provided in Table 7.3

The outcomes are categorized into distinct centrality classes, spanning from the most central (0-1%) to the most peripheral (60-90%) collisions. This inquiry encompasses the entire pseudorapidity spectrum, facilitating a thorough investigation of particle production dynamics.

The cumulative count encompasses pions, kaons, and protons originating from the mid-rapidity source, while exclusively pions emerge from the fragmentation sources. The primary contribution of hadrons stems from the gluon-gluon mid-rapidity source.

central.	N_{ch}	N_{ch}^{gg}	N_{π}^{gg}	N_{K}^{gg}	N_{p}^{gg}	N_{Pb}^{qg}	N_{p}^{qg}	R_{p}^{Pb}	R_{qg}^{gg}
0-1%	590.9	481.3	168.8	161.8	150.5	82.1	27.7	3.0	4.4
1-5%	467.0	374.8	132.2	126.1	116.5	66.5	25.9	2.6	4.1
5-10%	395.8	315.4	111.6	106.2	97.6	55.6	25.0	2.2	3.9
10-20%	325.8	257.5	91.5	86.7	79.3	44.4	24.1	1.8	3.8
20-30%	270.2	211.5	75.4	71.3	64.8	35.8	23.1	1.5	3.6
30-40%	228.5	176.6	63.1	59.5	54.0	29.5	22.6	1.3	3.4
40-60%	171.8	129.7	46.5	43.8	39.5	20.3	21.9	0.9	3.1
60-90%	92.6	64.3	23.3	21.8	19.3	8.4	19.9	0.4	2.3

Table 7.3.: Calculated produced charged hadrons N_{ch} for p-Pb collisions at $\sqrt{s_{NN}} = 5.02\,\mathrm{TeV}$ for various centrality classes and minimum bias. The calculations integrate over the full range of pseudorapidity. The extended Relativistic Diffusion model comprises three individual production sources: the mid-rapidity source N_{ch}^{gg} and two fragmentation sources $N_{p/Pb}^{qg}$. The produced charged hadrons for the mid-rapidity include pions N_{π}^{gg}, kaons N_{K}^{gg}, and protons N_{p}^{gg}, whereas the fragmentation regions only contain pions.

central.	N_{part}^{Pb}	$Q_0^2(\mathrm{GeV}/c)^2$	$D^p\tau_y$	$\tau_{\mathrm{int}}^{p}/\tau_y$	$D^{Pb}\tau_y$	$\tau_{\mathrm{int}}^{Pb}/\tau_y$	χ^2/N_{dof}
0-1%	17.2	0.098	1.5	0.80	6.0	0.30	0.124
1-5%	15.1	0.085	1.5	0.80	6.0	0.35	0.357
5-10%	13.6	0.078	1.5	0.72	10.0	0.40	0.435
10-20%	12.0	0.070	1.5	0.60	11.0	0.80	0.190
20-30%	10.4	0.065	2.0	0.60	13.0	0.80	0.151
30-40%	8.8	0.062	2.2	0.60	13.0	0.80	0.175
40-60%	6.4	0.058	3.0	0.55	13.0	1.00	0.065
60-90%	3.0	0.047	5.0	0.38	13.0	1.00	0.112

Table 7.4.: Model parameter from Relativistic Diffusion model for calculated pseudorapidity distributions for p-Pb collisions at $\sqrt{s_{NN}} = 5.02\,\mathrm{TeV}$. The number of participants N_{part}^{Pb} were taken from the Glauber Monte Carlo calculations by ATLAS [122] for different centrality classes. In asymmetric collisions participants for projectile and target are treated separately, where $\langle N_{part}\rangle = N_{\mathrm{part}}^{p} + N_{\mathrm{part}}^{Pb}$ with $N_{\mathrm{part}}^{p} = 1$.

The classification of centrality classes is derived from the ATLAS collaboration and is delineated in table 7.4. The count of produced hadrons N_{ch} exhibits a monotonic trend, with central collisions yielding approximately six times more hadrons compared to ultra-peripheral collisions.

Two essential ratios are offered to illuminate the underlying production mechanisms. The first, denoted as R_p^{Pb}, gauges the relative production of charged hadrons between the two distinct fragmentation sources. The ratio undergoes a decreasing transition as collisions become more ultra-peripheral, leading to a shift in production emphasis towards the proton-like fragmentation source.

The ration R_p^{Pb} states a value of less than 0.5 for ultra-peripheral collisions. However, when observing the amplitudes of both peaks in figure 7.4 for the most peripheral collisions, the mentioned shift in the relevance of the fragmentation sources is not discernible as a shift in the global peak towards the proton-going region.

The underlying reason for this is still the substantial asymmetry of the gluon-gluon source towards the lead-going region, attributed in the definition of the selected centrality class. The chosen centrality class spans a wide range (60-90%) and excludes the most ultra-peripheral region (90-100%).

The ratio denoted as R_{gg}^{qg} serves to characterize the proportion of charged hadrons originating from the mid-rapidity region in comparison to the collective contributions from the fragmentation regions, which has an scaling behaviour of

$$R_{qg}^{gg} \sim \frac{A^{1/3} N_{\mathrm{part}}}{A^{1/3} + N_{\mathrm{part}}}. \tag{7.1}$$

Upon further analysis of the model parameters listed in table 7.4 concerning the diffusion process, it shows that the behaviour of the proton-going fragmentation sources exhibits similarities to that of the Pb-Pb fragmentation sources, as mentioned in section 6.2.

However, a contrasting pattern emerges for the lead-going fragmentation source. In this scenario, the produced hadrons exhibit a more pronounced loss of momentum in the beam direction, consequently driving an elevation in the diffusion coefficient. Concurrently, the interaction time also experiences an increase. The interaction time signifies the duration during which the produced hadron is in the process of attaining its ultimate momentum state.

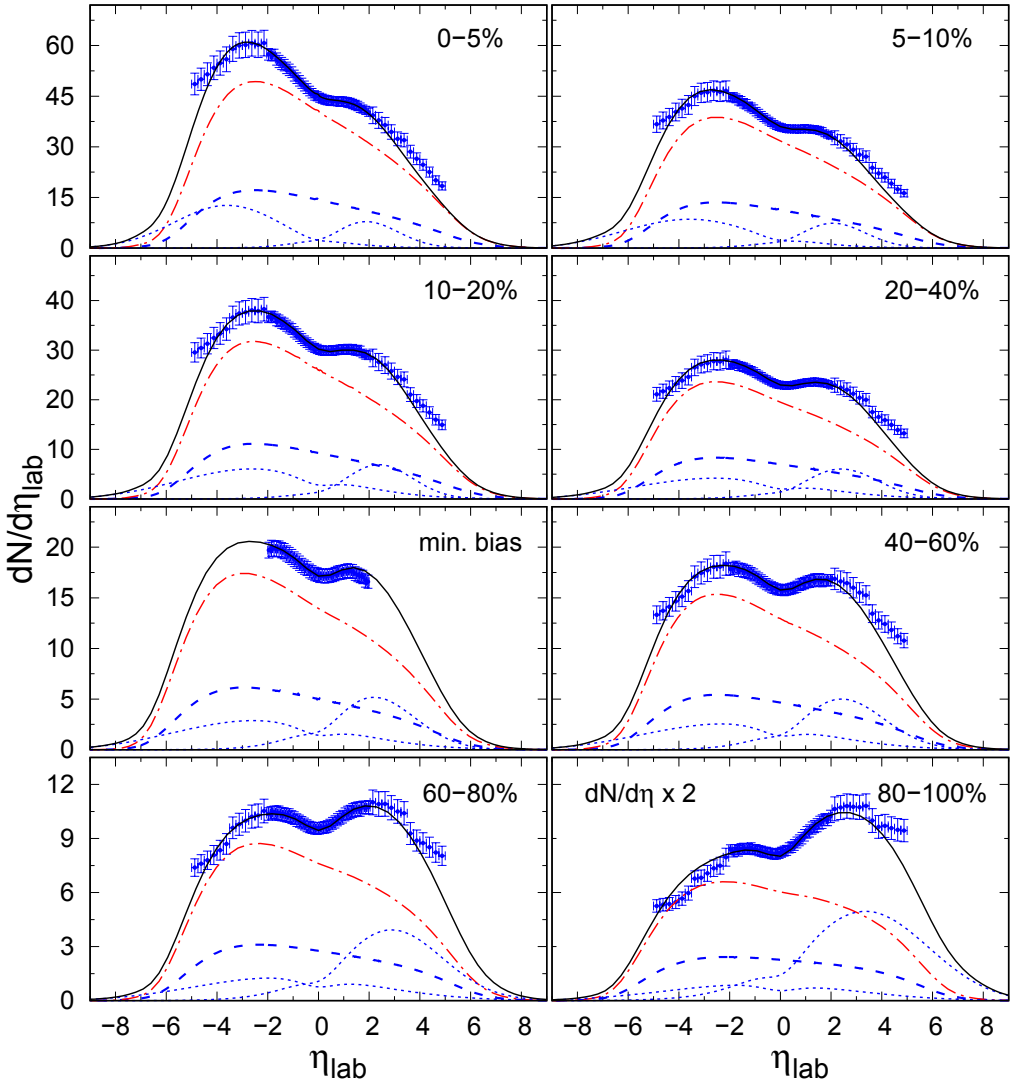

Figure 7.5.: Calculated pseudorapidity distributions of produced charged hadrons for p-Pb collisions at $\sqrt{s_{NN}} = 5.02\,\text{TeV}$. The data are measured by the ALICE collaboration and represent different centrality classes. The data for minimum bias come from [123]. The data for the different centrality classes for $|\eta| < 2.0$ come from [104], whereas for $|\eta| > 2.0$ from [105]. The solid distribution shows the full-calculated pseudorapidity distribution, whereas the dot-dashed distribution shows the combined distribution of charged hadrons produced by gluon-gluon interactions for pions, kaons and protons. The dashed distribution shows only the pions produced by gluon-gluon interactions and the dotted distributions show the produced pions coming from quark-gluon interactions. Kaons and protons are not shown explicitly for gluon-gluon interactions. The most peripheral distribution is scaled by a factor of two for better visibility.

Calculations compared with ALICE data

Figure 7.5 shows the calculated centrality dependence across a range of centrality classes. When compared to the data from ATLAS, it is important to note that the data obtained from ALICE corresponds to slightly different centrality classes.

The most significant distinction can be attributed to the delineation of ultra-peripheral collisions. In the ALICE data, this category extends to include the most peripheral region and reduces the range of less peripheral collisions (80-100%).

Our analysis exhibits a remarkable agreement between the computed outcomes and the experimental data, spanning a wide spectrum of pseudorapidity values.

In table 7.5 we see the calculated produced charged hadrons. Considering the ratio of the mid-rapidity and of the combined fragmentation sources we found the same relation than for ATLAS data.

In the context of ultra-peripheral collisions, a transition is observed wherein the dominant peak, the global maximum, of the pseudorapidity distribution shifts from the negative to the positive pseudorapidity region. This shift signifies that in the region, associated with the proton, a higher number of hadrons are produced compared to the lead region.

This phenomenon finds explanation within our model, indicating the relevance of fragmentation sources in describing the production of charged hadrons.

The rationale behind this observation can be elucidated as follows. We investigate the scaling behaviour of the fraction of produced hadrons originating from the fragmentation sources, denoted as R_p^{Pb}. Its scaling behaviour is basically governed by $\sim N_{\text{part}}^{Pb}\ A^{-1/3}$, primarily influenced by the fact that the lead serves both as the projectile and the target within collisions.

For situations where $A^{1/3} > N_{\text{part}}^{Pb}$, it is anticipated that the proton-like fragmentation source yields more hadrons than the Pb-like fragmentation source. So far the same argument can be applied to the data of ultra-peripheral collisions at ATLAS.

Furthermore, it is anticipated that the gluon-gluon source will exhibit a symmetrical nature, regarding positive and negative rapidities, in the limit of N_{part}^{Pb}, resulting in an approximately constant behaviour within the region where both peaks are situated, particularly evident in the case of the most ultra-peripheral collisions, as depicted in Figure 7.5.

In conclusion, the scaling behaviour of the fragmentation sources with respect to centrality, combined with the constant nature of the mid-rapidity source, characterizes the transition of the dominant peak towards ultra-peripheral collisions within the pseudorapidity distribution.

central.	N_{ch}	N_{ch}^{gg}	N_{π}^{gg}	N_{K}^{gg}	N_{p}^{gg}	N_{Pb}^{qg}	N_{p}^{qg}	R_{p}^{Pb}	R_{qg}^{gg}
0-5%	478.7	386.7	136.1	130.1	120.5	66.1	26.1	2.5	4.2
5-10%	384.8	307.3	108.7	103.4	95.2	53.1	24.7	2.1	3.9
10-20%	320.3	253.9	90.2	85.5	78.2	42.9	23.8	1.8	3.8
20-40%	246.0	191.9	68.5	64.7	58.8	31.6	22.6	1.4	3.5
min.bias	187.5	143.8	51.4	48.5	43.9	22.0	21.8	1.0	3.3
40-60%	169.0	127.8	45.8	43.1	38.9	19.9	21.3	0.9	3.1
60-80%	105.9	75.8	27.4	25.6	22.8	10.4	19.8	0.5	2.5
80-100%	49.7	31.0	11.6	10.5	8.8	3.7	15.1	0.2	1.6

Table 7.5.: Calculated produced charged hadrons N_{ch} for p-Pb collisions at $\sqrt{s_{NN}} = 5.02\,\mathrm{TeV}$ for various centrality classes and minimum bias. The extended Relativistic Diffusion model comprises three individual production sources: the mid-rapidity source N_{ch}^{gg} and two fragmentation sources N_{i}^{qg}. The produced charged hadrons for the mid-rapidity include pions, kaons, and protons, whereas the fragmentation regions only contain pions. The ratio between the two fragmentation sources are shown as $R_{p}^{Pb} = N^{Pb}/N^{p}$, whereas the ratio $R_{gg}^{qg} = N^{gg}/N^{qg}$ represents the proportion of produced charged hadrons in the mid-rapidity region compared to the combined fragmentation regions.

central.	N_{part}^{Pb}	$Q_0^2(\mathrm{GeV}/c)^2$	$D^{p}\tau_{y}$	τ_{y}^{p}/τ_{y}	$D^{Pb}\tau_{\mathrm{int}}$	$\tau_{\mathrm{int}}^{Pb}/\tau_{y}$	χ^2/N_{dof}
0-5%	14.70	0.090	1.5	0.80	6.0	0.40	0.342
5-10%	13.00	0.079	1.5	0.72	10.0	0.40	0.250
10-20%	11.70	0.071	1.5	0.60	11.0	0.80	0.349
20-40%	9.40	0.064	2.0	0.60	13.0	0.80	0.256
min.bias	6.90	0.061	2.9	0.60	13.0	0.90	0.100
40-60%	6.42	0.057	3.0	0.60	13.0	1.00	0.207
60-80%	3.81	0.048	5.0	0.45	13.0	1.50	0.202
80-100%	1.94	0.028	9.5	0.35	13.0	2.20	0.545

Table 7.6.: Model parameter from Relativistic Diffusion model for calculated pseudorapidity distributions for p-Pb collisions at $\sqrt{s_{NN}} = 5.02\,\mathrm{TeV}$. The number of participants N_{part}^{Pb} were taken from the Glauber Monte Carlo calculations by ALICE [123] for different centrality classes. In asymmetric collisions participants for projectile and target are treated separately, where $\langle N_{part} \rangle = N_{\mathrm{part}}^{p} + N_{\mathrm{part}}^{Pb}$ with $N_{\mathrm{part}}^{p} = 1$.

7.3. Charged hadrons for p-Pb collisions at 8 TeV

We delve into a comprehensive analysis of centrality-dependent calculations, concerning the pseudorapidity distributions of produced charged hadrons in p-Pb collisions. This pertains to the highest currently available energy regime at LHC.

In the context of asymmetric collisions, distinct calculations are required for forward and backward rapidities, unlike the simplified symmetry assumptions applicable to symmetric collisions. The experimental data encompasses a range of 3.6 units of pseudorapidity ($|\eta| < 1.8$) and has been published in [124].

In p-Pb collisions, the proton and lead beams possess differing momenta: 6.5 TeV/c for the proton and 2.563 TeV/c for the lead beam. The corresponding beam rapidities are $y^{p}_{\text{beam}} = 9.536$ and $y^{Pb}_{\text{beam}} = 8.606$. This configuration results in an energy per nucleon-nucleon pair of $\sqrt{s_{NN}} = 8.162$ TeV, corresponding to a beam rapidity in the nucleon-nucleon frame of reference of $y_{\text{beam}} = 9.071$.

It's important to consider a rapidity shift of $\Delta y = 0.465$ between the laboratory frame and the nucleon-nucleon pair reference frame, which remains consistent with other LHC energies, when calculating rapidity distributions.

central.	N_{ch}	N^{gg}_{ch}	N^{gg}_{π}	N^{gg}_{K}	N^{gg}_{p}	N^{qg}_{Pb}	N^{qg}_{p}	R^{Pb}_{p}	R^{gg}_{qg}
0-5%	649.3	538.7	188.3	181.1	169.4	82.6	29.7	2.8	4.8
5-10%	512.5	419.5	147.3	141.1	131.1	65.6	28.4	2.3	4.5
10-20%	414.3	335.0	118.2	112.7	104.1	53.4	26.8	2.0	4.2
20-40%	305.3	241.6	85.7	81.4	74.5	38.9	25.2	1.5	3.8
min.bias	228.4	176.9	62.9	59.6	54.4	27.1	24.8	1.1	3.4
40-60%	203.1	155.5	55.4	52.4	47.6	23.9	24.0	1.0	3.2
60-80%	115.2	81.8	29.5	27.7	24.7	11.8	21.6	0.5	2.5
80-100%	44.0	26.0	9.9	8.9	7.2	3.7	14.6	0.3	1.4

Table 7.7.: Calculated produced charged hadrons N_{ch} for p-Pb collisions at $\sqrt{s_{NN}} = 8.16$ TeV for different centrality classes. The centrality classes are comparable with ALICE data from [124]. Calculations include the full range of pseudorapidity. The RDM consists of three individual production sources, the mid-rapidity source N_{gg} and two fragmentation sources N^{qg}_{i}. The ratio between the fragmentation regions is shown via $R^{Pb}_{p} = N^{Pb}_{qg}/N^{p}_{qg}$. The ration between the mid-rapidity region and the combined fragmentation region is shown via $R^{gg}_{qg} = N^{gg}/N^{qg}$. The produced charged hadrons for the mid-rapidity contain pions, kaons and protons, whereas the fragmentation regions only contain pions.

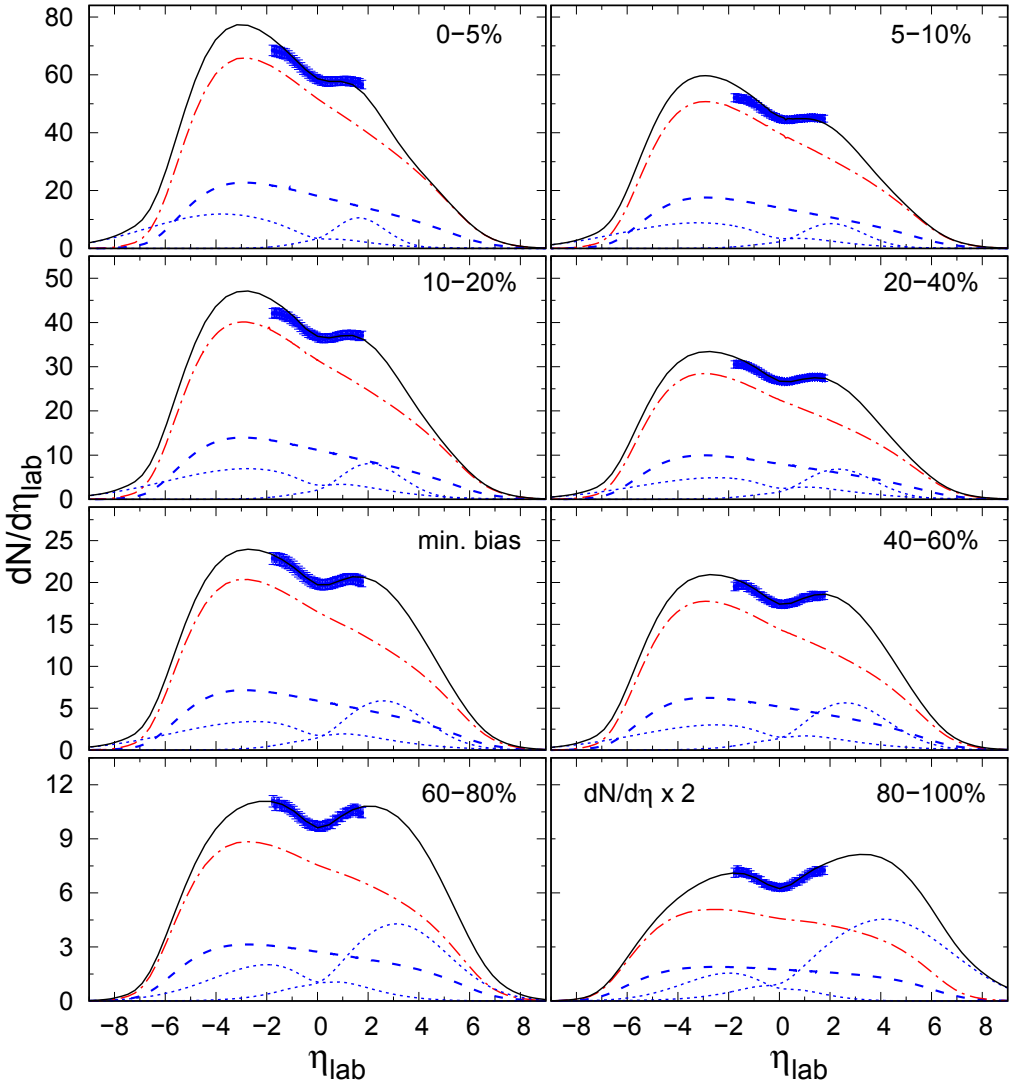

Figure 7.6.: Calculated pseudorapidity distributions of produced charged hadrons for p-Pb collisions at $\sqrt{s_{NN}} = 8.16\,\text{TeV}$ compared with ALICE data for different centrality classes [124]. The solid curves show the produced charged hadron distributions calculated by the extended Relativistic Diffusion model. The dot-dashed curves show the model contribution for the mid-rapidity region for produced pions, kaons and protons, whereas the dashed curves show the contribution only for pions. Kaons and protons are not explicitly shown. The dotted curves show the model contribution for pions coming from the two fragmentation regions. The scale of the most peripheral centrality is scaled by a factor of two for better visibility. The experimental data are mirrored from Pb-p to p-Pb convention.

central.	N_{part}^{Pb}	$Q_0^2(\mathrm{GeV}/c)^2$	$D^p\tau_y$	$\tau_{\mathrm{int}}^p/\tau_y$	$D^{Pb}\tau_y$	$\tau_{\mathrm{int}}^{Pb}/\tau_y$	χ^2/N_{dof}
0-5%	16.00	0.092	1.0	1.00	13.0	0.40	0.477
5-10%	14.00	0.080	1.5	0.80	13.0	0.60	1.697
10-20%	12.40	0.070	1.5	0.80	13.0	0.80	0.828
20-40%	9.90	0.061	2.0	0.70	13.0	1.00	0.492
min.bias	7.09	0.058	2.9	0.60	13.0	1.00	0.065
40-60%	6.47	0.054	3.0	0.60	13.0	1.00	0.240
60-80%	3.53	0.043	5.0	0.45	6.0	1.50	0.066
80-100%	1.76	0.019	13.0	0.25	4.0	1.50	0.090

Table 7.8.: Model parameter from Relativistic Diffusion model for calculated pseudorapidity distributions for p-Pb collisions at $\sqrt{s_{NN}} = 8.16\,\mathrm{TeV}$. The number of participants N_{part}^{Pb} were taken from the Glauber Monte Carlo calculations by ALICE with the CL1 estimator [124] for different centrality classes. In asymmetric collisions participants are treated separately, where $\langle N_{part}\rangle = N_{\mathrm{part}}^{p} + N_{\mathrm{part}}^{Pb}$ with $N_{\mathrm{part}}^{p} = 1$.

In figure 7.6, we present the computed centrality dependence for different centrality classes. The results obtained from our analysis demonstrate a remarkable agreement between the computed values and the experimental data. Our model accurately captures the behaviour of the mid-rapidity region across all investigated centrality classes with a high degree of accuracy.

The effectiveness of our model is further demonstrated by its ability to accurately replicate the expected presence of dual maxima in the distribution of charged-hadron production. Furthermore, our analysis reveals that the influence of the Jacobian related to the mid-rapidity source is insignificantly small. As a result, the depression observed in the mid-rapidity region can be attributed to the absence of the fragmentation sources.

Table 7.7 provides an overview of the total quantity of produced hadrons, as computed using the extended Relativistic Diffusion model.

The predominant contribution of hadrons is attributed to the gluon-gluon mid-rapidity source. The count of produced hadrons N_{ch} exhibits a monotonic increase, with central collisions producing ~ 15 times more hadrons compared to ultra-peripheral collisions.

The model parameter describing the diffusion process are shown in table 7.8. The diffusion process for the proton-going fragmentation source share the same centrality behaviour as for p-Pb collision at $\sqrt{s_{NN}} = 5.02\,\mathrm{TeV}$.

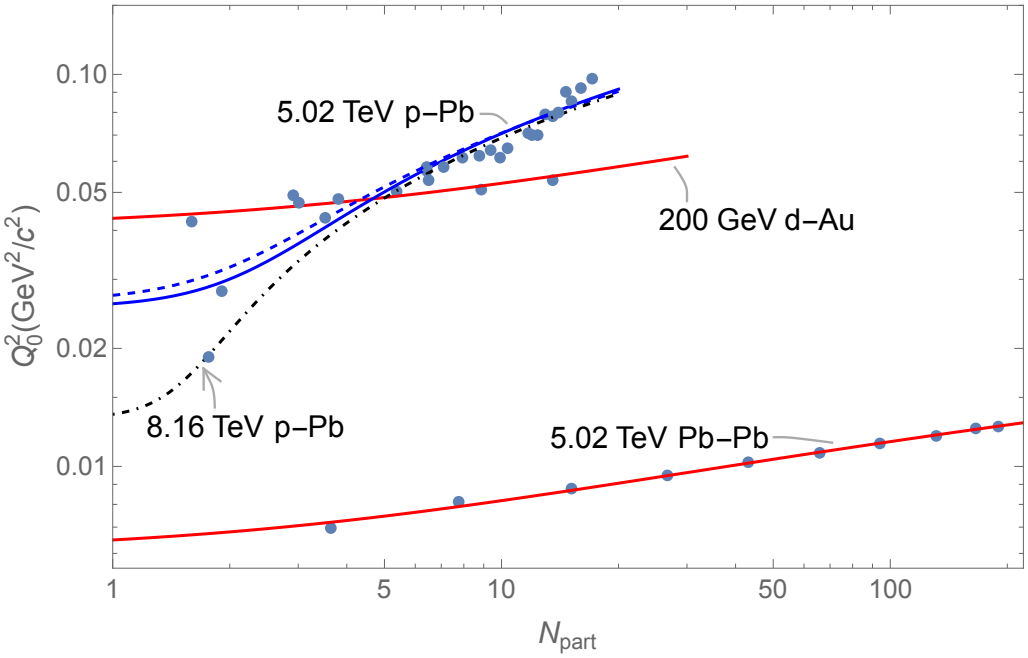

Figure 7.7.: Double logarithmic plot illustrating the centrality dependence of Q_0^2, considering N_{part} for RHIC and LHC energies. In cases of asymmetric collisions, participants from the projectile and target are treated individually, with target participants being employed here. The upper blue curve pertains to calculation in comparison with ATLAS data, while the lower curve corresponds to the calculations compared to ALICE.

		$\sqrt{s_{NN}}$ (TeV)	$\widehat{Q}_0^2$ (GeV$^2/c^2$)	N_0	d
Pb-Pb	ALICE	5.023	0.0030	1.00	0.8467
d-Au	PHOBOS	0.200	0.0201	1.30	0.8398
p-Pb	ATLAS	5.023	0.0132	1.32	3.0148
p-Pb	ALICE	5.023	0.0127	1.49	3.3397
p-Pb	ALICE	8.160	0.0066	1.21	6.2217

Table 7.9.: Values for the centrality-depended parametrization of Q_0^2, fitted to the results of previous calculations of the pseudorapidity distributions at RHIC and LHC energies.

Centrality dependence of the initial saturation scale

The initial saturation scale momentum Q_0, as employed in the definition of the saturation scale, see equation (3.26), fixes the saturation scale at a $y = 0$ to a specific value.

In the literature, the initial saturation scale was fixed to $Q_0^2 = 0.09\,\mathrm{GeV}^2/c^2$, obtained from fitting HERA data [67].

Nonetheless, there exists no direct calculation relying on a fixed Q_0 in conjunction with the number of participants derived from computations by the corresponding experimental collaborations. Instead, the collision's geometry is translated into the treatment of the dipole cross section, mainly involving adjustments to the thickness function [10, 12].

The dependence of Q_s^2 on the mass number A can be regarded as an approximation applicable primarily to very large collision systems. However, the behaviour of this dependence when the mass number decreases or when only a limited number of participants are involved remains largely unexplored.

In accordance with calculations presented in [121], Q_s^2 itself is adjusted in relation to the number of participants. Consequently, we opt to incorporate this uncertainty by allowing a slight variability in Q_0^2.

Based on the centrality-dependent calculations of pseudorapidity distributions discussed in the preceding sections, our objective is to establish a parametrization for this centrality dependence.

Our proposition involves a scaling of Q_s^2 in correspondence with the running coupling, as defined in equation (3.46), leading to a refined formulation of Q_0^2. This revised definition is designated as $\widehat{Q}_0^2$ and is expressed as

$$\widehat{Q}_0^2 = Q_0^2\ \alpha_s(p^2). \tag{7.2}$$

Subsequently, we proceed to establish a parametrization for p^2, defined by

$$p^2 := \left(N_{\mathrm{part}}^{\mathrm{tar}}/N_0\right)^d \Lambda_{\mathrm{QCD}}^2, \tag{7.3}$$

where Λ_{QCD} signifies the relevant energy scale, and N_0 is set to $N_0 = 1$ for symmetric collisions and increases for asymmetric collisions. The parameter d represents an anomalous dimension and resists a physical interpretation.

Figure 7.7 depicts a double logarithmic plot featuring the required values of Q_0^2 for the description of pseudorapidity distributions across various collisions, along with the fitted curves. Remarkably, these curves exhibit satisfactory agreement within the designated range.

8. Conclusion

This thesis presented a successful model that describes pseudorapidity distributions for produced charged hadrons in asymmetric relativistic heavy-ion collisions. Our model drew inspiration from the three-source Relativistic Diffusion model (RDM), as detailed in section 5.3, but we introduced a novel approach to determine the underlying produced charged hadron distributions. These distributions were successfully linked to the parton model and to the framework of gluon saturation.

Asymmetric collisions introduce a heightened level of complexity compared to symmetric heavy-ion collisions. This increased complexity predominantly stems from the intricate demands associated with accurately handling the corresponding frames of reference. Therefore, we introduced a range of established concepts in chapter 2 to effectively manage the kinematic aspects of asymmetric relativistic heavy-ion collisions.

In our novel approach to determine the three sources, we reviewed the parton model in chapter 3, which introduced the concepts of quarks and gluons. After that, we outlined the framework of gluon saturation and its rapidity evolution equations, leading to the establishment of unintegrated gluon distributions in section 3.3.

By employing two distinct QCD-factorization schemes, namely the k_T- and hybrid-factorization, which were delineated in chapter 4, we integrated all the foundational elements. This approach enabled us to successfully compute pseudorapidity distributions for charged hadrons produced at various relativistic energy scales.

Providing a more detailed account of the three microscopic contributions, our model characterized the colliding particles in terms of their quark and gluon constituents. By employing small-x gluon-gluon interactions within the context of k_T-factorization, we effectively computed the first component of the complete pseudorapidity distributions and established their connection to the mid-rapidity source of the RDM.

The determination of the two fragmentation sources involved utilizing quark-gluon interactions within the hybrid-factorization scheme. However, due to the inherent characteristics of hybrid-factorization, which is primarily employed to describe stopping processes within a collision, the computed distributions required an additional diffusion process to yield meaningful results for describing produced charged hadrons.

This additional diffusion process is governed by a Fokker-Planck equation, as shown in equation (5.8), which accounts for the distinct time scales associated with the stopping process and the production of charged hadrons.

To address the complicated calculations of the underlying non-analytical integrals, the utilization of the parton distribution functions and solving the differential equations, we developed a feature-rich C++ program, which is outlined in section 6.1, to numerically compute the pseudorapidity distributions.

Employing the model we developed, the extended Relativistic Diffusion model, we conducted an investigation into central p-Pb collisions, considering two distinct models for the unintegrated gluon distribution, as detailed in section 6.1. Our analysis indicates that the KLN model (3.43) provides a better description of the experimental data, as illustrated in (6.1). The variations between the models are visualized in 3.4.

Subsequently, we proceeded to explore the centrality-dependent pseudorapidity distributions for asymmetric collisions. This exploration encompassed the analysis of Phobos data at $\sqrt{s_{NN}} = 200\,\text{GeV}$ (7.2), alongside LHC data at $\sqrt{s_{NN}} = 5.02\,\text{TeV}$ (7.4 and 7.5) and $\sqrt{s_{NN}} = 8.16\,\text{TeV}$ (7.6). The computed pseudorapidity distributions accurately match the experimental data across a wide range of pseudorapidity values. In addition, also the sub-distributions of the different sources were presented.

The key findings are detailed in section 7.2, where we conduct a comparison between our computed pseudorapidity distributions and recently released data from ALICE. The experimental results exhibit notable characteristics. They encompass a pseudorapidity range extending up to $\eta = 5$. Furthermore, the categorization of the centrality classes incorporates ultra-peripheral collisions up to 100%. No prior publications have undertaken further investigations of these specific experimental data related to p-Pb collisions.

The examination of centrality-dependent pseudorapidity distributions corresponding to the experimental ALICE data revealed significant indications of the fragmentation sources within our three-source model. In the context of asymmetric collisions, the peaks of produced charged hadrons tend to concentrate in the vicinity of the direction of the heavy-ion target. This scaling behaviour is generally achievable through the inherent nature of the gluon-gluon source.

However, as depicted in figure 7.5, in the case of ultra-peripheral collisions, the experimental ALICE data exhibit a distinct behaviour. In this scenario, the peak of produced charged hadrons shift towards the region aligned with the direction of the projectile-like particle, the proton. This scaling trend cannot be accounted for solely by the gluon-gluon source, but can be accurately described by our three-source model. Further insights into this discussion are expounded upon in section 7.2.

Predictions were made for the larger pseudorapidity regions for the centrality-dependent pseudorapidity distributions in p-Pb collisions at $\sqrt{s_{NN}} = 8.16\,\text{TeV}$, exhibiting a similar trend extending to ultra-peripheral collisions, see figure 7.6.

An enhancement in our approach involves the utilization of the precise transformation between rapidity and pseudorapidity for the gluon-gluon source, as outlined in section 2.2, as opposed to relying on an effective transformation with a parameter that can be freely chosen.

This refinement is particularly important to accurately determine the initial condition of the gluon distributions at $y = 0$ for the rapidity evolution equation. To handle the precise transformation, our model also incorporates the masses of the hadron species.

The implications of this refinement for our model calculations resulted in significantly reduced suppression from the pseudorapidity transformation at mid-rapidity, a phenomenon evident from other calculations documented in the literature.

Consequently, it can be inferred that the dip observed around $\eta = 0$ in charged-hadron production cannot be explained solely by the Jacobian transformation. Instead, the absence of the fragmentation sources plays a significant role in this suppression around $\eta = 0$, as these sources essentially peak at the same pseudorapidity where the distribution of charged-hadron production reaches its two local maxima. This observation can be exploited to accurately ascertain both the initial saturation scale and its dependence on the centrality.

Another distinct aspect of our approach pertains to the characterization of collision geometries. Our model employs pre-existing Glauber-based calculations provided by experimental collaborations, quantified in terms of the number of participants involved in a heavy-ion collision. This approach aims to facilitate a more profound comprehension of the individual contributions stemming from both the collisions' geometric aspects and the intricate interplay of microscopic interactions involving quarks and gluons.

The extended Relativistic Diffusion model holds potential for further enhancement across various aspects.

A more sophisticated rapidity evolution equation, such as the rcBK equation, could be employed, albeit demanding additional numerical implementation efforts. Enhanced initial conditions would also likely result in better alignment with data closer to the beam rapidity.

An improved diffusion coefficient, leading to the exact equilibrium state, or even a two-dimensional realisation of the diffusion process, could also enhance the description of the fragmentation sources.

Bibliography

[1] S. Bethke, α_s 2016, Nucl. Part. Phys. Proc. **282-284**, 149–152 (2017).

[2] V. H. Dinh, J. Hoelck, and G. Wolschin, *Hot-medium effects on* Υ *yields in pPb collisions at* $\sqrt{s_{NN}} = 8.16\ TeV$, Phys. Rev. C **100**, 024906 (2019).

[3] G. Baym, *Ultrarelativistic heavy ion collisions: the first billion seconds*, Nucl. Phys. A **956**, 1–10 (2016).

[4] Y. Liu, C. M. Ko, and T. Song, *Hot medium effects on J/ψ production in p+Pb collisions at* $\sqrt{s_{NN}} = 5.02\ TeV$, Phys. Lett. B **728**, 437–442 (2014).

[5] I. G. Bearden et al. (BRAHMS Collaboration), *Nuclear stopping in* Au+Au *collisions at* $\sqrt{s_{NN}} = 200$GeV, Phys. Rev. Lett. **93**, 102301 (2004).

[6] S. Acharya et al. (ALICE Collaboration), *The ALICE experiment - A journey through QCD*, 2022, arXiv:2211.04384 [nucl-ex].

[7] J. L. Albacete et al., *Predictions for p+Pb collisions at* $\sqrt{s_{NN}} = 5\ TeV$, Int. J. Mod. Phys. E **22**, 1330007 (2013).

[8] J. L. Albacete et al., *Predictions for p+Pb collisions at* $\sqrt{s_{NN}} = 5\ TeV$*: Comparison with data*, Int. J. Mod. Phys. E **25**, 1630005 (2016).

[9] Z.-W. Lin, C. M. Ko, B.-A. Li, B. Zhang, and S. Pal, *Multiphase transport model for relativistic heavy ion collisions*, Phys. Rev. C **72**, 064901 (2005).

[10] A. H. Rezaeian, *CGC predictions for p+A collisions at the LHC and signature of QCD saturation*, Phys. Lett. B **718**, 1058–1069 (2013).

[11] J. L. Albacete et al., *Predictions for cold nuclear matter effects in p+Pb collisions at* $\sqrt{s_{NN}} = 8.16\ TeV$, Nucl. Phys. A **972**, 18–85 (2018).

[12] J. L. Albacete, A. Dumitru, H. Fujii, and Y. Nara, *CGC predictions for p+Pb collisions at the LHC*, Nucl. Phys. A **897**, 1–27 (2013).

[13] G. Wolschin, *Relativistic diffusion model*, Eur. Phys. J. A **5**, 85–90 (1999).

[14] G. Wolschin, M. Biyajima, T. Mizoguchi, and N. Suzuki, *Time evolution of relativistic d+Au and Au+Au collisions*, Ann. Phys. **518**, 369–378 (2006).

[15] D. M. Röhrscheid and G. Wolschin, *Centrality dependence of charged-hadron pseudorapidity distributions in PbPb collisions at energies available at the CERN Large Hadron Collider in the relativistic diffusion model*, Phys. Rev. C **86**, 024902 (2012).

[16] G. Wolschin, *Particle production sources at LHC energies*, J. Phys. G: Nucl. Part. Phys. **40**, 045104 (2013).

[17] P. Schulz and G. Wolschin, *Diffusion-model analysis of pPb and PbPb collisions at LHC energies*, Mod. Phys. Lett. A **33**, 1850098 (2018).

[18] P. Schulz and G. Wolschin, *Analysis of pPb collisions at LHC energies in the relativistic diffusion model*, Eur. Phys. J. A **51**, 18 (2015).

[19] J. Gosset et al., *Central collisions of relativistic heavy ions*, Phys. Rev. C **16**, 629–657 (1977).

[20] C.-Y. Wong, *Introduction to High-Energy Heavy-Ion Collisions* (World Scientific, Singapore, 1994).

[21] R. Sahoo, *Relativistic kinematics*, 2016, arXiv:1604.02651 [nucl-ex].

[22] G. Wolschin, *Produced charged hadrons in central Pb+Pb collisions at LHC energies in the RDM*, Phys. Lett. B **698**, 411 (2011).

[23] L. P. Csernai, *Introduction to relativistic heavy ion collisions* (John Wiley and Sons Ltd, Chichester, United Kingdom, 1994).

[24] M. L. Miller, K. Reygers, S. J. Sanders, and P. Steinberg, *Glauber modeling in high-energy nuclear collisions*, Annu. Rev. Nucl. Part. Sci. **57**, 205–243 (2007).

[25] R. Glauber and G. Matthiae, *High-energy scattering of protons by nuclei*, Nucl. Phys. B **21**, 135–157 (1970).

[26] B. Alver, M. Baker, C. Loizides, and P. Steinberg, *The PHOBOS Glauber Monte Carlo*, 2008, arXiv:0805.4411 [nucl-ex].

[27] L. Gribov, *Semihard processes in QCD*, Phys. Rep. **100**, 1–150 (1983).

[28] A. D. Martin, *Proton structure, Partons, QCD, DGLAP and beyond*, Acta Phys. Polon. B **39**, 2025–2062 (2008).

[29] J. D. Bjorken, J. B. Kogut, and D. E. Soper, *Quantum Electrodynamics at infinite momentum: Scattering from an external field*, Phys. Rev. D **3**, 1382–1399 (1971).

[30] M. E. Peskin and D. V. Schroeder, *An Introduction to Quantum Field Theory* (Perseus Books, Massachusetts, 1995).

[31] J. C. Collins, D. E. Soper, and G. Sterman, *Factorization of hard processes in QCD*, Perturbative QCD, 1–91 (1989).

[32] G. Altarelli and G. Parisi, *Asymptotic freedom in parton language*, Nucl. Physics, Sect. B **126**, 298–318 (1977).

[33] A. D. Martin, W. J. Stirling, R. S. Thorne, and G. Watt, *Parton distributions for the LHC*, Eur. Phys. J. C **63**, 189–285 (2009).

[34] L. Gribov, E. Levin, and M. Ryskin, *Singlet structure function at small x: unitarization of gluon ladders*, Nuclear Physics B **188**, 555–576 (1981).

[35] J. Albacete and C. Marquet, *Gluon saturation and initial conditions for relativistic heavy ion collisions*, Prog. Part. Nucl. Phys. **76**, 1–42 (2014).

[36] E. A. Kuraev, L. N. Lipatov, and V. S. Fadin, *The pomeranchuk singularity in nonabelian gauge theories*, Sov. Phys. JETP **45**, 199–204 (1977).

[37] I. I. Balitsky and L. N. Lipatov, *The pomeranchuk singularity in quantum chromodynamics*, Sov. J. Nucl. Phys. **28**, 822–829 (1978).

[38] F. Gelis, E. Iancu, J. Jalilian-Marian, and R. Venugopalan, *The color glass condensate*, Annu. Rev. Nucl. Part. Sci. **60**, 463–489 (2010).

[39] D. Triantafyllopoulos, *The energy dependence of the saturation momentum from RG improved BFKL evolution*, Nucl. Phys. B **648**, 293–316 (2003).

[40] V. Gonçalves and M. da Silva, *Probing the color glass condensate in pp collisions at forward rapidities and very low transverse momenta*, Nucl. Phys. A **906**, 28–36 (2013).

[41] D. Kharzeev, E. Levin, and M. Nardi, *Color glass condensate at the LHC: hadron multiplicities in pp, pA and AA collisions*, Nucl. Phys. A **747**, 609–629 (2005).

[42] L. McLerran and R. Venugopalan, *Gluon distribution functions for very large nuclei at small transverse momentum*, Phys. Rev. D **49**, 3352–3355 (1994).

[43] L. McLerran and R. Venugopalan, *Computing quark and gluon distribution functions for very large nuclei*, Phys. Rev. D **49**, 2233–2241 (1994).

[44] D. Kharzeev and M. Nardi, *Hadron production in nuclear collisions at RHIC and high-density QCD*, Phys. Lett. B **507**, 121–128 (2001).

[45] I. Balitsky, *Operator expansion for high-energy scattering*, Nucl. Phys. B **463**, 99–157 (1996).

[46] J. Jalilian-Marian, A. Kovner, L. McLerran, and H. Weigert, *Intrinsic glue distribution at very small x*, Phys. Rev. D **55**, 5414–5428 (1997).

[47] J. Jalilian-Marian, A. Kovner, A. Leonidov, and H. Weigert, *The BFKL equation from the Wilson renormalization group*, Nuclear Physics B **504**, 415–431 (1997).

[48] J. Jalilian-Marian, A. Kovner, A. Leonidov, and H. Weigert, *Wilson renormalization group for low x physics: Towards the high density regime*, Phys. Rev. D **59**, 014014 (1998).

[49] J. Jalilian-Marian, A. Kovner, and H. Weigert, *Wilson renormalization group for low x physics: Gluon evolution at finite parton density*, Phys. Rev. D **59**, 014015 (1998).

[50] J. Jalilian-Marian, A. Kovner, A. Leonidov, and H. Weigert, *Unitarization of gluon distribution in the doubly logarithmic regime at high density*, Phys. Rev. D **59**, 034007 (1999).

[51] E. Iancu, A. Leonidov, and L. McLerran, *Nonlinear gluon evolution in the color glass condensate: I*, Nucl. Phys. A **692**, 583–645 (2000).

[52] E. Iancu and L. McLerran, *Saturation and universality in qcd at small x*, Physics Letters B **510**, 145–154 (2001).

[53] E. Ferreiro, E. Iancu, A. Leonidov, and L. McLerran, *Nonlinear gluon evolution in the color glass condensate: II*, Nucl. Phys. A **703**, 489–538 (2002).

[54] E. Iancu, A. Leonidov, and L. McLerran, *The renormalization group equation for the color glass condensate*, Physics Letters B **510**, 133–144 (2001).

[55] H. Weigert, *Unitarity at small Bjorken x*, Nuclear Physics A **703**, 823–860 (2002).

[56] A. Mueller, *A simple derivation of the JIMWLK equation*, Physics Letters B **523**, 243–248 (2001).

[57] J. L. Albacete and A. Dumitru, *A model for gluon production in heavy-ion collisions at the LHC with rcBK unintegrated gluon densities*, (2010), arXiv:`1011.5161 [hep-ph]`.

[58] Y. V. Kovchegov, *Unitarization of the BFKL Pomeron on a nucleus*, Phys. Rev. D **61**, 074018 (2000).

[59] Y. Shi, S.-Y. Wei, and J. Zhou, *Parton shower generator based on the Gribov-Levin-Ryskin equation*, Phys. Rev. D **107**, 016017 (2023).

[60] A. Dumitru, A. Hayashigaki, and J. Jalilian-Marian, *The color glass condensate and hadron production in the forward region*, Nucl. Phys. A **765**, 464–482 (2006).

[61] E. Iancu, A. H. Mueller, and D. N. Triantafyllopoulos, *CGC factorization for forward particle production in proton-nucleus collisions at next-to-leading order*, J. High Energy Phys. **2016**, 41 (2016).

[62] F. Gelis, *Color glass condensate and glasma*, Int. J. Mod. Phys. A **28**, 1330001 (2013).

[63] I. Balitsky, *Quark contribution to the small-x evolution of color dipole*, Phys. Rev. D **75**, 014001 (2007).

[64] Y. V. Kovchegov and H. Weigert, *Triumvirate of running couplings in small-x evolution*, Nucl. Phys. A **784**, 188–226 (2007).

[65] J. L. Albacete and Y. V. Kovchegov, *Solving the high energy evolution equation including running coupling corrections*, Phys. Rev. D **75**, 125021 (2007).

[66] J. L. Albacete, N. Armesto, J. G. Milhano, and C. A. Salgado, *Nonlinear QCD meets data: a global analysis of lepton-proton scattering with running coupling Balitsky-Kovchegov evolution*, Phys. Rev. D **80**, 034031 (2009).

[67] K. Golec-Biernat and M. Wüsthoff, *Saturation effects in deep inelastic scattering at low Q^2 and its implications on diffraction*, Phys. Rev. D **59**, 014017 (1998).

[68] K. Golec-Biernat and M. Wüsthoff, *Saturation in diffractive deep inelastic scattering*, Phys. Rev. D **60**, 114023 (1999).

[69] J. L. Albacete, N. Armesto, J. G. Milhano, C. A. Salgado, and U. A. Wiedemann, *Numerical analysis of the Balitsky-Kovchegov equation with running coupling: dependence of the saturation scale on nuclear size and rapidity*, Phys. Rev. D **71**, 014003 (2005).

[70] D. Boer, A. Utermann, and E. Wessels, *Geometric scaling at BNL RHIC and CERN LHC*, Phys. Rev. D **77**, 054014 (2008).

[71] D. Kharzeev, Y. V. Kovchegov, and K. Tuchin, *Nuclear modification factor in d+Au collisions: onset of suppression in the color glass condensate*, Phys. Lett. B **599**, 23–31 (2004).

[72] D. Kharzeev and E. Levin, *Manifestations of high density QCD in the first RHIC data*, Phys. Lett. B **523**, 79–87 (2001).

[73] A. Dumitru, A. V. Giannini, M. Luzum, and Y. Nara, *Particle multiplicities in the central region of high-energy collisions from k_T-factorization with running coupling corrections*, Phys. Lett. B **784**, 417–422 (2018).

[74] D. Kharzeev, E. Levin, and M. Nardi, *QCD saturation and deuteron-nucleus collisions*, Nucl. Phys. A **730**, 448–459 (2004).

[75] D. Kharzeev, E. Levin, and M. Nardi, *Onset of classical QCD dynamics in relativistic heavy ion collisions*, Phys. Rev. C **71**, 054903 (2005).

[76] F. O. Durães, A. V. Giannini, V. P. Goncalves, and F. S. Navarra, *Testing the running coupling k_T-factorization formula for the inclusive gluon production*, Phys. Rev. D **94**, 054023 (2016).

[77] A. Mueller, *Parton saturation at small x and in large nuclei*, Nucl. Phys. B **558**, 285–303 (1999).

[78] A. Mueller, *Toward equilibration in the early stages after a high energy heavy ion collision*, Nucl. Phys. B **572**, 227–240 (2000).

[79] S. J. Brodsky and G. R. Farrar, *Scaling laws at large transverse momentum*, Phys. Rev. Lett. **31**, 1153–1156 (1973).

[80] V. A. Matveev, R. M. Muradyan, and A. N. Tavkhelidze, *Automodellism in the large-angle elastic scattering and structure of hadrons*, Lett. Nuovo Cimento **7**, 719–723 (1973).

[81] J. C. Collins and D. E. Soper, *The theorems of perturbative QCD*, Annual Review of Nuclear and Particle Science **37**, 383–409 (1987).

[82] A. Kovner, L. McLerran, and H. Weigert, *Gluon production from non-Abelian Weizsäcker-Williams fields in nucleus-nucleus collisions*, Phys. Rev. D **52**, 6231–6237 (1995).

[83] A. Kovner, L. McLerran, and H. Weigert, *Gluon production at high transverse momentum in the McLerran-Venugopalan model of nuclear structure functions*, Phys. Rev. D **52**, 3809–3814 (1995).

[84] B. S. Pudliner, V. R. Pandharipande, J. Carlson, S. C. Pieper, and R. B. Wiringa, *Quantum Monte Carlo calculations of nuclei with $A <\sim 7$*, Phys. Rev. C **56**, 1720–1750 (1997).

[85] Y. V. Kovchegov and D. H. Rischke, *Classical gluon radiation in ultrarelativistic nucleus-nucleus collisions*, Phys. Rev. C **56**, 1084–1094 (1997).

[86] X. Guo, *Gluon minijet production in nuclear collisions at high energies*, Phys. Rev. D **59**, 094017 (1999).

[87] Y. V. Kovchegov and K. Tuchin, *Inclusive gluon production in deep inelastic scattering at high parton density*, Phys. Rev. D **65**, 074026 (2002).

[88] A. Dumitru, A. Hayashigaki, and J. Jalilian-Marian, *Geometric scaling violations in the central rapidity region of d+Au collisions at RHIC*, Nucl. Phys. A **770**, 57–70 (2006).

[89] R. P. Feynman, *Very high-energy collisions of hadrons*, Phys. Rev. Lett. **23**, 1415–1417 (1969).

[90] A. Hayashigaki, *Proton and anti-proton production in the forward region of collisions at RHIC from the color glass condensate*, Nucl. Phys. A **775**, 51–68 (2006).

[91] Y. Mehtar-Tani and G. Wolschin, *Baryon stopping as a new probe of geometric scaling*, Phys. Rev. Lett. **102**, 182301 (2009).

[92] J. L. Albacete and C. Marquet, *Single inclusive hadron production at RHIC and the LHC from the color glass condensate*, Phys. Lett. B **687**, 174–179 (2010).

[93] T. Altinoluk and A. Kovner, *Particle production at high energy and large transverse momentum: "The hybrid formalism" revisited*, Phys. Rev. D **83**, 105004 (2011).

[94] Y. Mehtar-Tani and G. Wolschin, *Baryon stopping and saturation physics in relativistic collisions*, Phys. Rev. C **80**, 054905 (2009).

[95] S. M. Ross, *Introduction to Probability Models* (Academic Press, San Diego, CA, 2014).

[96] H. Risken, *The Fokker-Planck Equation*, Vol. 18, Springer Series in Synergetics (Springer, Berlin, Heidelberg, 1996).

[97] N. G. van Kampen, *Die Fokker-Planck-Gleichung*, Phys. J. **53**, 1012–1013 (1997).

[98] G. Wolschin, *From RHIC to LHC: A relativistic diffusion approach*, Nucl. Phys. A **787**, 68–73 (2007).

[99] A. Lavagno, *Anomalous diffusion in non-equilibrium relativistic heavy-ion rapidity spectra*, Phys. A Stat. Mech. its Appl. **305**, 238–241 (2002).

[100] G. Wolschin, *Anomalous net-baryon-rapidity spectra at RHIC*, Phys. Lett. B **569**, 67–72 (2003).

[101] F. Forndran and G. Wolschin, *Relativistic diffusion model with nonlinear drift*, Eur. Phys. J. A **53**, 37 (2017).

[102] G. E. Uhlenbeck and L. S. Ornstein, *On the theory of the brownian motion*, Phys. Rev. **36**, 823–841 (1930).

[103] G. Wolschin, *Diffusion and local deconfinement in relativistic systems*, Nucl. Phys. A **752**, 484–488 (2005).

[104] J. Adam et al. (ALICE Collaboration), *Centrality dependence of particle production in p-Pb collisions at* $\sqrt{s_{NN}} = 5.02\ TeV$, Phys. Rev. C **91**, 064905 (2015).

[105] S. Acharya et al. (ALICE Collaboration), *System-size dependence of the charged-particle pseudorapidity density at* $\sqrt{s_{NN}} = 5.02\ TeV$ *for pp, p-Pb, and Pb-Pb collisions*, Phys. Lett. B **845**, 137730 (2023).

[106] S. Albino, B. Kniehl, and G. Kramer, *AKK update: Improvements from new theoretical input and experimental data*, Nucl. Phys. B **803**, 42–104 (2008).

[107] R. Piessens, E. de Doncker-Kapenga, C. W. Überhuber, and D. K. Kahaner, *Quadpack*, Vol. 1, Springer Series in Computational Mathematics (Springer, Berlin, Heidelberg, 1983).

[108] B. Gough, *GNU scientific library reference manual* (Network Theory Ltd., 2009).

[109] M. Blatt et al., *The distributed and unified numerics environment, Version 2.4*, Archive of Numerical Software **4**, 13–29 (2016).

[110] P. Bastian, F. Heimann, and S. Marnach, *Generic implementation of finite element methods in the Distributed and Unified Numerics Environment (DUNE)*, Kybernetika **46**, 294–315 (2010).

[111] R. Brun and F. Rademakers, *ROOT - An object oriented data analysis framework*, 1997.

[112] J. Adam et al. (ALICE Collaboration), *Centrality dependence of the pseudorapidity density distribution for charged particles in Pb-Pb collisions at* $\sqrt{s_{NN}} = 5.02\ TeV$, Phys. Lett. B **772**, 567–577 (2017).

[113] B. Abelev et al. (ALICE Collaboration), *Centrality dependence of* π, K, *and p production in Pb-Pb collisions at* $\sqrt{s_{NN}} = 2.76\ TeV$, Phys. Rev. C **88**, 044910 (2013).

[114] S. Acharya et al. (ALICE Collaboration), *Production of charged pions, kaons, and (anti-)protons in Pb-Pb and inelastic pp collisions at* $\sqrt{s_{NN}} = 5.02\ TeV$, Phys. Rev. C **101**, 044907 (2020).

[115] B. B. Back et al. (PHOBOS Collaboration), *Pseudorapidity distribution of charged particles in d+Au collisions at* $\sqrt{s_{NN}} = 200\ GeV$, Phys. Rev. Lett. **93**, 082301 (2003).

[116] A. M. Sirunyan et al. (CMS Collaboration), *Pseudorapidity distributions of charged hadrons in proton-lead collisions* $\sqrt{s_{NN}} = 5.02$ *and* $8.16\ TeV$, J. High Energy Phys. **2018**, 45 (2018).

[117] B. Alver et al. (PHOBOS Collaboration), *Phobos results on charged particle multiplicity and pseudorapidity distributions in Au+Au, Cu+Cu, d+Au, and p+p collisions at ultra-relativistic energies*, Phys. Rev. C **83**, 024913 (2011).

[118] M. Ploskon (ALICE Collaboration), *Conference talk*, Hard Probes (2015).

[119] B. B. Back et al. (PHOBOS Collaboration), *Scaling of charged particle production in d+Au collisions at* $\sqrt{s_{NN}} = 200\ GeV$, Phys. Rev. C **72**, 031901 (2005).

[120] F. Gelis, A. Staśto, and R. Venugopalan, *Limiting fragmentation in hadron-hadron collisions at high energies*, Eur. Phys. J. C **48**, 489–500 (2006).

[121] A. Dumitru, D. E. Kharzeev, E. M. Levin, and Y. Nara, *Gluon saturation in pA collisions at energies available at the CERN Large Hadron Collider: Predictions for hadron multiplicities*, Phys. Rev. C **85**, 044920 (2012).

[122] G. Aad et al. (ATLAS Collaboration), *Measurement of the centrality dependence of the charged-particle pseudorapidity distribution in proton-lead collisions at* $\sqrt{s_{NN}} = 5.02\ TeV$ *with the ATLAS detector*, Eur. Phys. J. C **76**, 199 (2016).

[123] B. Abelev et al. (ALICE Collaboration), *Pseudorapidity density of charged particles in p+Pb collisions at* $\sqrt{s_{NN}} = 5.02\ TeV$, Phys. Rev. Lett. **110**, 032301 (2013).

[124] S. Acharya et al. (ALICE Collaboration), *Charged-particle pseudorapidity density at mid-rapidity in p-Pb collisions at* $\sqrt{s_{NN}} = 8.16\ TeV$, Eur. Phys. J. C **79**, 307 (2019).